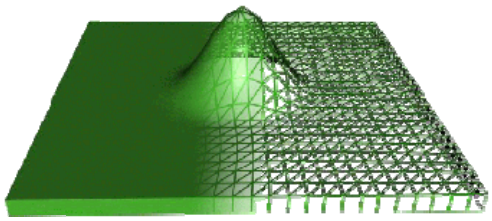

Thèse

par

Anna PANDOLFI

pour l'obtenition du grade de :
Docteur de l'Université Paul Verlaine de METZ

Spécialité: Physique et Sciences pour l'Ingénieur
Option: Mécanique

Théories Cohésives de Rupture pour l'Analyse Numérique de l'Endommagement des Matériaux

Soutenue à Metz le 7 Décembre 2007 à 14h30 devant le jury composé de :

Saïd Ahzi	Professeur à l'Université de Strasbourg, IMFS	Rapporteur
Jean-François Molinari	Professeur à l'Université de Lausanne CH, EPFL	Rapporteur
Jean-François Ganghoffer	Professeur à l'Université de Nancy, INPL	Examinateur
Michael Ortiz	Professeur à Caltech, Pasadena CA, USA	Examinateur
Alain Molinari	Professeur à l'Université de Metz, LPMM	Directeur de thèse

Laboratoire de Physique et Mécanique des Matériaux, U.M.R., C.N.R.S. n°7554, université de Metz - Ile du Saulcy - 57045 METZ Cedex 01 (FRANCE)

Théories Cohésives de Rupture pour l'Analyse Numérique de l'Endommagement des Matériaux

Cohesive Theories of Fracture in Numerical Modelling of Material Failure

A Pina e Dino

Résumé

Des outils pour l'analyse numérique avançée des phénomènes de rupture, impliquant la nucléation, la propagation, la bifurcation en plusieurs branches et la formation de fragments, sont présentés et discutés. Dans le cadre de la discrétisation par élément finis, les fissures sont décrites explicitement comme paires de surfaces interrompant la continuité du corps. Les comportements anélastiques du matériau pendant l'ouverture progressive d'une fissure sont décrits globalement par des lois cohésives. Des théories cohésives de rupture sont obtenues dans le cadre d'une approche thermodynamique. La physique de la rupture est reproduite correctement par l'usage de variables appropriées, c'est à dire par le saut de déplacement à travers la discontinuité et la traction cohésive. Les lois cohésives ont été largement employées en combinaison avec les éléments finis, comme conditions de frontière, ou par l'enrichissement de l'ensemble des fonctions de forme des éléments solides prenant en compte la description du saut de déplacement. L'approche développée ici est différente: on permet aux surfaces cohésives de se développer selon les frontières des éléments solides. Ainsi, une procédure automatique capable de modifier de manière adaptative la géométrie et la topologie d'une maille solide a été développée et combinée avec un code dynamique explicite.
Bien qu'un tel choix puisse réduire la possibilité de décrire exactement le chemin de la fissure, puisque les surfaces de la fissure sont intrinsèquement attachées à la maille initiale, le procédure a été validée par la simulation de nombreuses expériences de rupture dynamique. Des applications à la rupture dynamique de matériaux fragiles classiques (béton, céramique), de matériaux ductiles (acier, aluminium), de polymères et composites (PMMA, graphite-époxyde), et de tissus biologiques (os, artères) ont montré que la méthodologie est fiable et prédictive. En particulier, dans le contexte de problèmes dynamiques, la présence d'une échelle temporelle caractéristique confère aux modèles cohésifs une qualité intrinsèque, c'est a dire la dépendance en vitesse.
Pour conclure ce travail, nous proposons une nouvelle façon de décrire le comportement d'un matériau basée sur les théories cohésives. Le modèle construit explicitement des microstructures particulières basées sur l'introduction de surfaces cohésives equiespacées (défauts) dans une matrice solide. Le modèle décrit l'élasticité, la nucléation des défauts et le comportement cohésif et frictionnel. Les microstructures peuvent se développer périodiquement à différents niveaux, et caractérizer ainsi le matériau sur plusieurs échelles de longueur. Un tel modèle est approprié pour décrire le comportement dynamique des matériaux fragiles sous chargement compressif jusqu'à rupture.

Mots clés: Rupture, Théories cohésives, Eléments finis, Fragmentation, Remaillage, Longueur et temps caractéristiques, Endommagement fragile.

Intitulé et adresse du laboratoire
Laboratoire de Physique et Mécanique des Matériaux (LPMM)
UMR CNRS 7554, Université Paul Verlaine-Metz - Ile du Saulcy, 57045 METZ, France

Abstract

Basic tools for advanced numerical analysis of fracture processes, involving nucleation, propagation, branching and eventually fragment formation, are presented and discussed. In the framework of finite element discretization, cracks are modelled explicitly as a pair of surfaces breaking the continuity of the body. The inelastic behaviors exhibited by the material during the progressive opening of a crack are described globally through cohesive laws. Cohesive theories of fracture are derived here from a sound thermodynamic background. Thus, the physics of fracture is reproduced correctly by the work-conjugate variables, i.e. displacement jump across the discontinuity and the cohesive traction.
Cohesive laws have been widely used in combination with finite elements, as boundary conditions, or by enriching the set of shape functions of solid elements to include the description of the displacement jump. The approach pursued here is different: cohesive surfaces are allowed to develop along boundary surfaces of solid elements. An automatic procedure able to modify adaptively geometry and topology of a solid mesh has been developed and combined with an explicit dynamic code.
Although such choice may reduce the possibility to describe accurately the crack path, since the crack segments are intrinsically dependent on the initial mesh size, the procedure has been validated through the simulation of a number of dynamic fracture experiments. Applications to dynamic fracture of classic brittle materials (concrete, ceramics), of ductile materials (steel, aluminum), of polymers and composites (PMMA, graphite-epoxy), and of biological tissues (bones, arteries) proved that the methodology is reliable and highly predictive. In particular, the presence of a characteristic time scale confers to cohesive models combined with dynamics an intrinsic rate-dependence without the need of modelling viscosity explicitly.
As closing part of this work, we propose an innovative material model based on cohesive theories. We directly construct special micro-structures by distributing equi-spaced cohesive surfaces (faults) in a continuum material. The model accounts for elasticity of the bulk, nucleation of faults and cohesive and frictional behavior. Micro-structures can develop recursively at different levels, thus they embed the material with several length scales. Such material model is suitable to describe the dynamic behavior up to failure of brittle materials, undergoing compressive loading.

Keywords: Fracture, Cohesive Theories, Finite elements, Fragmentation, Adaptive remeshing, Characteristic length and time, Brittle Damage.

Remerciements

Mes remerciements les plus sincères à Alain Molinari et Guruswami Ravichandran pour leur constants encouragements. Je remercie la collaboration de Rena C. Yu, Gonzalo Ruiz et Sergio Conti dans le travail présenté ici. A mon mentor, Michael Ortiz, va ma reconnaissance la plus profonde.

My heartfelt thanks to Alain Molinari and Guruswami Ravichandran for their constant encouragement. I acknowledge the collaboration of Rena C. Yu, Gonzalo Ruiz and Sergio Conti in the research here presented. My deepest gratitude goes to my mentor, Michael Ortiz.

Table des Matières

Chapter 1

Introduction

Le comportement des matériaux subissant des chocs, des impacts, et des conditions de chargements extrêmes, jusqu'à la rupture, a toujours attiré l'attention des chercheurs. Dans les deux dernières décennies la capacité de prévoir la rupture des matériaux a considérablement augmenté avec l'appui des outils informatiques. Il y a deux raisons principales expliquant la réussite de la symbiose entre la mécanique et les approches numériques: d'un côté, la croissance exponentielle de la puissance des ordinateurs permet d'étudier des problèmes de complexité croissante; de l'autre côté, les procédures numériques utilisées pour la solution des problèmes de rupture sont améliorées constamment avec l'appui de théories nouvelles, empruntées parfois à d'autres champs de recherche.

Ces dernières années nous sommes témoins d'un développement étonnant des idées, procédures, algorithmes, et techniques, visant à prévoir numériquement le comportement des solides et des structures subissant des conditions extrêmes de chargement jusqu'à la rupture. Quelques approches sont intéressantes, conceptuellement simples et donc accessibles à une grande communauté. D'autres méthodes sont extrêmement avancées, mais compliquées et disponibles seulement à de petits groupes de chercheurs. Toutes, néanmois, contribuent à la connaissance des phénomènes de rupture et à des avancées dans le domaine des méthodes numériques en mécanique.

Dans ces développements il n'y a plus aucun sujet laissé de côté. La mécanique des structures compte sur les méthodes numériques pour concevoir d'audacieuses constructions à grandes échelles (machineries, bâtiments, avions) et structures sophistiquées à petites échelles (systèmes micro-électro-mécaniques); la science des matériaux exploite les possibilités offertes par les méthodes numériques pour analyser le comportement des matériaux complexes et pour concevoir des matériaux innovants; la mécanique des matériaux adapte des concepts innovateurs et des idées nouvelles à la description

des comportements non-linéaires, tels que la plasticité, la viscosité, les problèmes de localisation de la déformation, et la rupture.

Les travaux présentés ici portent essentiellement sur les simulations de la rupture par éléments finis. Spécifiquement nous adressons la rupture dynamique des matériaux fragiles, en particulier les verres, céramiques, roches et bétons. La source principale de dissipation d'énergie dans les matériaux fragiles est la création de surfaces de rupture. Généralement ces matériaux manquent de mécanismes dissipatifs alternatifs qui peuvent absorber un apport important en énergie pendant un intervalle de temps limité. Soumis aux vitesses de déformation élevées, les matériaux fragiles développent des ruptures complexes et produisent des chemins entrelacés de fragmentation. Les fissures peuvent naître de défauts préexistants, ou être générées au niveau d'hétérogénités présentes dans le matériau et produisant des concentrations de contraintes à l'échelle microscopique. Après nucléation, la rupture se peut produire d'une manière distribuée, par micro-fissuration, ou sous forme de macro-fissures dominantes. Les fissures suivent des chemins souvent tortueux, subissent des embranchement, se connectent aux surfaces libres ou avec d'autres fissures pour former des fragments. La complexité du phénomène est reflétée par la perte de convexité des énergies associées, qui exclue souvent l'utilisation des méthodes bien connues dans les calculs numériques.

Traditionnellement, plusieurs approches ont été suivies afin de modéliser ce comportement complexe. Nous mentionnons certaines d'entre elles: mécanique classique de la rupture, mécanique de l'endommagement, méthodes enrichies, et approches cohésives. Sans ambition à être approfondie, dans les prochaines sections nous décrivons brièvement les idées fondamentales de chaque approche, et citons certaines des contributions les plus significatives, en raison de l'influence qu'elles ont eu.

Dans cet aperçu, nous limiterons notre attention aux approches liées à la discrétisation par éléments finis, et ne mentionnons pas des techniques alternatives de discrétisation, telles que les différences finies, les éléments discrets, les éléments de frontière, ou les méthodes meshless.

1.1 La mécanique de la rupture

La mécanique de la rupture aborde spécifiquement la question de savoir si un corps sous charge demeurera intact ou formera une nouvelle surface libre. Dans le cas d'une fissure dominante, la mécanique de la rupture prévoit avec succès le développement de cette fissure, sa direction, et sa vitessse de croissance.

La mécanique de la rupture a été initié au début du dernier siècle avec trois papiers importants dus à Inglis [83], Griffith [75], et Westergaard [192]. Inglis [83] a trouvé la solution analytique du champ de contraintes autour d'un trou elliptique dans une plaque infinie sousmise à une contrainte lointaine uniforme, et a dérivé l'expression du facteur de concentration de contraintes en bout d'ellipse. Pour les matériaux fragiles, Griffith [75] a formulé un critère de rupture basé sur des concepts d'énergie. Griffith a prolongé le concept du minimum de l'énergie potentielle de la mécanique classique et de la thermodynamique en incluant une contribution d'énergie de surface. L'énergie de surface γ mesure le travail qui doit être effectué pour une avance de fissure correspondant à une unité de surface. Afin d'avoir la propagation de fissure, la réduction d'énergie de volume $\Delta W(\boldsymbol{F})$ dû au déchargement des contraintes entre les deux côtés de la fissure doit excéder la consommation de l'énergie de surface pour prolonger la fissure de la quantité ΔS:

$$-\Delta W(\boldsymbol{F}) \geq \gamma \Delta S \tag{1.1}$$

Quelques ans après, Westergaard [192] a dérivé l'expression du champ de contraintes autour d'une fissure, sous un contrainte lointaine normale ou de cisaillement.

Au milieu des années 50, Irwin [84] a développé l'idée de Griffith, et pour ses contributions il est maintenant considéré comme le fondateur de la mécanique de la rupture. Irwin a prolongé la théorie de Griffith aux matériaux ductiles, en supposant l'existence d'une zone plastique près de l'extrémité de la fissure, et a présenté le concept du facteur d'intensité de contraintes K_I et du taux de restitution d'énergie G. Les contraintes en bout de fissure peuvent toujours être exprimées par des fonctions analytiques de K_I et des coordonnées polaires (r, θ), à condition que la distance r du point soit petite par rapport à la taille a de la fissure. Un critère de rupture dérivé déclare que la rupture instable se produit quand le facteur d'intensité des contraintes atteint une valeur critique K_{Ic}, appelé la ténacité à la rupture. La ténacité à la rupture représente la capacité inhérente d'un matériau de résister à une intensité donnée du champ de contraintes en bout de fissure.

Des solutions analytiques du champs de contrainte élastique pour différentes situations, telles qu'une fissure en forme de V, interfaces matérielles, fissures dans des matériaux anisotropes, et beaucoup d'autres, ont été fournies dans des recherches ultérieures. La dérivation de certaines solutions a été particulièrement difficile, et dans plusieurs occasions elle a attiré l'intérêt des mathématiciens. De nos jours, des solutions classiques peuvent être trouvées dans les manuels de mécanique de la rupture.

Les non-linéarités matérielles ont été adressées par Wells [190], qui a employé le concept d'ouverture de la fissure pour caractériser la résistence d'une fissure dans un solide élastoplastique. Une étape importante a été fournie par Rice en 1968 [157]. Il a introduit une intégrale indépendante du chemin (connue dans la littérature comme intégrale-J ou intégrale de Rice) qui exprime la vitesse de changement de l'énergie potentielle pour un solide non linéaire élastique dû à une extension unitaire de la fissure.

Les théories dérivées de la mécanique de la rupture peuvent adresser des questions importantes telles que les effets de taille. Il a été observé expérimentalement que les spécimens de petite taille montrent un comportement plus résistant que les spécimens de grande taille. Les effets de taille peuvent être pris en compte dans les théories. Bažant [9] a présenté pour la première fois un modèle pour la résistance nominale des matériaux quasi-fragiles. Il a postulé que pour les petites tailles, la résistance est dominée par la plasticité et est ainsi peu sensible à la taille; pour les grandes tailles, la résistance est dominée par la mécanique de la rupture élastique et montre une dépendance vis à vis de la taille. Des propositions alternatives sont encore discutées, et une revue critique peut être trouvée dans un papier récent par Saouma et Fava [170].

Les théories classiques de la mécanique de la rupture sont fondées sur le cas limite d'une fissure dominante préexistante (sans compter les autres hypothèses restrictives) et négligent donc complètement la question de la nucléation de la fissure. Les situations complexes de rupture, impliquant beaucoup de fissures entrelacées, comme dans la fragmentation ou dans le processus d'écrasement, sont également étrangers à la mécanique classique de la rupture. D'autres limites apparaissent dans les conditions de progression de la fissure qui sont typiquement exprimées en terme de paramètres caractérisant l'amplitude des champs autonomes près des extrémités d'une fissure. Afin d'appliquer les critères de la mécanique classique de la rupture, l'existence et l'établissement de tels champs autonomes doivent être évalués [84]. Ces conditions limitent sévèrement l'application de la théorie, en imposant que la zone plastique ou la process-zone soit petite relativement aux dimensions géométriques du solide, tels que la taille de ligament. Une autre difficulté est que la structure des champs autonomes en bout de fissure dépend sensiblement du comportement constitutif du matériau, qui lie inextricablement le critère de rupture à la nature du matériau.

D'autres facteurs excluant l'utilisation de la mécanique classique de la rupture sont les phénomènes dynamiques et chargements cycliques. En chargement dynamique, le critère de rupture doit tenir compte de la micro-inertie. En plus, les chargements non proportionnels ou cycliques, comme ceux rencontrés en fatigue, ne permettent pas

l'application de concepts tels que l'intégrale-J.

1.2 Smeared Approaches de l'Endommagement

La rupture est un phénomène fortement non-linéaire, caractérisé par l'absence de compatibilité, une des hypothèses de base de la mécanique du continu. La compatibilité implique la continuité et la régularité de la déformation, et élimine des situations où la matière peut s'interpénétrer ou se séparer. Le mouvement régulier d'un corps, définissant un gradient non singulier de déformation et des mesures appropriées de déformation, n'est pas réalisé dans les phénomènes de rupture.

Bien que comprise, cette question a été délibérément ignorée dans les "smeared" approches d'endommagement, qui traitent les irrégularités du mouvement comme des déformations particulières réparties sur un certain volume.

Dans la pratique, les smeared approches de l'endommagement essayent d'inclure tous les mécanismes dissipatifs dans les relations constitutives, inévitablement par recours à des simplification fortes qui permettent de caractériser analytiquement le comportement apparant des microstructures complexes. Une difficulté importante inhérente aux descriptions constitutives concerne leur incapacité de caractériser les matériaux fragiles avec une énergie de rupture bien définie, telle qu'une mesure de la dissipation d'énergie par unité de surface de fissure. La voie thermodynamique conventionnelle, qui conduit à la formulation de relations constitutives générales, peut traiter la dissipation seulement comme une quantité extensive, possédant une densité bien définie par unité de volume.

Quand ces formulations sont employées pour décrire la rupture en terme de loi décrivant l'endoucissement de la contrainte en fonction de la déformation, on observe des pathologies telle qu'une diminution erronée de l'énergie efficace de la rupture avec la taille de la discrétisation, comme observé la première fois dans les papiers de Cedolin et Bažant [9, 14, 11] et plus tard dans le papier de Pijaudier-Cabot et Bažant [147]. En particulier, les approches par éléments finis qui utilisent les lois standard (appelées locales) de endoucissement de la contrainte avec la déformation conduirent à une convergence erronée.

Le remède peut être l'introduction (de manière explicite ou implicite) d'une échelle de longueur dans la description phénoménologique du matériau. L'échelle de longueur représente un cadre mathématique qui compense la dimensionnalité incorrecte de l'énergie de rupture dans les formulations constitutives. Une telle approche conduit a la défini-

tion de modèles d'endommagement nonlocaux, qui sont désignés généralement sous le nom de modèles régularisés ou de limiteurs de localisation.

Plusieurs chercheurs ont traité la question de la dépendance par rapport au maillage, et diverses théories ont été proposées par régler ce problème de dépendance [146, 148, 86, 66, 1, 2, 54, 10, 147, 52].

Un expédient simple pour préserver la théorie locale de endommagement consiste en un ajustement selon la maille de la pente de la branche décroissante, pour fournir la dissipation voulue d'énergie attendue. Cette correction peut être fournie, par exemple, en incluant la déformation localisée dans la matrice tangente de rigidité, comme dans le papier de Pietruszczak et de Mroz [146]. Alternativement, Pijaudier-Cabot *et al.* [148] ont proposé de remplacer le taux de restitution d'énergie par sa moyenne spatiale au-dessus du volume représentatif, c'est à dire un volume caractérisé par une taille relié à la longueur caractéristique du matériau.

Un des remèdes proposés plus tôt par Ju [86] est l'inclusion de la viscosité, conçue avec le double but (i) de compenser les difficultés numériques dans le calcul, dues à la décroissance des contraintes avec les déformations et à la perte de l'ellipticité forte, phénomène associé à l'endommagement, et (ii) pour expliquer la sensibilité à la vitesse de chargement observée expérimentalement dans les chargements dynamiques. Dans ce cas-ci, la régularisation est obtenue avec l'introduction d'un mécanisme visqueux de endommagement dans les équations constitutives. Récemment, des théories visqueuses de endommagement ont été employées pour modéliser des phénomène géologiques dans le papier par Lyakhovsky *et al.* [103]. La couche séismogénique de la croûte terretre est traitée comme un milieu élastique où la distribution de l'endommagement, qui modifie la rigidité élastique, évolue en fonction de l'histoire de la déformation. Un trait intéressant est que la loi d'évolution de endommagement dans [103] est liée au frottement et explique la dégradation et la re(guérison).

Un outil efficace pour le contrôle des problèmes de dépendance de maille dans les théories de endommagement est l'utilisation du gradient de déformation plastique. Les différentes théories phénoménologiques utilisent le gradient de déformation pour expliquer l'augmentation de la résistance effective d'écoulement des métaux, quand les déformations plastiques ont lieu à l'échelle microscopique. Les théories avec gradient de déformation visent à prolonger la validité de la plasticité conventionnelle en l'étendant de façon à prendre en compte les effets d'échelle de longeur [66]. Ainsi, ces théories doivent pouvoir redonner la théorie locale originale de plasticité quand les échelles de longueur des gradients de déformation imposés sont grandes comparées aux échelles

de longueur du matériaux. Par exemple, la théorie proposée originellement par Aifantis [1, 2] consiste à assigner une largeur aux bandes de cisaillement des métaux, cette largeur jouant le rôle d'une échelle matérielle de longueur. Une théorie analogue est rapportée dans [54]. Dans leur approche, de Borst et Mühlhaus ont supposé que la limite d'écoulement dépend de la déformation plastique cumulée et du Laplacien correspondant. Par conséquence, la condition de cohérence se traduit par une équation différentielle au lieu d'une équation algébrique comme en plasticité conventionnelle. Le grand avantage des approches avec gradient de déformation est qu'elles sont relativement faciles à mettre en oeuvre dans un code par éléments finis, bien qu'on ait observé qu'elles ne peuvent pas résoudre une gamme des problèmes impliquant plusieurs échelles de longueur.

Les modèles nonlocaux de endommagement sont assez semblables aux théories de plasticité avec gradient. Les modèles nonlocaux d'endommagement sont caractérisés par l'hypothèse que la contrainte en un point dépend de la déformation dans une région de taille finie autour du point, voir Bažant et Pijaudier-Cabot [10, 147]. Comme observé par Kunin [93, 94], ceci implique l'introduction d'une loi constitutive (nonlocale) intégrale; i.e., les interactions à longue distance entre particules doivent être prises en compte. En particulier, les théories avec gradient peuvent être considérées comme des approximations, au sense d'une série de Taylor, de la théorie nonlocale. Un examen concis des diverses approches de l'endommagement appliqués à la fissuration, avec des études comparatives, a été présenté par de Borst [53].

L'approche classique de la mécanique du continu peut être insuffisante pour modéliser de façon adéquate les matériaux avec une microstructure. La prise en compte de la microstructure du matériau conduit à différents types de modéles continus standards ou non standards (ou leur combinaison). Des milieux continus non standards sont caractérisés par l'inclusion de degrés de liberté additionnels, en plus de degrés de liberté conventionels en translation. Les degrés de liberté additionnels peuvent refléter, par exemple, des rotations relatives entre les particules adjacentes, ou les mouvements relatifs causant la densification ou la raréfaction des particules matérielles dans un micro-volume, conditions qui brisent l'hypothèse des champs homogènes de contrainte et de déformation dans le volume élémentaire. Des exemples bien connus sont les milieux continus de Cosserat [45], avec des degrés de liberté de rotation, ou les milieux continus de Mindlin [112], où dans un élément de volume l'on considère simultanément macro- et micro- déplacements. L'adoption des continus micro-polaires, avec une échelle intrinsèque de longueur, est discutée dans le travail de de Borst [52], où, dans une for-

mulation de plasticité généralisée, de type $J2$, le deuxième invariant déviatorique des contraintes inclut des couples de contraintes et où le loi d'écrouissage prend en compte des micro-courbures.

1.3 Approaches Enrichies

Dans la méthode des éléments finis, la modélisation de l'évolution des discontinuités est souvent fastidieuse, en raison de la nécessité d'adapter le maillage pour suivre la géométrie de la discontinuité. Plusieurs techniques ont été développées avec l'objectif précis de modéliser la localisation des déformations, la fissuration, et la progression de la fissure en évitant de redéfinir la topologie et d'employer des méthodes sophistiquées de remaillage. Modéliser des régions où les déformations sont fortement localisées peut être fait en incorporant les déformations ou les discontinuités de déplacement dans des interpolations standards des éléments finis, en faisant appel à des techniques d'enrichissement. Les procédures d'enrichissement peuvent différer en terme de type de discontinuité (faible ou forte) considérée, pour le principe variationnel adopté, ou pour le type de loi constitutive prise en compte.

Le papier fondateur de Ortiz, Leroy et Needleman [132] a ouvert le chemin à de nombreuses études sur des éléments finis avec des discontinuités incorporées. Ortiz *et al.* [132] proposent d'enrichir les champs de déformation de sorte qu'une discontinuité faible puisse être prise en compte. Le mode supplémentaire de déformation a été déterminé par une analyse de bifurcation, basée sur le tenseur acoustique. Belytschko et collaborateurs [19] ont poursuivi l'idée de discontinuité faible en proposant d'inclure une zone de localisation dans l'élément fini. Ils ont développé ainsi un élément plus flexible, qui peut être étendu aux grandes déformations et à la viscoplasticité.

Simo, Oliver et Armero [177, 176, 128] ont étudié la relation entre les lois constitutives et les lois d'interface, et ont prouvé qu'une discontinuité forte peut être approximée par une loi constitutive du continu avec une fonction régulière approchant la distribution de Dirac. Des prolongements ont suivi à propos de problèmes non-linéaires par Armero et Garikipati [6] et Oliver *et al.* [125], de problèmes d'endommagement isotrope par Oliver et Pulido [127], de transition progressive d'une faible discontinuité à un forte discontinuité par Oliver *et al.* [124], ceci a démontré la validité et la polyvalence de l'approche.

Dans les années suivantes, des formes alternatives de discontinuités régularisées de déplacement ont été proposées. Une classification intéressante, a été proposée en

se basant sur la cinématique enrichie et sur les conditions d'équilibre, voir Jirásek [85]. D'après cette classification, il est possible d'identifier une classe d'éléments finis contenant des discontinuités fortes incluses (c'est à dire des éléments symétriques statiquement consistants) qui sont affectés d'un blocage en contrainte. Ce problème a été abordé récemment par Oliver *et al.* [126].

Une nouvelle approche tout à fait remarquable pour l'analyse de la propagation de fissure avec les éléments finis a été présentée dans le papier fondateur de Möes, Dolbow et Belytschko [114], où une fissure se développe en redéfinissant la position de la pointe de fissure et en ajoutant des parties nouvelles de surfaces libres. Möes *et al.* ont développé une technique d'enrichissement basée sur le concept de partition de l'unité proposée par Melenk et Babuska [110], qui permet d'incorporer des fonctions locales d'enrichissement dans une approche par éléments finis. En même temps que l'insertion de nouveaux degrés de liberté, un champ discontinu, qui modélize la fissure indépendamment du maillage, est ajouté localement à l'ensemble des fonctions de forme [114]. Pour l'application particulière à l'analyse de la rupture, les fonctions d'enrichissement consistent en des champs asymptotiques près des extrémités de la fissure et une fonction discontinue qui représente le saut de déplacement à travers la ligne de fissure. Dans le détail, le champ de déplacement est global, mais le support des fonctions d'enrichissement est local, parce que l'enrichissement des fonctions est multiplié par des fonctions de forme nodales. Ainsi, la fissure est vue comme une entité géométrique complètement séparée, qui interagit avec le maillage seulement dans le choix des noeuds enrichis. L'exactitude de l'enrichissement de la partition de l'unité est presque indépendante de la taille de l'élément dans une large gamme, et l'approche mène à un système d'équations qui maintient les propriétés du système du maillage original. Un inconvénient de la méthode réside dans la nécessité d'un nombre variable de degrés de liberté du maillage. S'inspirant de [114], beaucoup de contributions ont développé et répandu la classe des méthodes d'élément finis étendus (X-FEM). La littérature courante sur les X-FEM est large, et se développe constamment avec des améliorations et des applications théoriques, mais l'idée originale est toujours préservée. Les évolutions récentes de la méthode des éléments finis étendus peuvent s'adapter au modèle de zone cohésive, voir, par exemple, Möes et Belytschko [113], Wells *et al.* [191], Gasser et Holzapfel [74], et les références incluses dans ces papiers.

1.4 Approaches Cohésives

À partir des travaux fondateur de Dugdale [62] et Barenblatt [8], les modèles cohésifs ont été employés pour décrire la séparation progressive d'un matériau menant à la formation de nouvelles surfaces libres. La théorie suppose que quand une fissure se forme, les forces de cohésion se développent sur les nouvelles surfaces et résistent à l'ouverture progressive. Le lien entre la séparation extérieure (ou le saut de déplacements) et les forces cohésives s'appelle la loi cohésive.

Les théories cohésives de rupture adressent les mêmes questions que celles traitées par la mécanique classique de rupture, mais elles surmontent efficacement la plupart des difficultés évoquées précédemmant. Les modèles cohésifs fournissent une théorie générale de la rupture, et permettent d'incorporer des paramètres fondamentaux de la rupture, tels que l'énergie de rupture et une contrainte d'écaillage. En prenant en compte spécifiquement le processus de séparation, les théories cohésives font une distinction entre la rupture, décrite par des lois cohésives, et le comportement du matériau en volume, décrit par un ensemble indépendant de relations constitutives. Comme conséquence remarquable, l'utilisation des modèles cohésifs n'est limitée par aucune considération de comportement matériel, grandes déformations, de non-proportionnalité du chargement, d'effets dynamiques, ou de géométrie du spécimen.

La première application numérique d'un modèle de zone cohésive a été présentée par Hillerborg *et al.* [79], qui a supposé un modèle non-linéaire où la contrainte est une fonction du saut du déplacement. Quelques annnées plus tard, les recherches de Needleman [119], Ortiz [130], et Willam [193] ont montré les avantages particuliers des lois cohésives de rupture combinées avec les éléments finis et ont ouvert la voie vers une utilisation intensive. Needleman, Tveergard et Ortiz étaient particulièrement actifs dans cette première phase [120, 121, 197, 198, 185, 137, 199, 131, 30, 187, 186, 200], mais de nombreuses applications et développements ont également proliféré parmi différents groupes de recherche. Le terme "fissure cohésive", fait référence a l'application numérique des théories cohésives aux problèmes de fissuration; ce terme est apparu dans le groupe de Carpinteri [22] et s'est répandu avec succès dans la littérature.

La méthodologie initiale –généralement limitée aux cas bidimensionnels– proposée par Needleman et collaborateurs [121, 197, 198, 199] introduit les éléments cohésifs sur toutes les frontières internes d'une maille standard des éléments finis. Cette procédure ajoute une modification artificielle de la compliance du corps discrétisé, puisque la transmission des forces cohésives et la diffusion des contraintes à travers le milieu

imposent une petite séparation entre les éléments. Comme observé par Rice et Beltz [158, 159], quand on utilise des éléments cohésives pre-établis, on doit faire attention à ne pas compter deux fois les effets sur l'élasticité du matériau, une première fois dans la loi cohésive et une deuxième fois dans le comportement du solide. Dans ce sens, les lois cohésives utilisées en combination avec les éléments pre-établis doivent produire une pente infinie pour un déplacement d'ouverture nul. Ceci implique l'adoption de lois rigides à l'origine, ou la modification de la pente initiale par un procédure artificielle, comme expliqué par exemple par Nguyen et Ortiz [122].

On élimine facilement l'excès de deformabilité, sans soucis pour ce qui concerne le choix de la loi cohésive, si les éléments finis solides sont maintenus cohérents jusqu'à ce qu'un critère de rupture approprié soit satisfait sur la surface des éléments. Cette idée venant du groupe d'Ortiz, et a été développée à deux-dimension par Camacho et Ortiz [30] et plus tard à trois-dimensions par Pandolfi et Ortiz [141, 139]. Ortiz et collaborateurs se sont concentrés sur le développement des techniques de remaillage capables d'ajouter les surfaces cohésives d'une manière adaptative. Par les nombreuses idées et questions qu'il a traité, le papier de Camacho et Ortiz [30] est devenu rapidement une référence pour de future extensions, en particulier pour les développements décrits dans ce travail. Camacho et Ortiz ont étudié la faisibilité des théories cohésives de rupture pour la simulation directe des processus de fragmentation de matériaux fragiles soumis à impact. Bien que limité à l'analyse bidimensionnelle, leur approche permet de suivre différentes fissures, leur naissance, leur propagation, les branchements et les jonctions qui conduisent à la formation des fragments. Ceci a montré que, dans les théories cohésives, le difficulté de développer des relations constitutives pour l'écrasement et la fragmentation est évitée. Un des premiers exemples d'analyse tridimensionnelle employant des théories cohésives a été présenté par de Andrés *et a.* [51], quoique le comportement cohésif ait été limité à la cinématique linéarisée.

Certains aspects des méthodes cohésives sont cruciaux pur le succès de l'approche. Bien qu'ils soient développés en détail dans les prochains chapitres, il est instructif de les introduire à l'aide de quelques applications exemplaires.

1.4.1 Longeur Caractéristique

En tant que marque distinctive, les méthodes numériques basées sur les modèles cohésifs ne souffrent pas des pathologies intrinsèques liées à la discrétisation. Cette propriété dérive du fait que les théories cohésives présentent une échelle bien définie de longueur dans la description matérielle et, par conséquent, sont sensibles à la taille

du spécimen [62, 8, 157, 79]. La longueur cohésive caractéristique l_c du matériau est indiquée par

$$l_c = c_1 \frac{EG_c}{\sigma_c^2} \tag{1.2}$$

où c_1 est une constante qui dépend de l'état de contrainte (contrainte plane ou déformation plane), E est le module élastique du matériau, G_c le taux de restitution critique d'énergie et σ_c la résistance à la traction statique, voir, par exemple, Morrissey et Rice [117]. La longueur caractéristique est physiquement liée à l'extension de la process-zone, située en pointe de fissure, où le matériau éprouve toute une variété de phénomènes anélastiques menant à la formation de nouvelles surfaces.

La réalisation de l'indépendance du maillage est subordonnée au respect d'une certaine condition sur le maillage: la zone cohésive doit être résolue de façon adéquate par la discrétisation, voit l'étude par Camacho et Ortiz [30]. Une telle condition est facilement satisfaite pour des matériaux comme le béton, où l'échelle microstructurale de longueur est commensurable avec la taille globale. Dans les bétons, les processus de rupture se produisent souvent sur une échelle comparable aux dimensions géométriques de la structure et la longueur cohésive caractéristique est comparativement grande (de l'ordre du centimètre), voir Ruiz *et al.* [168]. Malheureusement, dans les matériaux ayant une petite longueur microstructurale, ceci peut mener à une densification excessive du maillage en pointe de fissures, voir par exemple Falk *et al.* [64]. Clairement, il est essentiel que le maillage fournisse de riches possibilités pour les cheminements de fissures. Il est évident que le problème de la finesse du maillage devrait être traité de préférence dans le cadre d'un remaillage adaptatif.

Bien que les soucis principaux concernant la dépendance du maillage soient relatifs au chemin des fissures, d'autres questions de convergence peuvent émerger dans des analyses numériques avec les éléments cohésifs, particulièrement en présence de nucléation, d'embranchement et de fragmentation. À titre d'exemple, les simulations numériques sur une plaque en béton, chargée en mode mixte, effectuées par Ruiz *et al.* [169], fournissent une illustration de la compréhension encore inachevée des questions de convergence numérique. Les comparaisons entre les analyses obtenues avec deux tailles de maille différentes (l'une grossière, l'autre plus fine) montrent une forte influence de la taille du maillage sur les courbes d'histoire de chargement. On observe une anomalie dans la consommation d'énergie cohésive, qui est sensiblement plus grande pour le maillage plus fin. On observe la même dépendence dans les courbes de niveaux de la variable d'endommagement, qui reflète une zone micro-fissurée de dimension plus

grande pour le maillage fin. Les surfaces fissurées sont quant à elles, bien nettes pour la maillage plus grossier et comparativement plus rugueuese et instables pour le maillage plus fin. Évidemment, la plus grande intensité de microfissuration obtenue pour le maillage plus fin explique le niveau de dissipation d'énergie plus élevé. La question de la quantité correcte d'énergie dissipée dans la simulation numérique des processus de fissuration est toujours une question ouverte. S'il est clair que les solutions par élément finis montrent une convergence forte une fois la longueur cohésive résolue –comme montré par Camacho et Ortiz [30]–, la situation est plus incertaine pour des processus plus complexes de rupture. Pour les matériaux fragiles, l'augmentation de la microfissuration pour un maillage plus fin est-elle un effet artificiel purement lié à l'algorithme numérique ou bien est-ce le reflet de la physique réelle du processus de nucléation de fissures. Ceci est encore l'object de débats. Autre question: comment et dans quel sens la solution par éléments finis converge-t-elle dans la limite d'un maillage devenant infinitement fin. Le simulations numériques de Ruiz *et al.* [169] semblent indiquer qu'à l'échelle locale les détails du modèle de microfissuration sont en général non-uniques, alors que certaines quantités plus globales, telles que la dissipation d'énergie, sont tout à fait reproductibles et semblent converger correctement avec le raffinement du maillage. Les questions de convergence d'énergie dans les solutions par éléments finis ont été récemment adressées par Molinari *et al.* [115]. Dans le cadre de l'élasticité linéaire, un grand nombre de simulations numériques unidimensionelles de fragmentation sous chargement rapide démontre la convergence de la méthode des éléments cohésifs au sens énergique. Apparemment, l'introduction d'un léger aspect aléatoire dans l'organisation du maillage conduit à une convergence plus rapide de l'approche [115].

1.4.2 Temps Caractéristique

Expérimentalement on observe que la micro-inertie joue souvent un rôle significatif dans le comportement macroscopique effectif des solides aux vitesses élevées de déformation, voir, par exemple, Ravi-Chandar et Knauss [153], et Liu *et al.* [97]. La plupart des simulations de rupture dynamique en béton publiées dans la littérature modèlent la résistance à la traction comme une fonction croissante de la vitesse de déformation, en supposant dans certains cas que l'énergie de rupture est constante et indépendante de la vitesse, voir, par exemple, la recherche par le groupe de Kobayashi [202, 201, 203, 61, 204, 76], par le groupe de Tedesco [181, 81, 180, 167], et par Weerheijm et collaborateurs [155, 188]. Les lois prenant en compte la vitesse de déformation sont nécessairement empiriques et servent à la modélisation du comportement effectif

ou macroscopique du béton sous chargement dynamique.

Par contraste, on observe de façon naturelle la dépendance intrinsèque en vitesse dans les simulations numériques faisant appel aux modèles cohésifs. Comme observé par Camacho et Ortiz [30], les effets de vitesse dans les simulations sont dus à l'interaction entre les échelles caractéristiques (de longueur et de temps) des modèles cohésifs et de l'inertie. En plus de la longueur caractéristique mentionnée ci-dessus, en conditions dynamiques il est possible de définir un temps caractéristique t_c comme:

$$t_c = c_2 \, \frac{\varrho c_L \delta_c}{\sigma_c} \tag{1.3}$$

où la constante c_2 dépend de la loi cohésive choisie, $c_L = \sqrt{E/\varrho}$ est la vitesse des ondes longitudinales, E est le module de Young et ϱ la densité du matériau, et δ_c, σ_c la traction caractéristique et déplacement caractéristique d'ouverture, c'est à dire, une longueur identifiable dans toutes les lois cohésives. Le temps caractéristique t_c peut être interprétée comme le temps requis par la vitesse des ondes longitudinales pour traverser la process-zone en bout de la fissure:

$$t_c = c_3 \, \frac{l_c}{c_L} \tag{1.4}$$

où c_3 est une constante liée à la loi cohésive.

La dépendence intrinsèque en vitesse des modèles cohésifs a été observé dans les simulations de rupture des métaux par Pandolfi *et al.* [140]; dans les matériaux fragiles par Ruiz *et al.* [168, 169]; et dans les milieux composites par Yu *et al.* [205].

Une dépendance en vitesse de déformation a été observée par Pandolfi *et al.* [140] dans la simulation de la fragmentation des anneaux en aluminium en expansion. La fragmentation a été combinée avec le raffinement du maillage (technique appelée *h*-adaptivity). Les simulations numériques se sont révélées tout à fait prédictives d'un certain nombre de faits expérimentaux, incluant: le nombre de strictions dominantes ou arrêtées; la morphologie de la fragmentation; l'effet de la vitesse d'expansion sur le nombre de fragments et la déformation à rupture; et la distribution des tailles de fragments pour une vitesse d'expansion donnée.

La ruine dynamique du béton a été étudié par Ruiz *et al.* [168], en reproduisant sur une barre de Hopkinson des essais brésiliens sur des cylindres en béton. La sensibilité du béton à la vitesse de déformation est représentée par une augmentation presque linéaire de la résistance dynamique avec la vitesse de déformation. Ce point a été bien reproduit

par les simulations. Le modèle numérique prévoit d'autres aspects importants tels que les fissures primaires, avec une forme de lentille, parallèles à la direction de charge et les fissures secondaires diffuses près des appuis. Postérieurement, les mêmes auteurs ont présenté des simulations d'endommagement combiné traction-cisaillement et des phénomènes de rupture en modes I et II dans des spécimens soumis à un chargement dynamique [169]. Les calculs ont reproduit la morphologie de la rupture, les champs de déplacement, ainsi que les trajectoires et les vitesses de fissures, en fonction de la géométrie d'une pré-fissure et des conditions de chargement. Le modèle numérique explique correctement la compétition entre la croissance de la fissure et les mécanismes de nucléation.

Des expériences dynamiques en mode II sur plaques en composite graphite-époxyde ont été modelizées par Yu *et al.* [205], en supposant un modèle cohésif anisotrope de rupture. Les simulations ont reproduit les observations expérimentales par Coker et Rosakis [38] et ont prouvé que, pour des vitesses élevées, la pointe d'une fissure se propageant le long la direction des fibres peut atteindre des vitesses intersoniques, c'est à dire entre la vitesse des ondes de cisaillement et la vitesse des ondes longitudinales parallèlement aux fibres. La structure à double-choc des champs proches en pointe de fissure obtenus avec les simulations est en trés bon accord avec les observations expérimentelles obtenues avec une caméra à grande vitesse.

Comme observé dans des expériences dynamiques de rupture entreprises par Sharon et Fineberg, voir [172], les comportements dépendants de la vitesse déterminent la forme de la propagation des fissures chargées en mode I. A faibles vitesses de chargement, les fissures se développent suivant une ligne droite dans la direction de la fissure originale. Quand la vitesse de chargement augmente, le travail des forces exterieures ne peut pas être absorbé par l'augmentation de la vitesse de fissure. Les expériences ont démontré que la vitesse de la fissure en mode I est limitée supérieurement, et n'excède jamais 40% de la vitesse des ondes de Rayleigh du matériau. En réponse à un apport d'énergie élevé, le matériau réagit en créant plusieurs branches latérales de petites longeurs, qui permettent d'absorber l'excès de énergie. Ce comportement a été reproduit dans des simulations numériques en utilisant une approche cohésive par Falk *et al.* [64] et Yu *et al.* [206].

Une démonstration supplémentaire de la dépendance intrinsèque en vitesse des modèles cohésifs pour des matériaux fragiles est le sujet du travail présenté au chapitre 4, où des simulations du comportement dynamique d'une céramique de haute résistance sont présenteés et discutées.

1.5 Modèles Cohésifs Dépendant de la Vitesse

Comme observé dans la section précédente, l'adoption des modèles cohésifs dans la dynamique conduit à des résultats numériques dépendant en vitesse de chargement, bien que la description du comportement matériel n'inclue pas de dépendance en vitesse. Les matériaux visqueux subissant des processus dynamiques lents montrent cependant des effets réels de dépendance de la vitesse, bien que les effets inertiels ne jouent aucun rôle. Nous nous référons en particulier aux comportements dépendant de la vitesse des composites avec une matrice en polymère, comme observé dans des processus lents de rupture et de décollement, ce sont des résultats liés à la viscosité matérielle.

Dans la simulation numérique du décollement des composites au moyen de lois cohésives, les paramètres de dépendance en vitesse peuvent entrer dans la description du solide et dans le comportement de l'interface. Cependant on ne comprend pas encore complètement l'influence de chaque contribution sur la réponse globale du composite. Généralement, les modèles s'appliquant à décrire l'évolution du délaminage incluent la dépendance en vitesse dans la loi d'interface, voir, par exemple, les travaux de Corigliano et Ricci [44], et Corigliano et Allix [41]. La même stratégie a été suivie dans le papier de Corigliano *et al.* [42, 43]. Les aspects dépendant de la vitesse des processus dynamiques de décollement ont été traités explicitement en adoptant des lois cohésives dépendant de la vitesse pour modéliser la séparation entre les couches du composite. Les mécanismes d'un décollement rapide sont caractérisés par deux échelles différentes de longueur (taille du spécimen et taille de la zone cohésive) et trois échelles de temps différentes (temps caractéristique, vitesse de chargement et temps lié à la réponse visqueuse du matériau). Le problème s'inscrit dans la typologie multi-échelles et fait appel à des approches numériques avançées, voir Mariani *et al.* [105].

1.6 Fracture Dynamique sous Compression

Tandis que la rupture est très localisée pour les corps fragiles subissant un état de traction, un chargements compressif global conduit en général à des fissures diffuses. La mise en compression peut également être caractérisée par la formation de bandes localisées, mais dans beaucoup de cas on observe un endommagement diffus. Les situations aux quelles nous nous référons sont liées à plusieurs cas d'intérêt, incluant: les céramiques structurales confinées, les composites à matrice fragile; les béton sous compression; et les matériaux géologiques. En particulier, pour les aspects géologiques, la comportement fragile des roches est associé aux processus de rupture et de frottement.

La fracture est le phénomène dominant dans les roches sans fissuration initelle, alors que le frottement est dominant dans les cas où des surfaces de glissement pré-existent. Dans les matériaux géologiques on observe qu'aux premières étapes du chargement, le matériau se dégrade en raison de concentrations croissantes de microfissures. Ensuite, les microfissures distribuées dans la process-zone peuvent conduire à une macro-fissure, et finalement le processus de rupture s'accélère et produit la rupture dynamique. Les effets macroscopiques des fissures distribuées et d'autres types d'endommagement exigent un traitement par des modèles constitutifs qui incluent des relations déformation-contrainte non linéaires ainsi que la dégradation et la guérison des matériaux. Ces effets sont bien décrits par Lyakhovsky *et al.* [102], qui présentent un modèle intéressant d'endommagement développé pour l'étude des matériaux géologiques. Le modèle de Lyakhovsky peut décrire la transition de la propagation d'une fissure depuis le régime quasi-statique jusqu'au régime dynamique et donne des échelles appropriées de temps et de longueur pour le début des processus dynamiques catastrophiques.

Le chapitre 5 présente un modèle d'endommagement diffus, qui adopte le comportement cohésif et est approprié pour décrire l'endommagement diffus sous des états compressifs. La théorie fournit le comportement effectif du matériau depuis ses propriétés élastiques jusq'aux changements microstucturaux, qui se développent à différentes échelles de longueur.

1.7 Une Vue Prospective de la Fracture

La recherche ici présentée ne se limite pas à la rupture quasi-statique, sujet en développement constant, encore plus exploré que la rupture dynamique. Nos intérêts principaux sont des développements numériques faisant appel aux théories cohésives pour la description de la rupture. Nous sommes convaincus que les modèles cohésifs peuvent jouer un rôle déterminant. Nous suivons des développements récents dans les approches variationnelles appliquées à l'analyse de la rupture, et notre effort est consacré à la combinaison des théories basées sur l'énergie avec des procédures de rémaillage.

Comme observé dans les sections précédentes, la complexité de la rupture sous conditions dynamiques suggère de raffiner le maillage des éléments finis pour mieux suivre le cheminement des fissures dans les matériaux fragiles. Ce n'est pas le cas pour l'analyse de la propagation de fissure sous conditions quasi-statiques. Le cheminement quasi-statique de fissures impose inévitablement de faire appel à des outils plus

sophistiqués.

Comme beaucoup de phénomènes non-linéaires se produisant quand des solides sont déformés au delà de leur limite élastique (par exemple, bandes de cisaillement dans les matériaux granulaires, surfaces de glissement dans les cristaux ductiles, défauts dans la croûte terrestre), la rupture se localise dans des zones étroites. Contrairement aux déformations régulières, l'énergie associée aux déformations localisées est non convexe. La nature différente de l'énergie induit une compétition entre les déformations régulières et localisées, conduisant en général à l'instabilité du matériau.

Les mathématiciens suggèrent une approche particulière pour l'analyse des déformations localisées: ils supposent que le phénomène se produit sur une "entité géometrique" de dimension inférieure. Dans le cas de la rupture, cette entité (où se situe la discontinuité) est la surface inconnue de rupture. D'après la terminologie du calcul des variations présentée par De Giorgi, les problèmes de discontinuité libre sont des problèmes où l'inconnue est un couple (u, K), où K varie dans une classe d'hypersurfaces fermées (suffisamment régulières) contenues dans un ouvert fixe $\Omega \subset \mathbb{R}_n$, et $u : \Omega \backslash K \to \mathbb{R}_n$ (c'est-à-dire, u est défini partout excepté sur K) appartenant à une classe de fonctions suffisamment régulières.

Les problèmes de discontinuités libres sont habituellement de la forme:

$$\min \{E_v(u, K) + E_s(u, K) + \text{lower order terms}\} \tag{1.5}$$

où E_v, E_s sont interprétés comme des énergies de volume et de surface, respectivement. Dans le cas d'un corps élastique dans la configuration de référence, K représente la surface de la fissure, et u représente la déformation élastique dans la partie intacte du corps. Une expression simple de l'énergie globale peut être dérivée du critère de Griffith de la propagation d'une fissure [75]. En tenant compte de l'inégalité dans l'équation (1.1), l'expression de l'énergie pour un corps isotrope en rupture est simplement proportionnelle à la superficie de K:

$$E_s(u, K) = \gamma \mathcal{H}^{n-1}(K) \tag{1.6}$$

où $\mathcal{H}^{n-1}$ est la mesure de Hausdorff, qui sous l'hypothèse de régularité correspond à l'aire de rupture. Plus généralement, quand il est nécessaire de distinguer l'ouverture et le glissement le long de la fissure, E_s est une intégrale sur K dépendant de la normale

ν sur la surface de la fissure:

$$E_s(u, K) = \int_K \Phi(\nu)\, d\mathcal{H}^{n-1}(K). \tag{1.7}$$

L'énergie de volume prend la forme

$$E_v(u, K) = \int_{\Omega \backslash K} W(u)\, dx. \tag{1.8}$$

La formulation des formes fonctionnelles appropriées de l'énergie d'un solide pour tenir compte des contribution en volume et en surface, a été le sujet d'une recherche active, voir par exemple les travaux par Braides and Chiadò Piat [27], Fonseca et Francfort [67], Braides *et al.* [29], et Ambrosio et Braides [5].

En raison de la dépendance des énergies par rapport à la surface K, le traitement des problèmes de discontinuité libre avec des méthodes directes de calcul des variations présente beaucoup de difficultés. À moins que les contraintes topologiques soient incluses, l'unique information que de telles énergies soient bornées ne permet pas en général de déduire les propriétés nécessaires de compacité. De Giorgi a proposé d'interpréter K comme ensemble de points de discontinuité de la fonction u, et de placer les problèmes dans un espace de fonctions discontinues, sujet à deux types de conditions. La première est une propriété de structure: si K est l'ensemble de points de discontinuité de la fonction u, alors K peut être interprété comme une hypersurface, et u est différentiable sur $\Omega \backslash K$ de sorte que l'énergie en volume qui dépend de ∇u, puisse être définie. La seconde est une propriété de compacité: il est possible d'utiliser la méthode directe de calcul des variations en obtenant la compacité des suites de fonctions avec énergie bornée. L'espace qui satisfait aux deux conditions est l'espace des fonctions spéciales de variations bornées (space of functions of bounded variation, SBV) définies par De Giorgi et Ambrosio [56]. En particulier, une fonction u appartient à $SBV(\Omega)$ si et seulement si sa dérivée au sens de distributions Du est une mesure bornée qui peut être separée en deux parties, l'une en volume et l'autre en surface. Les détails mathématiques de la définition peuvent être trouvés dans la littérature spécifique, voir, par exemple, le livre de Dal Maso [48]. Ici, nous disons simplement que si $u \in SBV(\Omega)$, l'ensemble K peut être remplacé par un ensemble $S(u)$, caractérisé par une normale théorique ν_n, des traces u^+ et u^- des deux côtés de la discontinuité, et un

gradient approché. Le remplacement conduit à une formulation faible de la forme:

$$E(u) = \int_{\Omega \setminus K} W(x, u, \nabla u)\, d\Omega + \int_{S(u)} \Phi(x, u^+, u^-, \nu_u)\, d\mathcal{H}^{n-1}(K). \tag{1.9}$$

Ambrosio [3, 4] a donné une théorie d'existence pour des problèmes impliquant ces types d'énergies. Divers résultats de régularité montrent que, pour une large classe de problèmes, la solution faible u dans $SBV(\Omega)$ fournit une solution du problème de discontinuité libre correspondant. La théorie d'existence n'exclut pas malheureusement quelques inconvénients sérieux. D'abord, le manque de differentiabilité dans n'importe quelle norme raisonnable implique l'impossibilité d'aborder directement les problèmes d'évolution. En second lieu, de très délicats problèmes numériques apparaissent dans la détermination de la surface de discontinuité inconnue.

Alternativement, on peut faire recours aux techniques numériques de solution et rechercher des approximations variationnelles en employant des énergies différentiables définies sur des fonctions régulières. Cette approche est basée naturellement sur la notion de Γ-convergence de De Giorgi [58]. Une famille (F_ε) de fonctions à valeurs réelles définies sur un espace métrique X Γ-converge vers F quand $\varepsilon \to 0^+$ si pour tout $x \in X$ est satisfaite l'inégalité suivante en limite inférieure:

$$F(x) \leq \liminf_{\varepsilon \to 0^+} F_\varepsilon(x_\varepsilon) \ \text{ quand } \ x_\varepsilon \to x \tag{1.10}$$

et l'existence d'une suite telle que:

$$F(x) = \liminf_{\varepsilon \to 0^+} F_\varepsilon(x_\varepsilon) \ \text{ pour quelque } x_\varepsilon, \text{ avec } \ x_\varepsilon \to x \tag{1.11}$$

La Γ-convergence vérifie des propriétés de compacité, et, selon des hypotèses additionnelles appropriées, est suffisamment robuste pour garantir que les minimums et les minimiseurs pour des problèmes relatifs à F_ε convergent vers les minimums et les minimiseurs relatifs à la fonctionnelle originale, voir le livre de Dal Maso [48].

Une formulation variationnelle pour l'évolution d'une surface de rupture dans un solide fragile et linéairement élastique a été proposée par Francfort et Marigo [68]. Bourdin *et al.* [24] ont combiné cette technique avec la méthode des éléments finis classique pour résoudre avec succès des problèmes de rupture à deux-dimensions. La généralisation à des fonctions vectorialles à fait l'object de démonstrations mathématiques partielles. Ce domaine est actuellement l'object de nombreuses investigations.

Un problème additionnel est lié à l'irréversibilité du processus de rupture. En

tenant compte de l'irréversibilité, on élimine les solutions irréalistes, où des sauts d'un minimiseur à l'autre apparaissent avec l'augmentation du paramètre de chargement. L'irréversibilité est obligatoire dans la définition d'une approche entièrement évolutive. La base théorique des approches évolutives a été développée par Dal Maso *et al.* [50, 49].

Motivé par le travail précédemment mentionné, notre idée d'approcher la rupture quasi-statique est basée sur le concept de minimisation de l'énergie combiné avec la discrétisation par éléments finis et les modèles cohésifs.

Nous avons déjà précisé la nécessité d'identifier la position de la fissure à l'intérieur du corps, qui dans notre approche (décrite en détail dans le Chapitre 3) est confinée aux interfaces des éléments. La restriction réclame l'adaptation du maillage, sous une forme particulière appelée r-adaptivité. La r-adaptivité implique le mouvement des noeuds dans la configuration de référence; i.e., les coordonnées nodales ne sont pas fixes mais peuvent se déplacer afin d'améliorer la discrétisation des éléments finis. L'amélioration du maillage peut être poursuivie de différentes manières, mais ici nous prenons en compte des considérations énergiques; et nous voulons que le maillage optimal soit celui qui réduise au minimum l'énergie totale du corps discrétisé. Ce concept a été exploité par Thoutireddy et Ortiz [182] dans le cadre de l'élasticité non-linéaire. En supposant une dépendance de l'énergie non seulement à l'égard le champ du déplacement, mais également à l'égard des coordonnées nodales d'une discrétisation, il est possible de dériver les équations d'Euler-Lagrange impliquant la stationarité de l'énergie. De telles équations définissent un système non-linéaire qui inclut les résidus standards d'une approche par éléments finis et les résidus "des forces basées sur la configuration", c'est-à-dire, les forces qui expriment l'inhomogénéité du volume induit par la discrétisation. En combination avec la rupture, la contribution des forces configurationnelles est employée pour détecter le chemin optimal de fissure en combinaison avec la discrétisation choisie. Cette recherche est actuellement en cours de développement, mais elle exploite toutes les ressources présentées dans ce travail et représente notre prochaine étape dans les applications des modèles cohésifs.

1.8 Outline

Dans les prochains chapitres nous présentons quatre papiers différents, précédemment publiés dans journaux internationaux. Ils représentent les étapes les plus significatives dans l'élaboration d'une méthodologie numérique profonde basée sur des théories cohésives pour l'analyse de la rupture. La référence complète du papier considéré est

indiquée au début de chaque chapitre.

Le premier chapitre décrit une classe générale de modèles cohésifs tridimensionnels en grandes déformations, avec distinction entre ouverture et glissement, et prise en compte des irréversibilités. En même temps, nous présentons des éléments cohésifs spéciaux compatibles avec une discrétisation tétraédrique du continu et fournissons un exemple d'application à la rupture dynamique des plaques en acier chargées en mode I. Le papier a été développé en collaboration avec Michael Ortiz (Aeronautics and Applied Science Division, California Institute of Technology, Pasadena, CA, USA).

Le deuxième chapitre, également écrit en collaboration avec Michael Ortiz, décrit en détail un algorithme de fragmentation basé sur des structures topologiques de données. Le procédure exécute un remaillage adaptatif à partir d'une maille tétraédrique, introduisant les surfaces cohésives le long des éléments, initialement cohérents. Le remaillage induit des changements topologiques qui permettent de suivre la propagation des fissures, les embranchements, l'intersection des fissures et la formation des fragments. Des exemples d'application concernent la propagation de la rupture fragile dans des plaques de PMMA (polymethilmetacrilate), subissant un chargement dynamique en mode I.

Le troisième chapitre décrit une application intéressante de la procédure à l'analyse des céramiques à haute résistance subissant un chargement dynamique en mode I et II. Nous analysons la réponse dynamique des cylindres en céramique à un essai brésilien dynamique, réalisé pour évaluer la sensibilité du matériau à la vitesse de chargement. Les simulations numériques ont reproduit beaucoup d'aspects expérimentaux, en terme de morphologie de rupture et de réponse globale au chargement de la structure. Le papier est le fruit de la collaboration avec Rena C. Yu et Gonzalo Ruiz, actuellement à l'E.T.S. de Ingenieros de Caminos, Canales y Puertos, Universidad de Castille-La Mancha, Ciudad Real, Espagne.

Le quatrième chapitre développe une application différente des théories cohésives. Nous visons à définir un modèle de matériau avec une microstructure particulière, sous forme de surfaces cohésives équidistantes parallèles (défauts ou failles), capables de décrire le comportement de matériaux fragiles subissant un état compressif global. La structure des failles est reliée à une échelle de longueur. Le modèle présente une structure récursive et différentes échelles de longueur, qui peuvent expliquer les effets de taille typiques de la rupture fragile. Le papier est le résultat de la collaboration avec Michael Ortiz et Sergio Conti, Fachbereich Mathematik, Universität Duisburg-Essen, Allemagne.

Le chapitre final contient des conclusions et des perspectives de nos recherches

actuelles.

Chapter 2

Finite-Deformation Irreversible Cohesive Elements for 3D Crack Propagation Analysis

Abstract

We develop a three-dimensional finite-deformation cohesive element and a class of irreversible cohesive laws which enable the accurate and efficient tracking of dynamically growing cracks. The cohesive element governs the separation of the crack flanks in accordance with an irreversible cohesive law, eventually leading to the formation of free surfaces, and is compatible with a conventional finite element discretization of the bulk material. The versatility and predictive ability of the method is demonstrated through the simulation of a drop-weight dynamic fracture test similar to those reported by Zehnder and Rosakis [208]. The ability of the method to approximate the experimentally observed crack-tip trajectory is particularly noteworthy[1].

2.1 Introduction

The three-dimensional tracking of dynamic cracks in solids undergoing large-scale plasticity has received scant attention in the finite element literature (see [108] for a notable exception). Marusich and Ortiz [107] have developed a method of crack tracking based on continuous and adaptive remeshing, and have applied the method to the simulation of orthogonal high-speed machining. Two conventional crack-growth criteria were employed: the attainment of a critical stress at a critical distance; and the attainment of a critical plastic strain at a critical distance. In this manner, the

[1] **This chapter has been published in a peer reviewed journal paper in 1999**.
M. Ortiz and A. Pandolfi. Finite-Deformation Irreversible Cohesive Elements for Three-Dimensional Crack Propagation Analysis. *International Journal for Numerical Methods in Engineering*, 44, 1267-1282 (1999).

approach is capable of accounting for large-scale plasticity, crack kinking and branching and permits the competition between ductile and brittle fracture mechanisms. However, its generalization to three dimensions is not straightforward, specially as regards the need for automatic remeshing. Perhaps a more fundamental difficulty concerns the applicability of the traditional K and J-based crack-growth initiation and propagation criteria to situations involving large-scale yielding. Even in cases which conform to the assumptions of small-scale fracture mechanics, considerable uncertainties remain as regards the proper choice of crack-growth initiation and propagation criteria that account for loading rate, material interfaces, small crack sizes and other complicating circumstances.

An alternative viewpoint–pioneered by Dugdale [62], Barenblatt [8], Rice [157] and others–regards fracture as a gradual phenomenon in which separation takes place across an extended crack 'tip', or cohesive zone, and is resisted by cohesive tractions. This theory of fracture permits the incorporation into the analysis of *bona fide* fracture parameters such as the spall strength –the peak cohesive traction– and the fracture energy –the area under the cohesive law– of the material. An appealing feature of this approach is that it does not presuppose a particular type of constitutive response in the bulk of the material, the extent of crack growth, or the size of the plastic zone. In addition, the shape and location of successive crack fronts is itself an outcome of the calculations. Yet another noteworthy property of cohesive formulations pointed out by Camacho and Ortiz [30] is that, under dynamic loading conditions, they automatically account for the observed rate-dependency of fracture [154, 97]. Thus, in addition to endowing the solid with an intrinsic length scale, cohesive models also introduce an intrinsic time scale and the corresponding distinction between fast and slow loading rates.

Most cohesive fracture laws proposed to date are reversible and history-independent [166, 119, 130, 17, 158, 137]. These laws presume that the cohesive tractions exactly retrace the loading traction-opening displacement curve upon unloading. While this is rigorously correct when fracture occurs at the atomistic level, where cohesion directly arises from the atomic bonds, most macroscopic decohesion processes may be expected to entail some degree of irreversibility. This requires the formulation of *irreversible* cohesive laws such as proposed by Needleman [121] and Camacho and Ortiz [30]. Our present work extends the formulation of Camacho and Ortiz [30] to three dimensions. Thus, cohesive surfaces are assumed to unload to the origin and mode coupling is accounted for by the simple device of introducing an effective scalar opening displacement.

Cohesive laws have been built into finite element analyses as mixed boundary conditions [79, 32, 119, 120, 121, 196, 149, 185, 187, 186]; or have been embedded into *cohesive finite elements* [193, 137, 30, 198, 199, 200]. These elements are surface-like and are compatible with general bulk finite element discretizations of the solid, including those which account for plasticity and large deformations. Cohesive elements bridge nascent surfaces and govern their separation in accordance with a cohesive law. Camacho and Ortiz [30] have shown that mesh-size independent results are obtained when the mesh adequately resolves the cohesive zone. Here we develop a class of three-dimensional cohesive elements consisting of two six-noded triangular facets. The opening displacements are described by quadratic interpolation within the element. The element is fully compatible with –and may be used to bridge– pairs of tetrahedral elements. Our present work extends the cohesive elements of de Andrés *et al.* [51] to finite deformations. Thus, the elements are endowed with full finite-deformation kinematics and, in particular, are exactly invariant with respect to superposed rigid body translations and rotations.

In Section 2.4 we present a detailed simulation of the drop-weight dynamic fracture tests of Zehnder and Rosakis [208] which demonstrates the predictive ability of the formulation. The ability of the method to reproduce the salient trends in the experimentally observed crack tip trajectory is particularly noteworthy.

2.2 Finite-deformation irreversible cohesive laws

By way of general framework, consider a body occupying an initial configuration $B_0 \subset R^3$. The body undergoes a motion described by a deformation mapping $\boldsymbol{\varphi} : B_0 \times [0,T] \to R^3$, where $[0,T]$ is the elapsed time interval. Let $\boldsymbol{F}$ be the attendant deformation gradients and $\boldsymbol{P}$ the first Piola-Kirchhoff stress tensor (cf, e. g., [106]).

Suppose now that the body is traversed by a cohesive surface S_0, Fig. 2.1. Furthermore, orient S_0 by choosing a unit normal $\boldsymbol{N}$. For simplicity, assume that the cohesive surface then partitions the body into two subbodies $B_0^{\pm}$, lying on the plus and minus sides of S_0, denoted $S_0^{\pm}$, respectively. The power expended by the body forces $\rho_0 \boldsymbol{b}$ and the boundary tractions $\boldsymbol{t}$ is

$$\dot{W} = \sum_{\pm} \int_{B_0^{\pm}} \rho_0 \boldsymbol{b} \cdot \dot{\boldsymbol{\varphi}} dV_0 + \sum_{\pm} \int_{\partial B_0^{\pm}} \boldsymbol{t} \cdot \dot{\boldsymbol{\varphi}} dS_0 \tag{2.1}$$

where the sum extends over the two subbodies defined by the cohesive surface. Likewise,

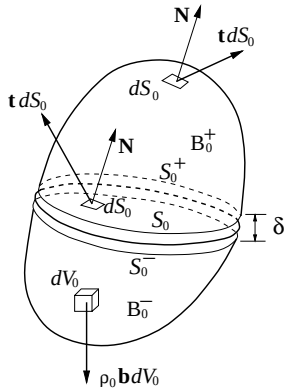

Figure 2.1: Cohesive surface traversing a 3D body.

the kinetic energy of the body is

$$K = \sum_{\pm} \int_{B_0^{\pm}} \frac{1}{2} \rho_0 |\dot{\boldsymbol{\varphi}}|^2 dV_0 \tag{2.2}$$

The deformation power, namely, the part of the power expended on the solid which is not expended in raising its kinetic energy, is, therefore,

$$P^D = \dot{W} - \dot{K} = \sum_{\pm} \int_{B_0^{\pm}} \rho_0 (\boldsymbol{b} - \ddot{\boldsymbol{\varphi}}) \cdot \dot{\boldsymbol{\varphi}} dV_0 + \sum_{\pm} \int_{\partial B_0^{\pm}} \boldsymbol{t} \cdot \dot{\boldsymbol{\varphi}} dS_0 \tag{2.3}$$

Additionally, we assume balance of linear momentum, which requires

$$\nabla_0 \cdot \boldsymbol{P} = \rho_0 (\ddot{\boldsymbol{\varphi}} - \boldsymbol{b}), \qquad \text{in } B_0^{\pm} \tag{2.4}$$

$$\boldsymbol{P} \cdot \boldsymbol{N} = \boldsymbol{t} \qquad \text{on } \partial B_0^{\pm} \tag{2.5}$$

$$[\![\boldsymbol{P} \cdot \boldsymbol{N}]\!] = [\![\boldsymbol{t}]\!] = \boldsymbol{0} \qquad \text{on } S_0^{\pm} \tag{2.6}$$

Here, $\nabla_0 \cdot$ signifies the material divergence over B_0 and $\boldsymbol{N}$ is the unit normal. Inserting (2.4) into (2.3) and making use of (2.5) and (2.6) leads to the deformation power identity

$$P^D = \sum_{\pm} \int_{B_0^{\pm}} \boldsymbol{P} \cdot \dot{\boldsymbol{F}} dV_0 + \int_{S_0} \boldsymbol{t} \cdot [\![\dot{\boldsymbol{\varphi}}]\!] dS_0 \tag{2.7}$$

This expression generalizes the conventional deformation power identity (cf, e. g., [106]) to a body containing a cohesive surface.

As is evident from (2.7), the presence of a cohesive surface results in the addition of a new term to the deformation power identity. The duality or work-conjugacy relations between stress and deformation measures may also be discerned from (2.7): as in conventional solids, the first Piola-Kirchhoff stress tensor $\boldsymbol{P}$ does work on the deformation gradients $\boldsymbol{F}$ over the bulk of the body. In addition, it follows that the tractions $\boldsymbol{t}$ do work on the displacement jumps

$$\boldsymbol{\delta} = [\![\boldsymbol{\varphi}]\!] \tag{2.8}$$

or 'opening displacements' over the cohesive surface.

The preceding work-conjugacy relations set the stage for the development of a general theory of cohesive in solids. In this theory, the opening displacements $\boldsymbol{\delta}$ play the role of a deformation measure, with the tractions $\boldsymbol{t}$ furnishing the conjugate stress measure. It is worth noting in this regard that $\boldsymbol{\delta}$ vanishes identically when the body undergoes a rigid translation, as required of a proper deformation measure. For simplicity, we shall assume that the behavior of cohesive surfaces is local. Consequently, for the purpose of formulating cohesive laws we can confine our attention to one point on the cohesive surface.

We expect the cohesive behavior to be different for opening and sliding. In order to account for this difference, it becomes necessary to keep track of the deformed geometry of the cohesive surface. However, this task is compounded by the discontinuous behavior of the deformation mapping. One scheme for identifying a unique deformed configuration S of the cohesive surface is to introduce the mean deformation mapping

$$\bar{\boldsymbol{\varphi}} = \frac{1}{2}(\boldsymbol{\varphi}^+ + \boldsymbol{\varphi}^-) \tag{2.9}$$

over S_0, and to set $S \equiv \bar{\boldsymbol{\varphi}}(S_0)$. Evidently, the full deformation mapping may be recovered from (2.8) and (2.9) through the identities

$$\boldsymbol{\varphi}^{\pm} = \bar{\boldsymbol{\varphi}} \pm \frac{1}{2}\boldsymbol{\delta} \tag{2.10}$$

It should be noted that for most materials systems of practical interest the opening displacements $\boldsymbol{\delta}$ across cohesive zones, e. g., at the tip of a crack, are exceedingly small, which effectively eliminates any ambiguities in the definition of the deformed cohesive surface.

Equipped with these conventions, it is now possible to introduce a unit normal $\boldsymbol{n}$ to S, which we take to point from $\boldsymbol{\varphi}^-(S_0)$ to $\boldsymbol{\varphi}^+(S_0)$. We shall assume throughout that

S remains smooth and, therefore, $\boldsymbol{n}$ is well-defined everywhere. Given a vector field $\boldsymbol{u}$ over S, its normal and tangential components are

$$u_n = \boldsymbol{u} \cdot \boldsymbol{n}, \qquad \boldsymbol{u}_S = \boldsymbol{u} - u_n \boldsymbol{n} = (\boldsymbol{I} - \boldsymbol{n} \otimes \boldsymbol{n})\boldsymbol{u}, \tag{2.11}$$

respectively. In addition, we shall denote by $\nabla_S \boldsymbol{u}$ the surface gradient of $\boldsymbol{u}$. Given a parametrization of S by curvilinear coordinates (s_1, s_2), the components of $\nabla_S \boldsymbol{u}$ are simply the covariant derivatives of the components of $\boldsymbol{u}$ (cf, e. g., [106]).

We postulate the existence of a free energy density per unit underformed area over S_0 of the general form

$$\phi = \phi(\boldsymbol{\delta}, \theta, \boldsymbol{q}; \nabla_{S_0} \bar{\boldsymbol{\varphi}}) \tag{2.12}$$

where θ is the local temperature and $\boldsymbol{q}$ is some suitable collection of internal variables which describe the inelastic processes attendant to decohesion. The additional dependence on $\nabla_{S_0} \bar{\boldsymbol{\varphi}}$ is geometrical in nature since a variation of $\bar{\boldsymbol{\varphi}}$ at constant $\boldsymbol{\delta}$ does not entail any surface decohesion. Given a parametrization (S_1, S_2) of S_0, the vectors $\bar{\boldsymbol{\varphi}}_{,1}$ and $\bar{\boldsymbol{\varphi}}_{,2}$ are tangent to S. Consequently, the unit normal $\boldsymbol{n}$ is the unit vector orthogonal to both $\bar{\boldsymbol{\varphi}}_{,1}$ and $\bar{\boldsymbol{\varphi}}_{,2}$. The surface deformation is measured by the surface Cauchy-Green deformation tensor

$$\boldsymbol{C}_{S_0} = (\nabla_{S_0} \bar{\boldsymbol{\varphi}})^T \nabla_{S_0} \bar{\boldsymbol{\varphi}} \tag{2.13}$$

Evidently, the geometrical information conveyed by $\nabla_{S_0} \bar{\boldsymbol{\varphi}}$ is required in order to keep track of the normal direction and possibly of special material directions within the cohesive surface, such as easy glide directions in crystalline surfaces.

By recourse to Coleman and Noll's method (e. g., [99, 100]) it is possible to show that the cohesive law takes the form

$$\boldsymbol{t} = \frac{\partial \phi}{\partial \boldsymbol{\delta}} \tag{2.14}$$

The potential structure of the cohesive law is a consequence of the first and second laws of thermodynamics. The evolution of the internal variables $\boldsymbol{q}$ is governed by a set of kinetic relations of the general form

$$\dot{\boldsymbol{q}} = \mathbf{f}(\boldsymbol{\delta}, \theta, \boldsymbol{q}) \tag{2.15}$$

In the sequel we shall restrict our attention to isothermal processes and dependencies on θ will be omitted for simplicity. A key benefit of the potential structure of the

cohesive law (2.14) is that it reduces the identification of the cohesive law from the three independent functions $\boldsymbol{t}$ to the single function scalar ϕ.

The cohesive free energy ϕ is subject to the restrictions imposed by material frame indifference, namely,

$$\phi(\boldsymbol{\delta}^*, \boldsymbol{q}^*; \nabla_{S_0}\bar{\boldsymbol{\varphi}}^*) = \phi(\boldsymbol{\delta}, \boldsymbol{q}; \nabla_{S_0}\bar{\boldsymbol{\varphi}}) \tag{2.16}$$

where

$$\boldsymbol{\delta}^* = \boldsymbol{R}\boldsymbol{\delta}, \qquad \nabla_{S_0}\bar{\boldsymbol{\varphi}}^* = \boldsymbol{R}\nabla_{S_0}\bar{\boldsymbol{\varphi}} \tag{2.17}$$

and $\boldsymbol{R} \in SO(3)$ is an arbitrary rotation. The precise expression for $\boldsymbol{q}^*$ depends on the tensorial nature of $\boldsymbol{q}$. For simplicity, we shall assume that the internal variables $\boldsymbol{q}$ are scalar or otherwise invariant under superposed rigid rotations. The most general dependence of ϕ on $\boldsymbol{\delta}$ and $\nabla_{S_0}\bar{\boldsymbol{\varphi}}$ consistent with these restrictions is

$$\phi = \phi(\delta_n, \boldsymbol{\delta} \cdot \nabla_{S_0}\bar{\boldsymbol{\varphi}}, \boldsymbol{q}; \boldsymbol{C}_{S_0}) \tag{2.18}$$

This form of the free energy allows for coupling between the cohesive surface deformation, as measured by $\boldsymbol{C}_{S_0}$, and decohesion. For simplicity, in the sequel we shall assume that no such coupling exists, i. e., that the cohesive response is independent of the stretching and shearing of the cohesive surface, leading to a class of free energies of the simpler form

$$\phi = \phi(\delta_n, \boldsymbol{\delta} \cdot \nabla_{S_0}\bar{\boldsymbol{\varphi}}, \boldsymbol{q}) \tag{2.19}$$

Further simplifications arise from material symmetry. Assume, for instance, that the cohesive surface is isotropic, i. e., that the resistance to sliding is independent of the direction of sliding. This requires that

$$\phi = \phi(\delta_n, \delta_S, \boldsymbol{q}) \tag{2.20}$$

where we write

$$\delta_S = |\boldsymbol{\delta}_S| \tag{2.21}$$

Interestingly, the free energy (2.20) depends only on the geometry of S through its unit normal $\boldsymbol{n}$. In this simple case, the cohesive law (2.14) reduces to

$$\boldsymbol{t} = \frac{\partial \phi}{\partial \delta_n}(\delta_n, \delta_S, \boldsymbol{q})\, \boldsymbol{n} + \frac{\partial \phi}{\partial \delta_S}(\delta_n, \delta_S, \boldsymbol{q})\, \frac{\boldsymbol{\delta}_S}{\delta_S} \tag{2.22}$$

To further simplify the formulation of mixed-mode cohesive laws, we follow Camacho

and Ortiz [30] and introduce an effective opening displacement

$$\delta = \sqrt{\beta^2 \delta_S^2 + \delta_n^2} \tag{2.23}$$

Evidently, the parameter β assigns different weights to the sliding and normal opening displacements. As simple model of cohesion is then obtained by assuming that free energy potential ϕ depends on $\boldsymbol{\delta}$ only through the effective opening displacement δ, i. e.,

$$\phi = \phi(\delta, \boldsymbol{q}) \tag{2.24}$$

Under these conditions, the cohesive law (2.22) reduces to

$$\boldsymbol{t} = \frac{t}{\delta}(\beta^2 \boldsymbol{\delta}_S + \delta_n \boldsymbol{n}) \tag{2.25}$$

where

$$t = \frac{\partial \phi}{\partial \delta}(\delta, \boldsymbol{q}) \tag{2.26}$$

is a scalar effective traction. It follows from (2.23) and (2.25) that the effective traction is

$$t = \sqrt{\beta^{-2} |\boldsymbol{t}_S|^2 + t_n^2} \tag{2.27}$$

This relation shows that β defines the ratio between the shear and the normal critical tractions. In brittle materials, this ratio may be estimated by imposing lateral confinement on specimens subjected to high-strain-rate axial compression [33, 34].

It bears emphasis that, upon closure, the cohesive surfaces are subject to the contact unilateral constraint, including friction. We regard contact and friction as independent phenomena to be modelled outside the cohesive law. Friction may significantly increase the sliding resistance in closed cohesive surfaces. In particular, the presence of friction may result in a steady–or even increasing–frictional resistance while the normal cohesive strength simultaneously weakens.

Fig. 2.2 depicts the class of irreversible cohesive laws envisioned here. Irreversibility manifests itself upon unloading. Therefore, an appropriate choice of internal variable is the maximum attained effective opening displacement $\delta_{\max}$. Loading is then characterized by the conditions: $\delta = \delta_{\max}$ and $\dot{\delta} \geq 0$. Conversely, we shall say that the cohesive surface undergoes unloading when it does not undergo loading. We assume the existence of a loading envelop defining a relation between t and δ under conditions of loading. A simple and convenient relation is furnished by Smith and Ferrante's

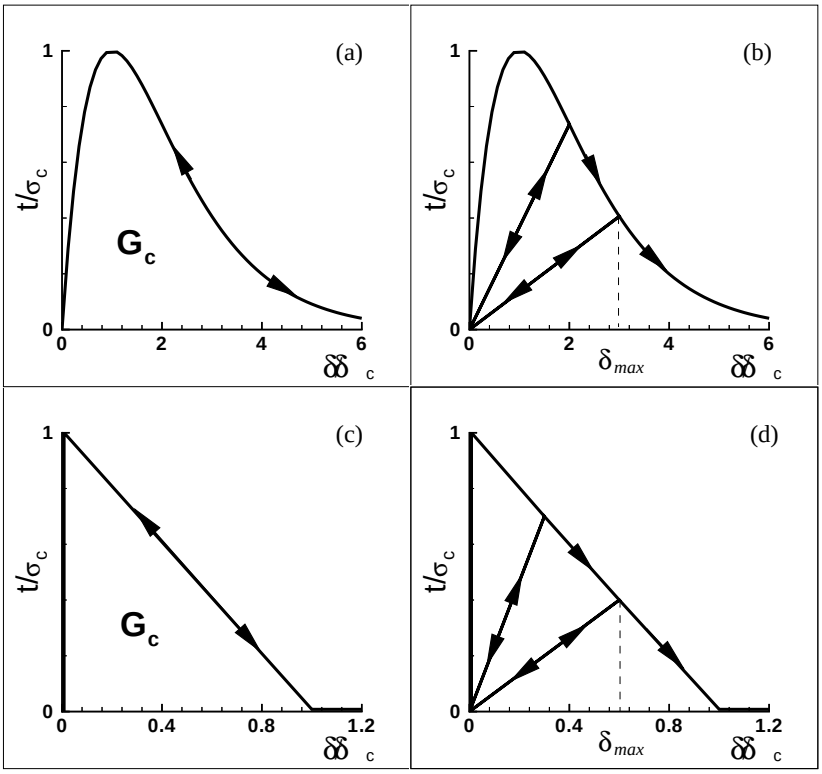

Figure 2.2: Two simple choices of cohesive law expressed in terms of an effective opening displacement δ and traction t. (a) Loading envelop of the Smith-Ferrante type; (b) Loading-unloading rule from Smith-Ferrante envelop; (c) Linearly decreasing loading envelop; (d) Loading-unloading rule from linearly decreasing loading envelop.

universal binding law, Fig. 2.2a,

$$t = e\sigma_c \frac{\delta}{\delta_c} \mathrm{e}^{-\delta/\delta_c}, \qquad \text{if} \qquad \delta = \delta_{\max} \text{ and } \dot{\delta} \geq 0 \tag{2.28}$$

where $e \approx 2.71828$ is the e-number, σ_c is the maximum cohesive normal traction and δ_c is a characteristic opening displacement. The potential corresponding to (2.28) is

$$\phi = e\sigma_c \delta_c \left[1 - \left(1 + \frac{\delta}{\delta_c}\right) \mathrm{e}^{-\delta/\delta_c}\right] \tag{2.29}$$

Following Camacho and Ortiz [30] we shall assume unloading to the origin, Fig. 2.2, giving

$$t = \frac{t_{\max}}{\delta_{\max}} \delta, \qquad \text{if} \qquad \delta < \delta_{\max} \text{ or } \dot{\delta} < 0 \tag{2.30}$$

For the present model, the kinetic relations (2.15) reduce to

$$\dot{\delta}_{\max} = \begin{cases} \dot{\delta}, & \text{if } \delta = \delta_{\max} \text{ and } \dot{\delta} \geq 0; \\ 0, & \text{otherwise,} \end{cases} \tag{2.31}$$

Evidently, the cohesive behavior just described is rate-independent. Two types of loading envelops and the corresponding loading-unloading paths are shown in Fig. 2.2.

In nonlinear elastic materials, a standard application of the J-integral [157] establishes a link between the critical energy release rate G_c for crack propagation and the cohesive law. For simplicity, let the cohesive surface S_0 be flat and choose a local orthonormal reference frame such that the basis vector $\boldsymbol{e}_1$ points in the direction of propagation of the crack front, $\boldsymbol{e}_1$ is aligned with the crack front direction and $\boldsymbol{e}_3$ coincides with the unit normal $\boldsymbol{N}$, Fig. 2.3. Choosing a contour Γ for the evaluation of the J-integral which surrounds the cohesive zone gives

$$G_c = \int_0^R \boldsymbol{t} \cdot \boldsymbol{\delta}_{,1} \, dx_1 = \int_0^R t\delta_{,1} \, dx_1 \tag{2.32}$$

where R is the cohesive zone length and we have made use of (2.23) and (2.25). A change of variables enables the second of (2.32) to be written in the form

$$G_c = \int_0^\infty t d\delta \equiv \phi_\infty \tag{2.33}$$

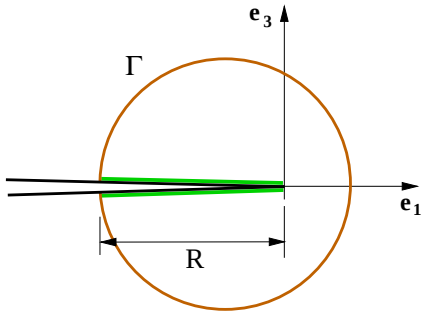

Figure 2.3: Computation of the J-integral along a surface Γ which surrounds the cohesive zone R.

For the particular case of (2.28), (2.33) gives

$$G_c = e\sigma_c\delta_c \tag{2.34}$$

which relates σ_c and δ_c to the fracture energy G_c.

For purposes of display of results, we shall find it convenient to define a damage parameter

$$D = \frac{\phi(\delta_{max})}{G_c} \tag{2.35}$$

Evidently, D ranges from 0 to 1, with these limits corresponding to an intact and a fully decohered cohesive surface, respectively. Furthermore, it follows from (2.31) that

$$\dot{D} \geq 0 \tag{2.36}$$

as befits the irreversibility of damage.

2.3 Finite element implementation

A particularly appealing aspect of cohesive laws is that they fit naturally within the conventional framework of finite element analysis. One possible approach is to implement the cohesive law as a mixed boundary condition, relating tractions to displacements at boundaries or interfaces [79, 32, 119, 120, 121, 149, 185, 187, 186]. Here, by contradistinction, we follow Willam [193], Ortiz and Suresh [137], and Xu and Needleman [198], and directly embed the cohesive law into surface-like finite elements, leading to the formulation of so-called 'cohesive' elements.

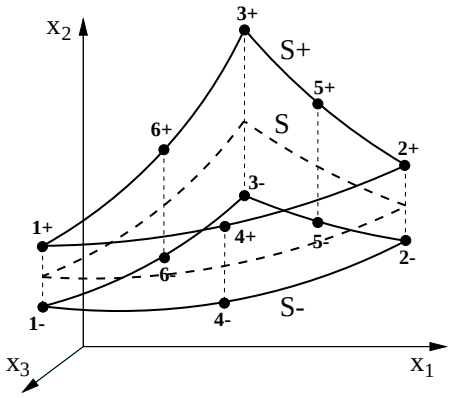

Figure 2.4: Geometry of cohesive element. The surfaces S^- and S^+ coincide in the reference configuration of the solid.

The class of elements considered consists of two surface elements which coincide in space in the reference configuration of the solid, Fig. 2.4. Each of the surface elements has n nodes. The total number of nodes of the cohesive element is, therefore, $2n$. The particular triangular geometry depicted in Fig. 2.4 is compatible with three-dimensional tetrahedral elements, Fig. 2.5. The compatibility of cohesive elements with general classes of bulk elements and constitutive behaviors is particularly noteworthy.

We shall denote by $N_a(s_1, s_2)$, $a = 1, \ldots, n$ the standard shape functions of each of the constituent surface elements. The coordinates (s_1, s_2) are the natural coordinates of each of the surface elements in some convenient standard configuration $\hat{S}$, e. g., that shown in Fig. 2.6a. We shall designate one of the surface elements as S^- and the remaining one as S^+.

As noted in Section 2.2, the behavior of a cohesive surface may be expected to differ markedly depending on whether the surface undergoes sliding or normal separation. This requires the continuous tracking of the normal and tangential directions to the surface. In particular, since S^- and S^+ may diverge by a finite distance the definition of a unique normal direction $\boldsymbol{n}$ is to some extent a matter of convention. In keeping with the framework developed in the preceding section, all geometrical operations such as the computation of the normal are carried out on the *middle surface* S of the element, Fig. 2.6b, defined parametrically as

$$\boldsymbol{x}(\boldsymbol{s}) = \sum_{a=1}^{n} \bar{\boldsymbol{x}}_a N_a(\boldsymbol{s}) \tag{2.37}$$

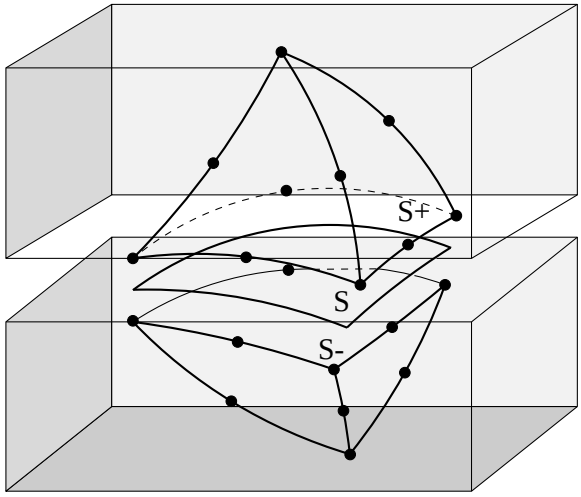

Figure 2.5: Assembly of 12-node triangular cohesive element and two 10-node tetrahedral elements.

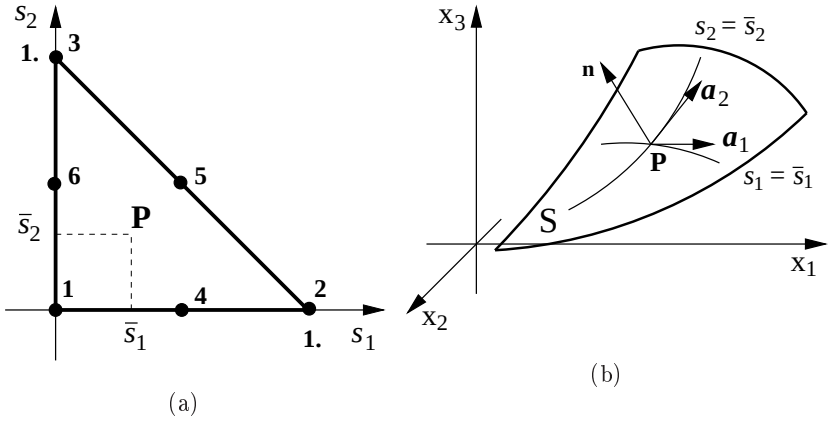

Figure 2.6: (a) Standard element configuration and natural coordinate system; (b) Deformed middle surface S and corresponding curvilinear coordinate system.

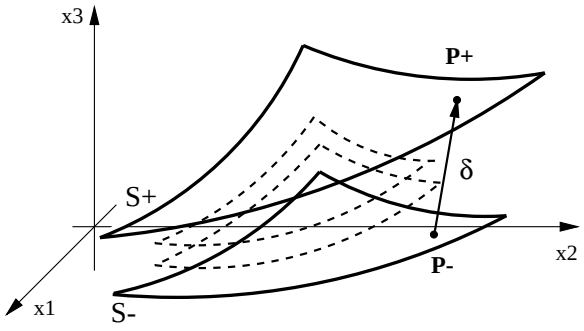

Figure 2.7: Opening displacement.

where

$$\bar{\boldsymbol{x}}_a = \frac{1}{2}(\boldsymbol{x}_a^+ + \boldsymbol{x}_a^-) \tag{2.38}$$

and $\boldsymbol{x}_a^\pm$, $a = 1, \ldots, n$ are the coordinates of the nodes in the deformed configuration of the element. The natural coordinates (s_1, s_2) thus define a convenient system of curvilinear coordinates for the middle surface of the element. The corresponding tangent basis vectors are

$$\boldsymbol{a}_\alpha(\boldsymbol{s}) = \boldsymbol{x}_{,\alpha}(\boldsymbol{s}) = \sum_{a=1}^{n} \bar{\boldsymbol{x}}_a N_{a,\alpha}(\boldsymbol{s}) \tag{2.39}$$

Here and subsequently, Greek indices are assigned the range $(1, 2)$ and a comma signifies partial differentiation. The unit normal to S is

$$\boldsymbol{n} = \frac{\boldsymbol{a}_1 \times \boldsymbol{a}_2}{|\boldsymbol{a}_1 \times \boldsymbol{a}_2|} \tag{2.40}$$

which, conventionally, points from S^- to S^+.

The opening displacement vector in the deformed configuration is, Fig. 2.7,

$$\boldsymbol{\delta}(\boldsymbol{s}) = \sum_{a=1}^{n} [\![\boldsymbol{x}_a]\!] N_a(\boldsymbol{s}) \tag{2.41}$$

where

$$[\![\boldsymbol{x}_a]\!] = \boldsymbol{x}_a^+ - \boldsymbol{x}_a^- \tag{2.42}$$

Evidently, $\boldsymbol{\delta}$ remains invariant upon superposed rigid translations of the element.

For the cohesive model developed in Section 2.2, the cohesive tractions per unit

undeformed area follow as

$$\boldsymbol{t} = \frac{t}{\delta}[\beta^2\boldsymbol{\delta} + (1-\beta^2)(\boldsymbol{\delta}\cdot\boldsymbol{n})\boldsymbol{n}] = \boldsymbol{t}(\boldsymbol{\delta},\boldsymbol{n}) \tag{2.43}$$

where the last identity has been inserted in order to highlight the dependence of $\boldsymbol{t}$ on the normal $\boldsymbol{n}$. This dependence needs to be carefully accounted for in a finite deformation setting as it leads to geometrical terms in the tangent stiffness matrix. The nodal forces now follow from the tractions as

$$f_{ia}^{\pm} = \mp \int_{S_0} t_i N_a dS_0 \tag{2.44}$$

It should be noted that the integral extends over the undeformed surface of the element in its reference configuration. As is costumary in isoparametric finite elements, the integral may conveniently be approximated by recourse to numerical quadrature. The tangent stiffness matrix follows by consistent linearization of (2.44), with the result

$$K_{iakb}^{\pm\pm} = \frac{\partial f_{ia}^{\pm}}{\partial x_{kb}^{\pm}} = \mp\mp \int_{S_0} \frac{\partial t_i}{\partial \delta_k} N_a N_b dS_0 \mp \frac{1}{2}\int_{S_0} \frac{\partial t_i}{\partial n_p}\frac{\partial n_p}{\partial \bar{x}_{kb}} N_a dS_0 \tag{2.45}$$

A trite calculation gives

$$\frac{\partial n_p}{\partial \bar{x}_{kb}} = \frac{e_{krs}}{2|\boldsymbol{a}_1\times\boldsymbol{a}_2|}(a_{2r}N_{b,1} - a_{1r}N_{b,2})(\delta_{ps} - n_p n_s) \tag{2.46}$$

Evidently, the geometrical terms in (2.45) render the stiffness matrix unsymmetric.

2.4 Simulation of the drop-weight dynamic fracture test

Finally, we present a three-dimensional simulation of the drop-weight dynamic fracture tests which demonstrates the scope and versatility of the cohesive elements and cohesive laws described above. This example effectively tests the ability of the method to track dynamically growing three-dimensional cracks in a solid undergoing finite deformations. The calculations presented here are primarily intended as a numerical test of the formulation and not as a comprehensive investigation of three-dimensional aspects of dynamic crack growth in steel. A more systematic numerical study of such aspects may be found elsewhere [108].

The assumed test configuration is shown in Fig. 2.8. A rectangular three-point bend specimen is subjected to dynamic loading as imparted by a falling weight which

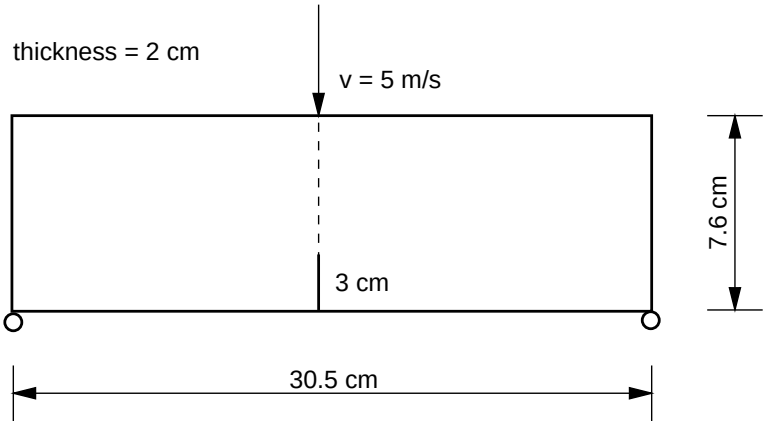

Figure 2.8: Geometry of three-point bend test specimen.

Plasticity 10-nodes tetrahedron		**Cohesive 12-nodes element**	
Mass density	ρ = 7830 kg/m^3	Maximum cohesive stress	σ_c = 6000 MPa
Young's modulus	E = 200 GPa	Critical opening displacement	δ_c = 5.46 x 10^{-6}
Poisson's ratio	ν = 0.3	Weighting coefficient	β = 0.707
Initial yield stress	σ_0 = 2000 MPa		
Reference plastic strain	ε_0 = 0.01		
Reference plastic strain Rate	$\dot{\varepsilon}_0$ = 0.001/s		
Rate sensitivity exponent	m = 70		
Hardening exponent	n = 100		

Figure 2.9: Table of assumed material constants for C-300 steel.

strikes at the midsection of the specimen. The specimen has an initial precrack 3 cm deep within its midsection sharpened by fatigue, Fig. 2.8. The effect of the weight is approximated by prescribing a constant velocity of 5 m/s at the point of contact. Because of the impulsive nature of the motion, the problem is ideally suited to explicit dynamics. In calculations we employ the explicit member of Newmark's algorithm (e. g., [18, 82]). We have found that in explicit calculations a cohesive law of the form shown in Fig. 2.2d is preferable to one of the type Fig. 2.2b, as the initial elastic slope in the latter may place stringent restrictions on the stable time step for explicit integration. The material is a brittle C-300 steel, which we assume to obey J_2-plasticity with power-law hardening and rate dependency (e. g., [46, 107, 31]). The material constants used in calculations are collected in Fig. 2.9.

The computational mesh is shown in Fig. 2.10. In view of the brittleness of the C-300 steel under consideration, the extent of shear lip formation may be expected to be small. Consequently, the crack surface may be approximated as remaining essentially planar and confined to the midsection of the specimen. In order to allow for dynamic crack growth, we tile the midsection of the specimen with cohesive elements such as described in Section 2.3. All surfaces and the interior of the specimen are meshed automatically by the advancing front method. The mesh is designed so as to be fine and nearly uniform on and in the vicinity of the crack plane, and to gradually coarsen away from the crack plane up to a large uniform mesh size, Fig. 2.10. The volume elements are 10-node quadratic tetrahedra and the state variables are updated by recourse to the method of extension of Cuitiño and Ortiz [46]. Overall, the computational mesh comprises 8084 nodes, 4410 tetrahedra and 768 cohesive elements. The minimum mesh size is 2 mm. Based on this dimension and the elastic moduli, a stable time step for explicit integration may be conservatively estimated at $\Delta t = 0.012$ μs.

The deformed mesh after the passage of 2.4 ms is shown to scale in Fig. 2.11. At this time, the specimen is clearly split into two identical fragments. The ability of the cohesive elements to simulate the emergence of the crack through the upper surface of the specimen is noteworthy. The finite rotations undergone by the specimen should also be carefully noted.

Details of the crack growth process are shown in Figs. 2.12 and 2.13. Fig. 2.12 depicts contours of the damage variable D, eq. 2.35, at four difference stages of growth. As may be recalled, a value of $D = 0$ denotes the absence of cracking, whereas the limiting value of $D = 1$ denotes a fully formed crack. The narrow transition zone between these two limiting values may be regarded as a smeared crack tip, or cohesive

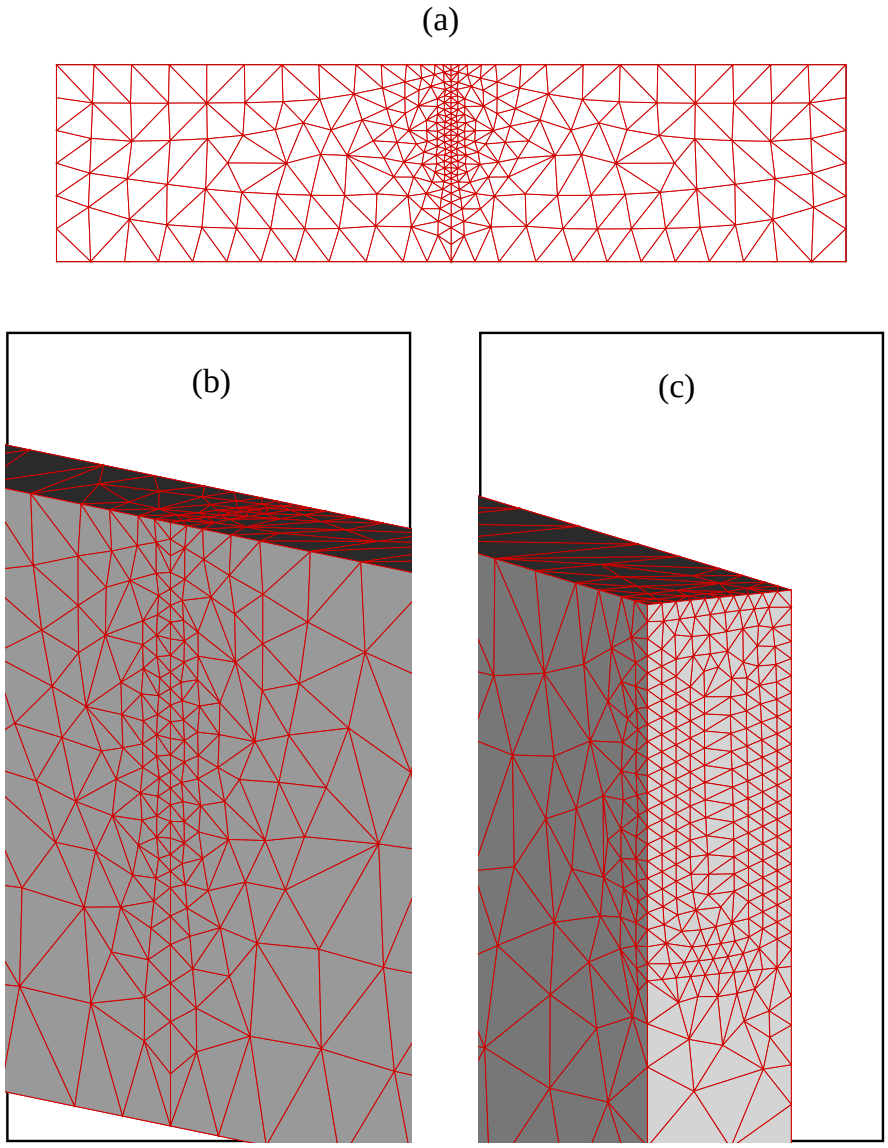

Figure 2.10: Computational mesh comprising 8084 nodes, 4410 tetrahedra and 768 cohesive elements.

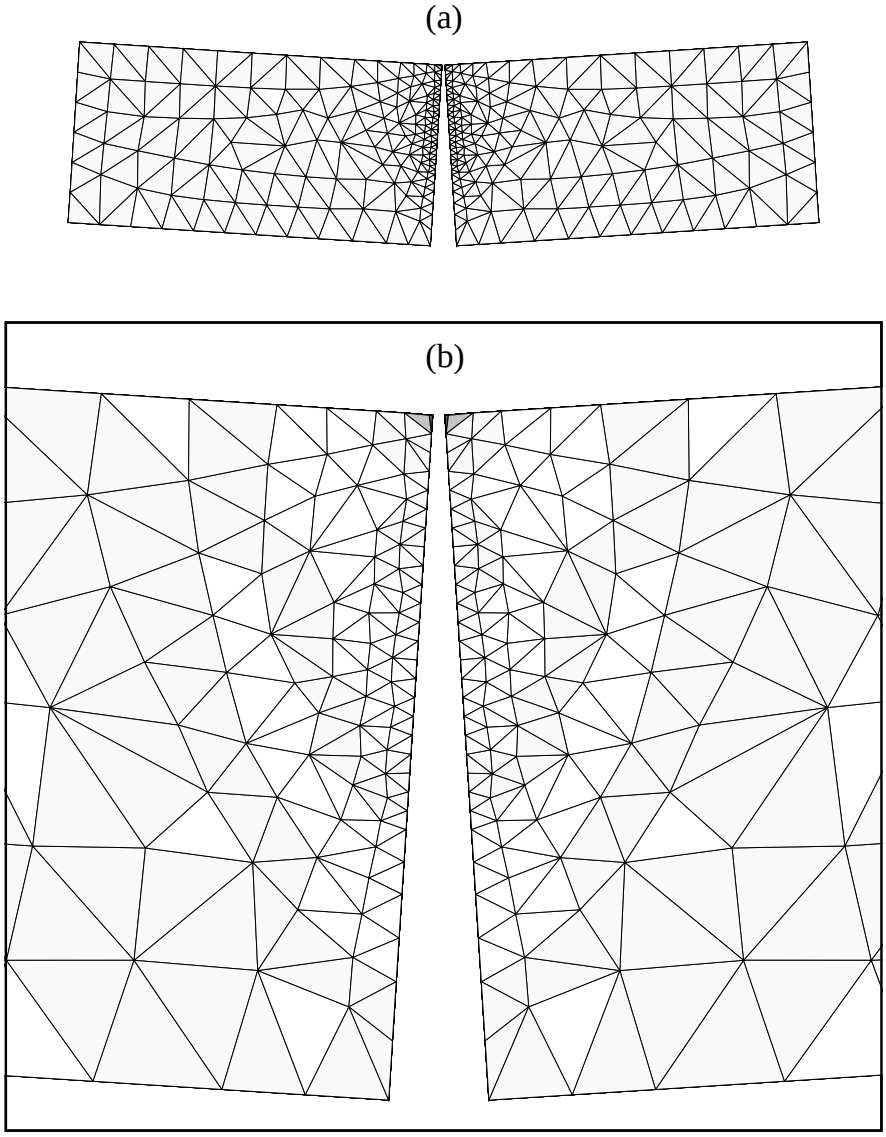

Figure 2.11: Deformed geometry of the specimen after 2400 microseconds.

zone. It is observed in Fig. 2.12 that the crack front develops a small curvature as it propagates and it lags behind somewhat near the free surface as a consequence of enhanced plastic activity in that region. However, these effects are not strong as expected from the brittleness of C-300 steel.

The trajectory and speed of the central point of the crack front are plotted in Fig. 2.13. The trajectory of the crack, Fig. 2.13a, is seen to be smooth initially and becomes jerky during later stages of growth. The velocity history of the crack front as computed by a three-point numerical differentiation formula is shown in Fig. 2.13b. For purposes of comparison, Fig. 2.13c shows the experimentally determined velocity history for a similar drop-weight test [208]. Remarkably, the numerical simulation captures some of the salient features of the experimental record such as the initial acceleration of the crack tip; the subsequent oscillations about a plateau; and the final drop in velocity as the crack joins up with the top surface of the specimen.

2.5 Summary and Conclusions

We have developed a three-dimensional finite-deformation cohesive element and a class of irreversible cohesive laws which enable the accurate and efficient tracking of dynamically growing cracks. The cohesive element governs the separation of the crack flanks in accordance with an irreversible cohesive law, eventually leading to the formation of free surfaces, and is compatible with a conventional finite element discretization of the bulk material. Our present work extends the cohesive model of Camacho and Ortiz [30] to three dimensions. Thus, cohesive surfaces are assumed to unload to the origin and mode coupling is accounted for by the simple device of introducing an effective scalar opening displacement. The cohesive elements developed here are endowed with full finite kinematics, and in this important respect they generalize the cohesive elements of de Andrés *et al.* [51]. The versatility and predictive ability of the method has been demonstrated through the simulation of a drop-weight dynamic fracture test similar to that reported by Zehnder and Rosakis [208]. The ability of the method to approximate the experimentally observed crack-tip trajectory is particularly noteworthy.

Acknowledgements

This research has been supported by the Office of Naval Research through grant N00014-95-1-0453.

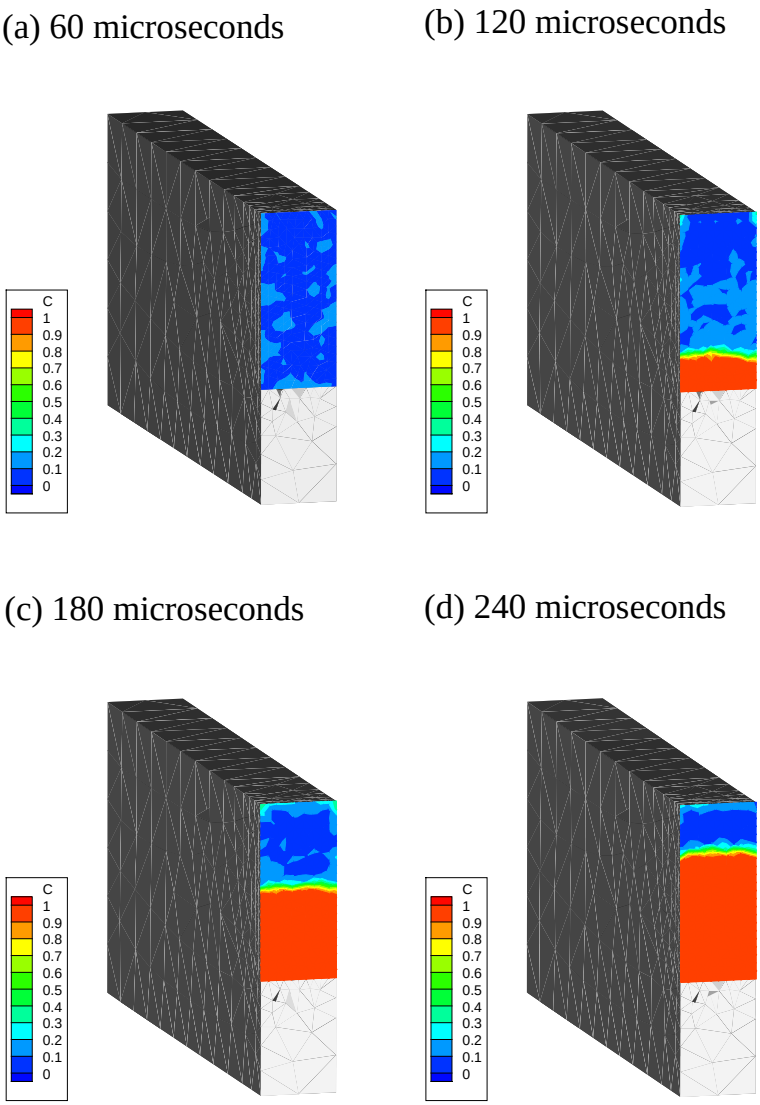

Figure 2.12: Contour levels of the damage variable D at four different stages of crack growth.

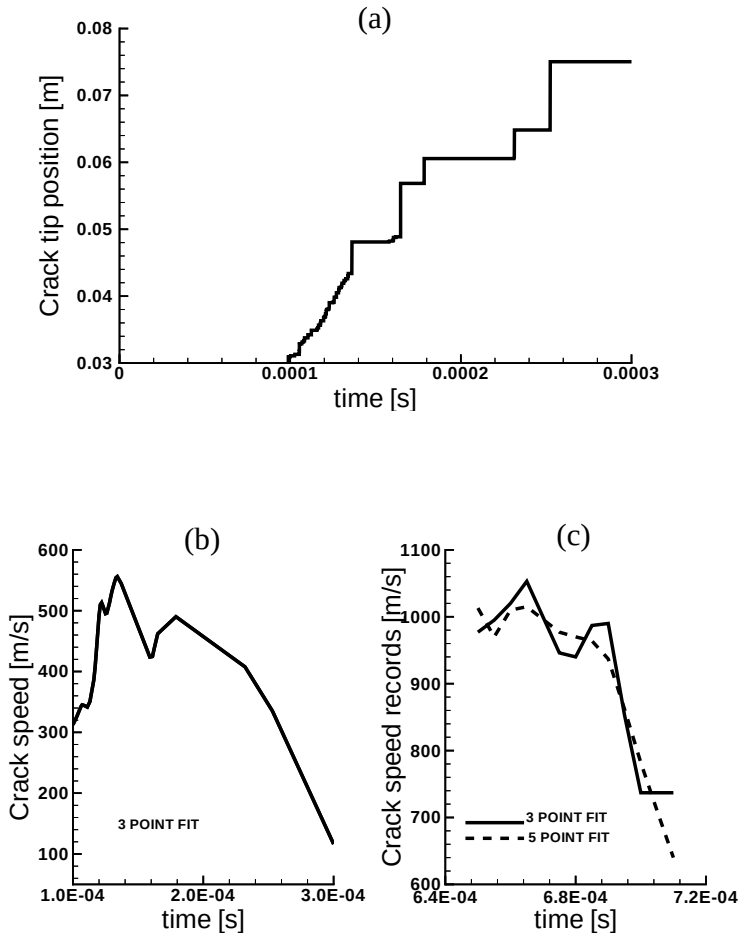

Figure 2.13: (a) Computed crack-tip trajectory; (b) crack-tip speed computed by smoothing and numerical differentiation of the crack tip trajectory; (c) experimental crack-tip velocity [208].

Chapter 3

An Efficient Adaptive Procedure for 3D Fragmentation Simulations

Abstract

We present a simple set of data structures, and a collection of methods for constructing and updating the structures, designed to support the use of cohesive elements in simulations of fracture and fragmentation. Initially all interior faces in the triangulation are perfectly coherent, i. e., conforming in the usual finite element sense. Cohesive elements are inserted adaptively at interior faces when the effective traction acting on those face reaches the cohesive strength of the material. The insertion of cohesive elements changes the geometry of the boundary and, frequently, the topology of the model as well. The data structures and methods presented here are straightforward to implement and enable the efficient tracking of complex fracture and fragmentation processes. The efficiency and versatility of the approach is demonstrated with the aid of two examples of application to dynamic fracture[1].

3.1 Introduction

The essential interplay between geometry and mechanics comes into sharp focus in applications where the topology of the domain may change, oftentimes extensively, in the course of calculations. Fragmentation, which may result in a runaway proliferation of bodies in the form of fragments [65, 88, 194, 145], provides a case in point.

Camacho and Ortiz [30, 131] in two dimensions, and Pandolfi *et al.* [140, 168, 169] in three dimensions, have established the feasibility of: i) accounting explicitly for individ-

[1] **This chapter has been published in a peer reviewed journal paper in 2002**.
A. Pandolfi and M. Ortiz. An Efficient Adaptive Procedure for Three-Dimensional Fragmentation Simulations. *Engineering with Computers*, 18 (2), 148-159 (2002).

ual cracks as they nucleate, propagate, branch and possibly link up to form fragments; and ii) simulating explicitly the granular flow which ensues following widespread fragmentation. In this approach, cracks are allowed to form and propagate along element boundaries in accordance with a cohesive-law model [137, 198]. Clearly, it is incumbent upon the mesh to provide a rich enough set of possible fracture paths, an issue which may be addressed within the framework of adaptive meshing. In contrast to other approaches [137, 198] which require interfacial elements to be inserted at the outset along potential fracture paths, Camacho and Ortiz [30], and Pandolfi *et al.* [140, 168, 169], adaptively create new surface as required by the cohesive model by duplicating nodes along previously coherent element boundaries and inserting surface-like *cohesive elements* which encapsulate the fracture behavior of the solid. These elements are surface-like and are compatible with general bulk finite element discretizations of the solid, including those which account for plasticity and large deformations.

Pandolfi and Ortiz [141] have given an enumeration of the ways in which the topology and geometry of a three-dimensional finite-element model may evolve as a consequence of fracture and fragmentation, and have described the actions which may be taken in order to update the boundary representation, or *Brep*, of the solid. Maintaining an up-to-date Brep is of the essence when meshing methods such as the advancing front [144, 143, 98] are utilized [152]. The Brep may also assist in the implementation of contact algorithms [87]. The geometrical framework proposed by Pandolfi and Ortiz [141] has extensively utilized in a broad range of applications involving fracture and fragmentation [140, 168, 169].

The Brep of a solid can become inordinately complex, and thus computationally costly to maintain, in applications involving profuse fragmentation. In addition, some meshing algorithms, e. g., those based on subdivision [116], and contact algorithms (e. g., [139]) do not require a full Brep for their implementation. In these cases, much simpler data structures suffice in order to account for fragmentation processes.

The purpose of this article is to present one such set of data structures, and a suite of methods for constructing and updating the structures. The data structures and methods are straightforward to implement and enable the efficient tracking of complex fracture and fragmentation processes. We also present two examples of the application to dynamic fracture, which illustrate the ability of the method to represent intricate geometrical and topological transitions resulting from crack branching, the nucleation of surfaces and interior cracks, crack coalescence, the detachment of fragments, and other effects.

The organization of the paper is as follows. In Section 3.2 we introduce three simple data structures where all necessary information pertaining to tetrahedra, faces and edges is stored. In Section 3.3 we present the suite of methods for evolving the data structures in response to fragmentation. Finally, in Section 3.4 we present examples of application which demonstrate the scope and the versatility of the approach.

3.2 Topological Data Structures for a 3D finite element model

We shall restrict our attention to tetrahedral triangulations and regard the computational model as a three-dimension simplicial complex [156, 104, 80]. In addition, we focus on the case of quadratic interpolation and, hence, every tetrahedron in the triangulation gives rise to a ten-node tetrahedral finite-element (e. g., [152]). Extensions to higher-order elements are straightforward but will not be pursued here. The local nodal numbering convention for the tetrahedral elements adopted here is shown in Fig. 3.1a. Each tetrahedron is bounded by exactly four triangular faces, Fig. 3.1b, and six edges, Fig. 3.1c. The faces and the edges can be oriented consistently by an appropriate ordering of the nodes, Figs. 3.1b and Fig. 3.1c. A face is bounded by exactly three edges. Each face is incident on exactly one tetrahedron, if the face is on the boundary of the body, or two tetrahedra, if the face is in the interior. Edges are incident on rings of varying numbers of tetrahedra. Likewise, a variable number of faces may be adjacent to an edge.

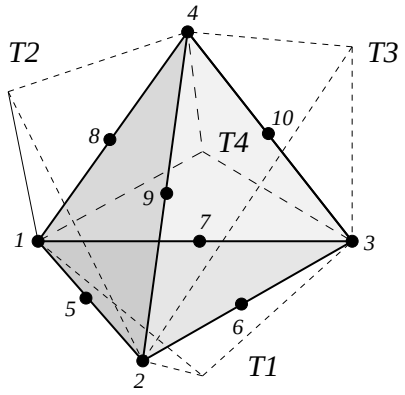

(a)

Figure 3.2: Tetrahedron connected to four adjacent tetrahedra.

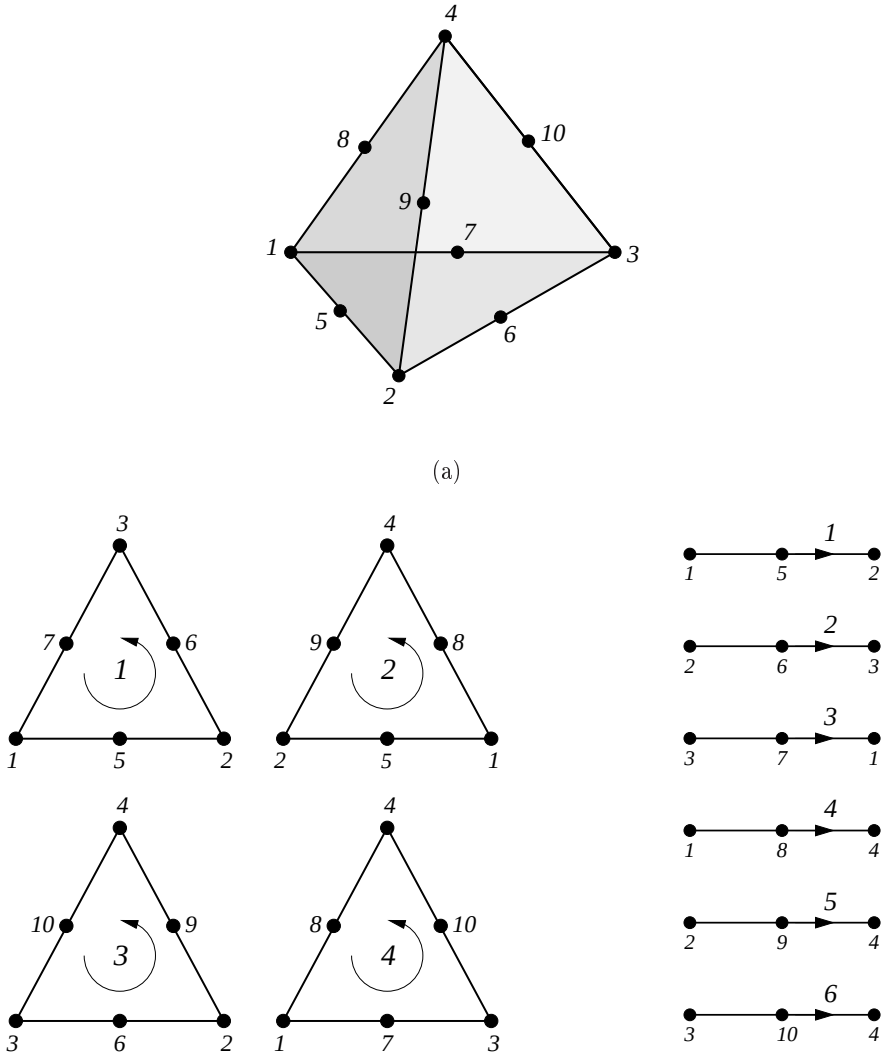

Figure 3.1: (a) A 10-nodes `tetrahedron`; (b) description of its four `facets`; (c) description of its six segments.

We begin by introducing three data structures which collect these data and relationships, namely, the `tetrahedra`, `facets` and `segments` structures. In describing these structures, we adopt C syntax for definiteness. The redundancy of data stored in our structures is justified by the need to speed up some additional searching procedure used in the mechanical applications.

The data stored in the `tetrahedra` structure consists of the number of the element, the element connectivity, pointers to its six `segments`, pointers to its four `facets`, and pointers to the four adjacent `tetrahedra`, Figs. 3.2- 3.3. Some of these pointers can be null. For instance, if a tetrahedron is incident on the boundary one or more of the pointers to adjacent tetrahedra are null. With a view to facilitating fragmentation simulations based on the use of cohesive elements [141], we include in the `tetrahedra` structure the number of the adjacent cohesive elements and the side of the cohesive elements incident on the tetrahedron.

```
/*-------------------------------------------------------------*
 * Tetrahedron data structure                                  *
 *-------------------------------------------------------------*/
typedef struct tetra
{
  struct tetra   *Link, *Rink;  /* Links */
  int             el;           /* Element no. */
  int             N[10];        /* Nodes */
  struct segment *S[6];         /* Pointers to Segments */
  struct facet   *F[4];         /* Pointers to Facets */
  struct tetra   *T[4];         /* Pointers to Tets */
  int             C[4];         /* Cohesive element */
  int             L[4];         /* Coh. el. side: 0=bottom, 1=top */
} Tetra;
```

Figure 3.3: Description of the `tetrahedron` data structure.

The data stored in the `facet` structure consists of an array containing six nodal numbers, ordered cyclically so as define an orientation for the face; pointers to the top and bottom tetrahedra, defined in accordance with the orientation of the face, Fig. 3.4a; pointers to the three edges incident on the face; and a boolean variable indicative of whether the face is interior or exterior, Fig. 3.5. Specifically, the identify top (bottom) or positive (negative) `tetrahedron` is that tetrahedron from which the nodes of the `facet` appear to be traversed counterclockwise (clockwise). For `facets` which are on the surface, the bottom `tetrahedron` is null. With a view to fragmentation applica-

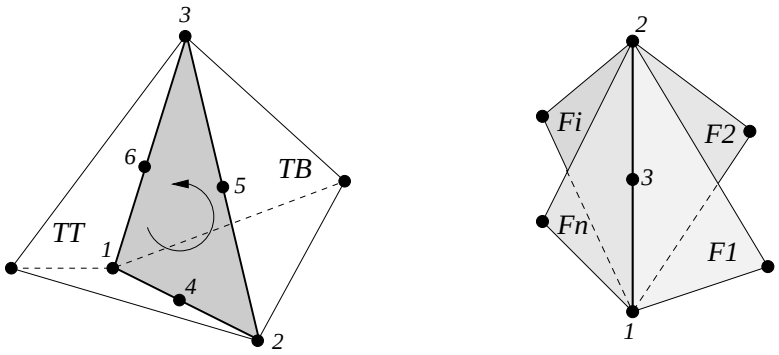

Figure 3.4: (a) A `facet` connected to two `tetrahedra`; (b) a `segment` connected to several `facets`.

tions, we additional collect the components of the unit normal; the critical traction for the insertion of a cohesive element, and an index designating the cohesive law to be used within the cohesive element.

```
/*-----------------------------------------------------------------*
 * Facet data structure                                            *
 *-----------------------------------------------------------------*/
typedef struct facet
{
  struct facet   *Link, *Rink;  /* Links */
  int             N[6];         /* Nodes */
  struct tetra   *T[2];         /* Pointers to Tets */
  struct segment *S[3];         /* Pointers to Segments */
  int             posi;         /* 0 = internal, 1 = external */
  double          v[3];         /* Components of the unit normal */
  double          sc;           /* Traction limit value */
  int             cm;           /* Cohesive material index */
} Facet;
```

Figure 3.5: Description of the `facet` data structure.

The edge structure `segment` contains an array with the numbers of its three nodes, Fig. 3.6, all of which are shared with one or more adjacent `facets` and with one or more adjacent `tetrahedra`. The local sequential numbering of the nodes defines

the orientation of the edge. Owing to the variable environment of the edges in the triangulation, the structure `segments` additionally contains arrays of pointers which need to be allocated dynamically. These are the array of pointers to the tetrahedra and faces adjacent to the edge. The dimension of these arrays is also stored in the structure, as well as an additional boolean variable which designates the edge as interior or exterior.

```
/*-------------------------------------------------------------*
 * Segment data structure                                      *
 *-------------------------------------------------------------*/
typedef struct segment
{
  struct segment *Link, *Rink;  /* Links */
  int             N[3];         /* Nodes */
  int             nt;           /* No. adj tets */
  struct tetra  **T;            /* Pointers to the first Tet */
  int             nf;           /* No. adj Facets */
  struct facet  **F;            /* Pointer to the first Facet */
  int             posi;         /* 0 = internal, 1 = external */
} Segment;
```

Figure 3.6: Description of the `segment` data structure.

A C procedure for setting up the structures just described from a conventional finite-element connectivity array is shown in Appendix A.

3.3 Fragmentation

Ortiz and Pandolfi [133] developed a class of three-dimensional cohesive elements consisting of two six-node triangular facets (Fig. 3.7a). The opening displacements are described by quadratic interpolation within the element. The element is fully compatible with –and may be used to bridge– pairs of ten-node tetrahedral elements (Fig. 3.7b). The elements are endowed with full finite-deformation kinematics and, in particular, are exactly invariant with respect to superposed rigid body translations and rotations.

We are here specially concerned with dynamic fragmentation, although static applications may be treated similarly. The analysis proceeds incrementally in time, e. g., by explicit dynamics. Following Camacho and Ortiz [30], cohesive elements are introduced adaptively at element interfaces as required by a fracture –or spall– criterion. For in-

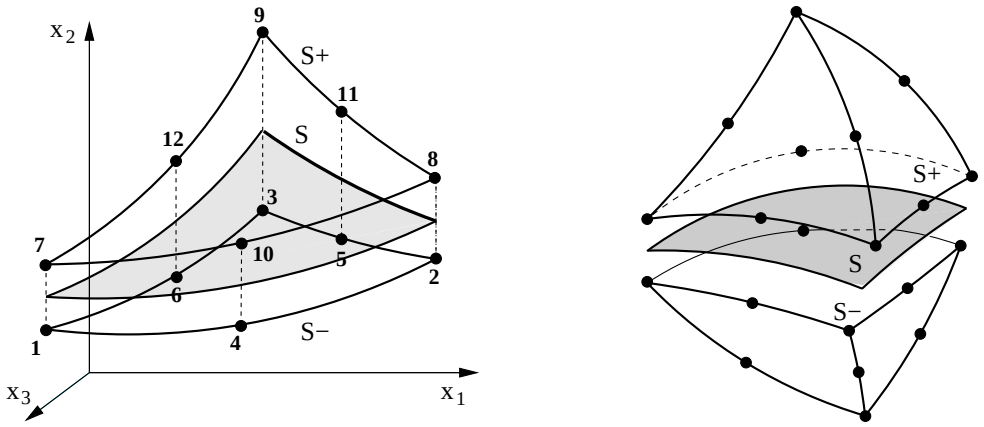

(a) (b)

Figure 3.7: (a) Geometry and connectivities of 12-nodes cohesive element; (b) Assembly of 12-node triangular cohesive element and two 10-node tetrahedral elements.

stance, fracture may be supposed to initiate at a previously coherent element interface when a suitably defined *effective traction* attains a critical value [30, 51, 133]. When the fracture criterion is met at an element interface, a cohesive element is inserted, leading to the creation of new surface. In this manner, the shape and location of successive crack fronts is itself an outcome of the calculations.

Next we discuss how the data structures defined in the preceding section may be used to support fragmentation simulations of the type just described. In particular, we specifically address the issue of how to update the data structures in response to fragmentation. The update procedure consists of two basic operations:

1. Selection of interior faces (`facets`) for the insertion of new cohesive elements.
2. Updating the data structures based on the selected `facets`.

We proceed to discuss these two steps in turn.

3.3.1 Selection of faces to be fractured

The selection of an interior face for the insertion of a cohesive element is based on the attainment of a suitable fracture criterion. The specific form of this criterion depends on the type of cohesive model used in calculations. For definiteness, we consider the

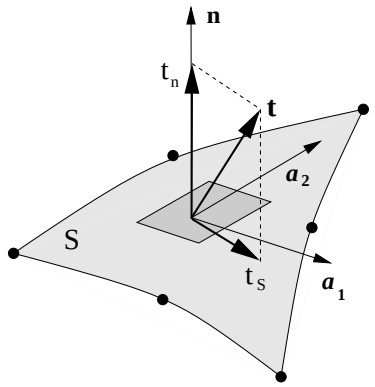

Figure 3.8: Normal and tangential components of the traction acting on an interface.

class of cohesive laws proposed by [30, 51, 133], which are based on the introduction of an effective opening displacement and the corresponding work-conjugate effective traction:

$$t_{eff} = \sqrt{t_n^2 + \beta^{-2}|\boldsymbol{t}_s|^2} \tag{3.1}$$

where β is a tension-shear coupling parameter, t_n denotes the traction component normal to the `facet`, and $\boldsymbol{t}_s$ is the corresponding tangential traction, Fig. 3.8. If, in addition, cohesive surfaces are assumed to be rigid, or perfectly coherent, below a certain critical traction σ_c, or spall strength, then the appropriate form of the fracture criterion is:

$$t_{eff} \geq \sigma_c \tag{3.2}$$

This condition is checked for each internal face (for example, at the integration points) at the conclusion of a pre-specified number of time steps in the calculations, and the faces where the criterion is met are flagged for subsequent processing. Evidently, criterion (3.2), which arises directly from the mechanics of cohesive fracture, drives the evolution of the geometrical description of the model. This connection exemplifies the tight coupling between mechanics and geometry which is characteristic of fragmentation simulations.

3.3.2 Data-structure update

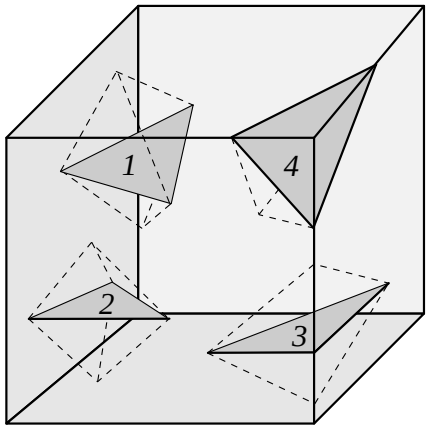

Figure 3.9: Classification of cases according to whether the fractured `facet` has zero (case 1), one (case 2), two (case 3) or three (case 4) `segments` on the boundary.

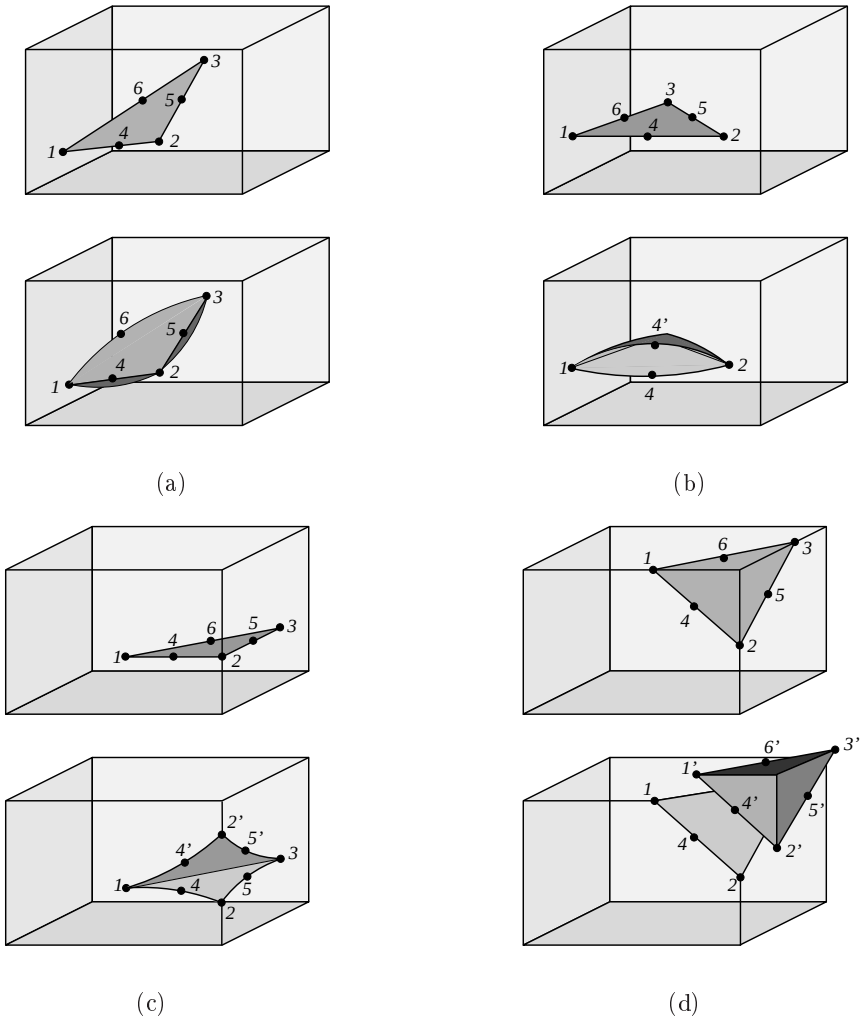

Figure 3.10: Topological changes induced by the fracturing of a `facet`. The primed numbers indicate the new inserted nodes. (a) Case 1: no `segments` on the boundary. No action; (b) Case 2: one `segment` on the boundary. The mid-side node is duplicated. (c) Case 3: two `segments` on the boundary. The corner node is duplicated and the mid-side nodes are duplicated; (d) Case 4: three `segments` on the boundary. All six nodes are duplicated.

The operations to perform in order to process a fractured face depend critically on its position with respect to the external boundaries of the domain. Four main cases may be identified depending on whether the fractured `facet` has zero, one, two or three `segments` resting on the boundary, Fig. 3.9. This information is supplied by the flag *posi* of each `segment` contained in the `facet`. In all cases the fractured `facet` is

duplicated and a new `facet` is added to the corresponding linked list. The remaining operations to be performed are:

1. No `segments` are on the boundary: No further operations, Fig. 3.10a.
2. One `segment` is on the boundary: the `segment` is duplicated by doubling the mid-side node, Fig. 3.10b.
3. Two `segments` are on the boundary: the `segments` are duplicated by doubling the mid-side nodes; the corner node is duplicated when it represents the sole remaining connection between the top and bottom `tetrahedra`, Fig. 3.10c.
4. Three `segments` are on the boundary: the `segments` are duplicated by doubling the mid-side nodes; a corner node is duplicated when it represents the sole remaining connection between the top and bottom `tetrahedra`, Fig. 3.10d. The new node is added to the top elements of the fractured `facet`.

The commented C code reported in Appendix B gives a detailed account of the operations to be performed in order to update the data structures and the connectivities.

3.4 Examples of application

In this section we demonstrate the scope and versatility of the procedures described above with the aid of two examples of application. The fracture criterion (3.2) is adopted in order to determine the onset of fracture in a `facet` [30, 51, 133]. In all calculations, the material is modeled as nonlinear elastic obeying a Neohookean constitutive law [106]. In particular, full finite kinematics is taken into account.

The first application concerns the simulation of the dynamic fragmentation of a three-point bend PMMA specimen with a sharp precrack contained within its symmetry plane. The central point of the top side of the specimen is suddenly imparted a uniform velocity 40 m/s at time $t = 0$, and the velocity is held constant thereafter. The length of the specimen is 8.4 mm, its width 1 mm and its height 1.4 mm (Fig. 3.11).
The model is meshed into 4,260 ten-node tetrahedra and 6,420 nodes. The mesh is finer in the central part and is gradually coarsened away from the crack (Fig. 3.12a).

The material parameters employed in the calculations are: specific fracture energy per unit area, or critical energy release rate, $G_c = 210$ N/m; critical cohesive stress, or spall strength, $\sigma_c = 100$ MPa; tension-coupling constant $\beta = 1$; Young's modulus $E = 3$ GPa; Poisson's ratio $\nu = 0.38$; and mass density $\rho = 1180$ kg/m^3. The equations

of motion are integrated in time by recourse to Newmark's explicit algorithm with parameters $\beta = 0$, $\gamma = 1/2$ [18, 82]. The time step used in the calculations is $\triangle t = 1.7$ x $10^{-4}\mu$s.

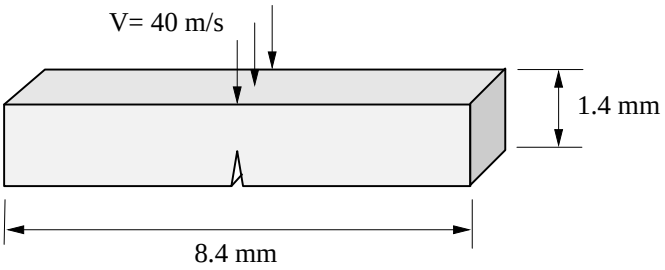

Figure 3.11: Three point bend test in PMMA specimen, loading conditions. The impact is simulated imposing a uniform and constant velocity V along the central line. Owing to the high impact speed, the supports are not simulated.

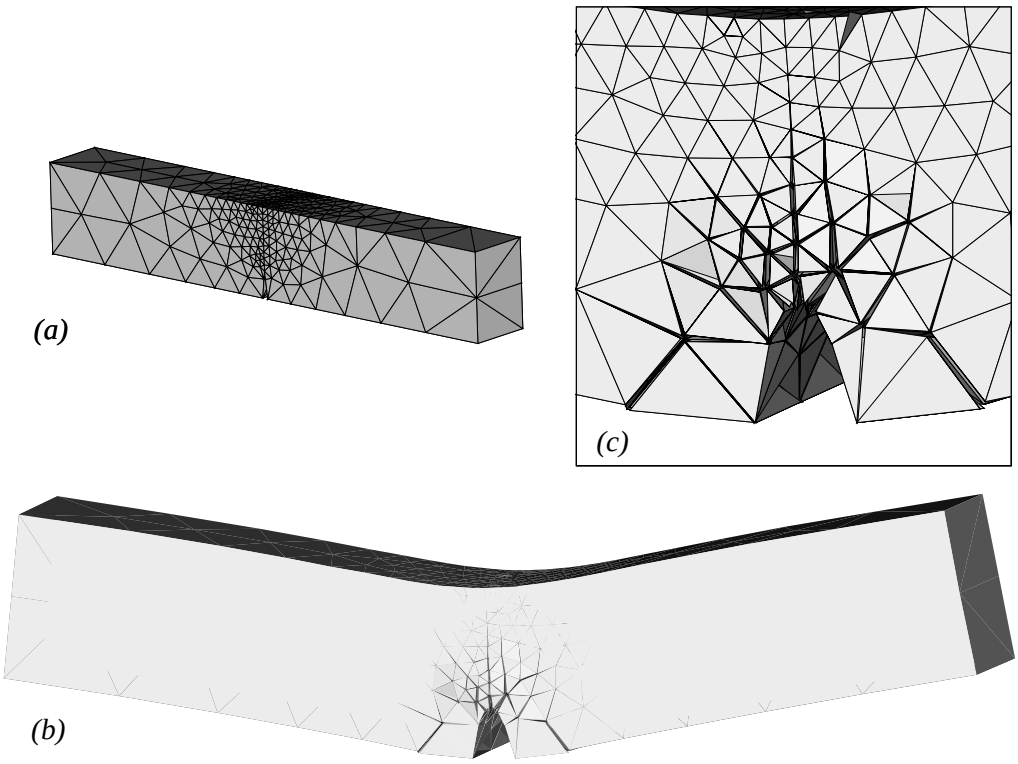

Figure 3.12: Fragmentation algorithm applied to the three-point bend dynamic test in PMMA: (a) initial mesh; (b) final configuration; (c) detail of the fracture and fragmentation pattern in the final configuration.

Figs. 3.12b and c show the computed fracture and fragmentation pattern after 20 μs. The ability of the approach to track the evolution of complex crack geometries is clearly demonstrated. As may be seen in the figure, the geometrical update procedure effectively deals with the intricate geometrical and topological transitions which result from crack branching, the nucleation of surfaces and interior cracks, crack coalescence, the detachment of fragments, and others.

The second example of application concerns the simulation of dynamic crack branching in a PMMA thin square plate. The plate is 3 mm in length and 0.3 mm in thickness. The specimen contains an initial 0.25 mm sharp notch. Constant normal velocities, tending to open the crack symmetrically in mode I, are prescribed on the top and bottom edges of the specimen. The magnitude of the prescribed velocities corresponds to a nominal strain rate of $0.002/\mu$s. In addition, the initial velocity field is assumed to be linear in the coordinate normal to the crack and to correspond to a uniform rate of

deformation of $0.002/\mu$s throughout the specimen, Fig. 3.13.

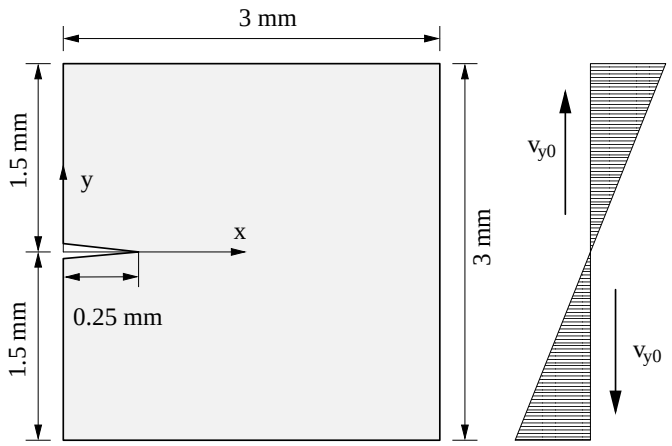

Figure 3.13: Geometry of the PMMA square plate and mode-I loading conditions.

The model is meshed into 14,319 ten-node tetrahedra and 25,936 nodes, Fig. 3.14a. The equations of motion are integrated using Newmark's explicit algorithm with time step $\triangle t = 6$ x $10^{-5}\mu$s. The material parameters used in the calculation are: specific fracture energy per unit area $G_c = 176.15$ N/m; critical cohesive stress $\sigma_c = 324$ MPa; tension-shear coupling constant $\beta = 2$; Young's modulus $E = 3.29$ GPa; Poisson's ratio $\nu = 0.35$; and mass density $\rho = 1190$ kg/m^3. Figs. 3.14b and c show the fracture pattern at the conclusion of the test. As may be seen, at a low prescribed strain rate the crack tends to grow within its plane, and it branches only when it senses the proximity of the free surface on the right side of the specimen. Results from a similar calculation at a higher nominal strain rate of $0.01/\mu$s are shown in Figs. 3.15a-c. The mesh in this case contains 6,363 ten-node tetrahedra and 11,569 nodes, and the stable time step is $\triangle t = 6$ x $10^{-5}\mu$s. Figs. 3.15b and c show the crack patterns at the conclusion of the test. Initially the crack remains within its plane and accelerates steadily. As a certain crack speed is attained, the crack begins to issue lateral branches. These branches consume additional fracture energy, thereby limiting the mean crack speed. As the crack approaches the free surface, the extent of branching increases steadily.

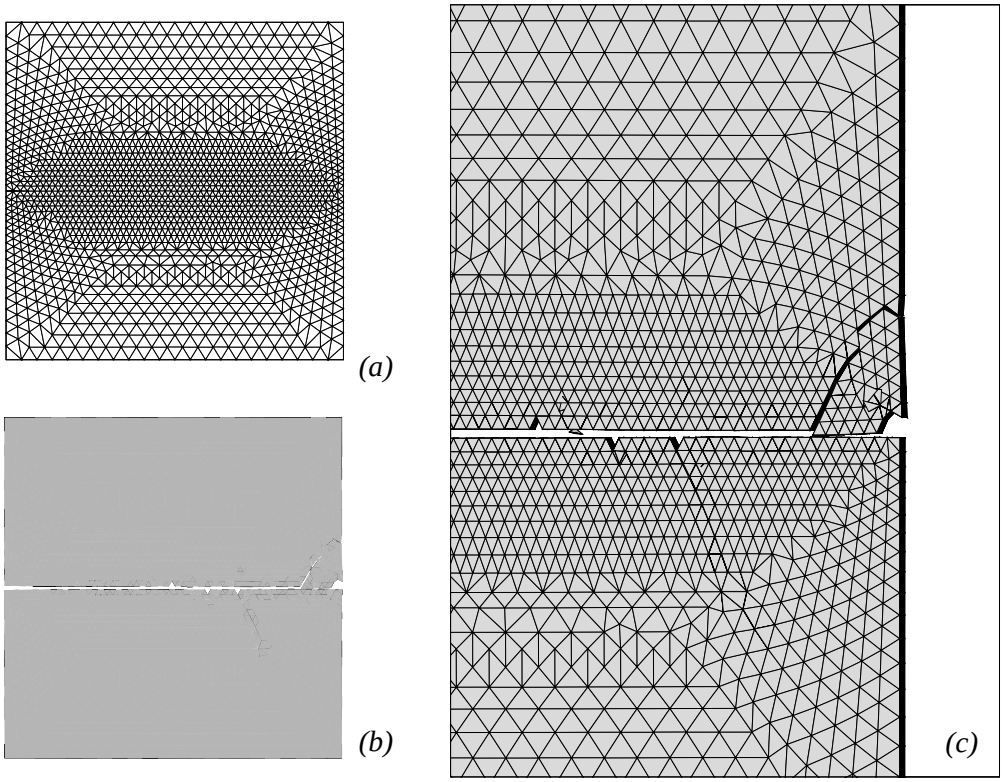

Figure 3.14: Mode-I dynamic fracture test in PMMA at nominal strain rate $0.002/\mu$s. (a) Initial mesh and prescribed and initial velocities; (b) final configuration; (c) detail of the branching in the final configuration at time 5 μs.

As in the previous example, the ability of the method to deal with complex geometrical and topological transitions simply and effectively is remarkable. In particular, cracks are allowed to branch unimpeded, connect with free surfaces or with other cracks to form fragments.

We conclude this section by emphasizing that the simulations presented above, while representative of a broad class of engineering materials and loading conditions, are not intended as a validation of the cohesive model but as a demonstration of the computational methodology. Detailed validation studies, including extensive comparisons with experiment, based on test configurations similar to those just described may be found elsewhere [140, 168, 169, 206].

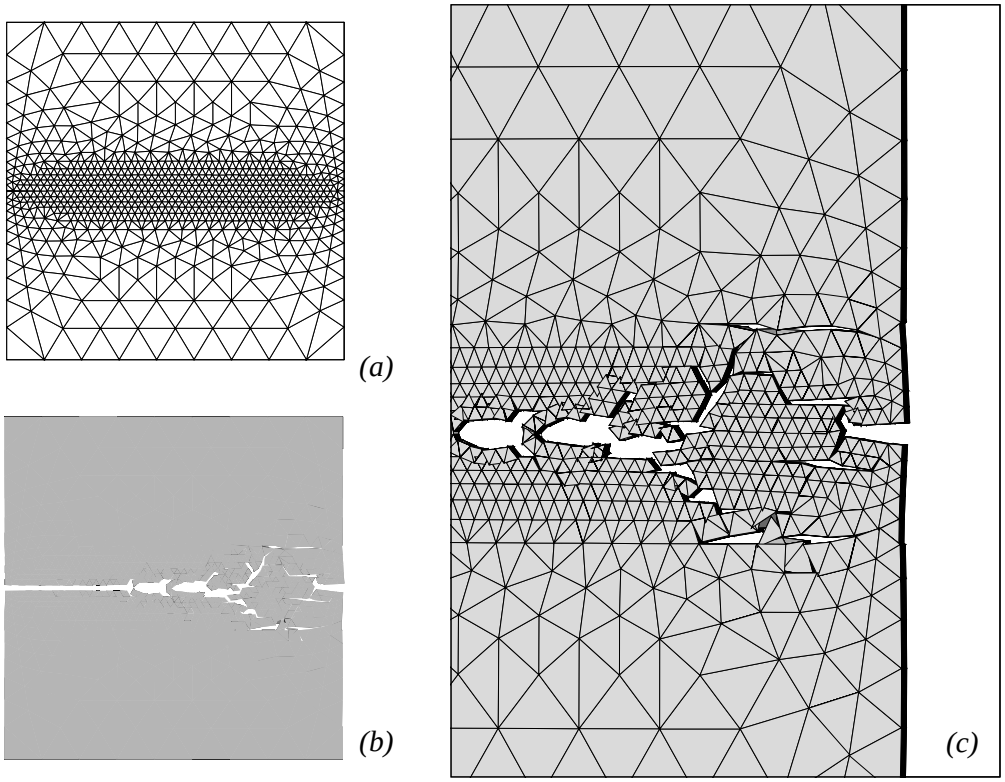

Figure 3.15: Mode-I dynamic fracture test in PMMA at a nominal strain rate $0.01/\mu$s. (a) Initial mesh; (b) final configuration; (c) detail of the branching in the final configuration at time 5 μs.

3.5 Summary and Conclusions

In cohesive theories of fracture, material separation is governed by a suitable cohesive law. In finite-element simulations based on a tetrahedral triangulation of the domain of analysis, decohesion and opening may conveniently be restricted to interior triangular faces. The cohesive laws considered here are rigid up to the attainment of the cohesive strength of the material. Consequently, initially all the faces in the triangulation are perfectly coherent, i. e., conforming in the usual finite element sense. Cohesive elements are inserted adaptively at interior faces when the effective traction acting on those face reaches the cohesive strength of the material. The insertion of cohesive elements changes the geometry of the boundary and, frequently, the topology of the model as well.

We have presented a simple set of data structures, and a collection of methods for constructing and updating the structures, designed to support the use of cohesive elements in simulations of fracture and fragmentation. The data structures and methods are straightforward to implement and enable the efficient tracking of complex fracture and fragmentation processes. The examples of application discussed here illustrate the uncanny ability of the method to represent intricate geometrical and topological transitions resulting from crack branching, the nucleation of surfaces and interior cracks, crack coalescence, the detachment of fragments, and others.

Acknowledgments

The support of the Army Research Office through grant DAA-H04-96-1-0056 is gratefully acknowledged. We are also grateful for support provided by the DoE through Caltech's ASCI/ASAP Center for the Simulation of the Dynamic Behavior of Solids. The assistance provided by Dr. Rena Chengxiang Yu with the numerical examples is gratefully acknowledged.

Appendix A

This procedure fills the data structures described in Figs. 3.3-3.6. As the connectivity table is traversed, each element is added to the linked list of `tetrahedra`. The corresponding six `segments` of each `tetrahedra` are identified, and the linked list of the `segments` and the list of incident `tetrahedra` of the `segments` are updated. Likewise, the four `facets` of each tetrahedra are identified, and the linked list of the `facets` and the list of incident `tetrahedra` of the `facets` are updated. The subroutines are listed in the following boxes: (1) a new `segment` or `facet` insertion follows from the failure of a search in the corresponding linked lists; (2) the insertion of a new `tetrahedron`; (3) check of the existence of a `segment` in the corresponding linked lists ; (4) the insertion of a new `segment`; (5) check of the existence of a `facet` in the corresponding linked lists; (6) the insertion of a new `facet` in the corresponding linked list; (7) update of the list of `facet` in the `segment` data structure.

```
int sc[6][4] = {{0,4,1},{1,5,2},{2,6,0},   /*  segments topology */
                {0,7,3},{1,8,3},{2,9,3}};
int fc[4][6] = {{0,1,2,4,5,6},{0,3,1,7,8,4}, /*  faces topology */
               {1,3,2,8,9,5},{0,2,3,6,9,7}};
int p1[3] = {1,2,0};
/*-------------------------------------------------------------*
 * void CreateDataStructures                                   *
 *-------------------------------------------------------------*/
void CreateDataStructures ()
{
  Segment  *S[6], *G;
  Facet    *F[4], *R;
  Tetra    *T,    *Ti;
  int       ie, ic, i, j, n[10];
  TetraList   = NULL;    /*  Initialize the Tetrahedra list  */
  SegmentList = NULL;    /*  Initialize the Segments list  */
  FacetList   = NULL;    /*  Initialize the Facets list  */
  for (ie = 0; ie < TetraElementNumber; ie++) {
                                  /*  Add Tetrahedron */
    for (j = 0; j < 10; j++) n[j] = connectivity[ie*nodes_element+j];
    TetraList = T = AddTetra (TetraList, n[0], n[1], n[2], n[3], n[4],
                              n[5], n[6], n[7], n[8], n[9], ie);
    for (ic = 0; ic < 6; ic++) {  /*  Add Segments */
      S[ic] = SearchInSegments (T, n[sc[ic][0]], n[sc[ic][1]],
                                  n[sc[ic][2]]);
      TetraList->S[ic] = S[ic];
    }
    for (ic = 0; ic < 4; ic++) {  /*  Add Facets */
      F[ic] = SearchInFacets (T, n[fc[ic][0]], n[fc[ic][1]],
                                n[fc[ic][2]], n[fc[ic][3]],
                                n[fc[ic][4]], n[fc[ic][5]]);
      for (j = 0; j < 3; j++) {   /*  Check Segments and Facets */
         for (i = 0; i < 6; i++) {
            if ((S[i]->N[0] == F[ic]->N[j] &&
                 S[i]->N[2] == F[ic]->N[p1[j]]) ||
                (S[i]->N[2] == F[ic]->N[j] &&
                 S[i]->N[0] == F[ic]->N[p1[j]])) {
            F[ic]->S[j] = S[i];
            SegmentFacet (S[i], F[ic]);
          }
        }
      }
      /*  update the incident Facet */
      TetraList->F[ic] = F[ic];
    }
  }
```

1.

```
/*  Complete the Tet list with adj Tets */
  for (T = TetraList; T != NULL; T = T->Rink) {
    for (i = 0; i < 4; i++) {
      R = T->F[i];
      if (R->T[0] == T) T->T[i] = R->T[1];
      if (R->T[1] == T) T->T[i] = R->T[0];
    }
  }
/*  Complete the Facets list defining if inside or outside */
  for (R = FacetList; R != NULL; R = R->Rink) {
    if (R->T[0] == NULL) R->posi = 1;
    if (R->T[1] == NULL) R->posi = 1;
  }
/*  Complete the Segment list defining if inside or outside */
  for (G = SegmentList; G != NULL; G = G->Rink) {
    for (i = 0; i < G->nf; i++) {
      if (G->F[i]->posi == 1) G->posi = 1;
    }
  }
  return;
}
```

2.

```
/*-------------------------------------------------------------*
 * Tetra *AddTetra                                             *
 *-------------------------------------------------------------*/
Tetra *AddTetra (Tetra *beg, int n1, int n2, int n3, int n4, int n5,
             int n6, int n7, int n8, int n9, int n10, int ie)
{
  Tetra *T;      /*  Add a Tet to the linked list */
  T       = calloc (1, sizeof(Tetra));
  T->el   = ie + 1;
  T->N[0] = n1;  T->N[1] = n2;
  T->N[2] = n3;  T->N[3] = n4;
  T->N[4] = n5;  T->N[5] = n6;
  T->N[6] = n7;  T->N[7] = n8;
  T->N[8] = n9;  T->N[9] = n10;
  T->C[0] = 0;   T->C[1] = 0;  T->C[2] = 0;   T->C[3] = 0;
  T->Link = NULL;
  T->Rink = beg;
  if (beg != NULL) beg->Link = T;
  return T;
}
```

3.
```
/*-------------------------------------------------------------*
 * Segment *SearchInSegments                                   *
 *-------------------------------------------------------------*/
Segment *SearchInSegment (Tetra *T, int n1, int n2, int n3)
{
  Segment  *S;    /*  Search for a Segment in SegmentList */
  int       nt;
  for (S = SegmentList; S != NULL; S = S->Rink) {
    if ((n1 == S->N[0] && n3 == S->N[2]) ||
        (n1 == S->N[2] && n3 == S->N[0])) {
      nt = S->nt;
      nt++;
      S->T = realloc (S->T, nt * sizeof(Tetra *));
      S->T[nt - 1] = T;
      S->nt = nt;
      return S;
    }
  }
  SegmentList = S = AddSegment (SegmentList, n1, n2, n3, T);
  return S;
}
```

4.
```
/*-------------------------------------------------------------*
 * Segment *AddSegment                                         *
 *-------------------------------------------------------------*/
Segment *AddSegment (Segment *beg, int n1, int n2, int n3, Tetra *T)
{
  Segment *S;     /*  Add a Segment to the linked list */
  S       = calloc (1, sizeof(Segment));
  S->posi = 0;
  S->N[0] = n1;  S->N[1] = n2;  S->N[2] = n3;
  S->nt   = 1;
  S->T    = calloc (1, sizeof(Tetra *));
  S->T[0] = T;
  S->nf   = 0;
  S->F    = calloc (1, sizeof(Facet *));
  S->Rink = beg;
  S->Link = NULL;
  if (beg != NULL) beg->Link = S;
  return S;
}
```

5.
```
/*-------------------------------------------------------------*
 * Segment *SearchInFacets                                     *
 *-------------------------------------------------------------*/
Facet *SearchInFacets (Tetra *T, int n1, int n2, int n3,
                       int n4, int n5, int n6)
{
  Facet *F;      /*  Search for a Facet in the FacetList */
  for (F = FacetList; F != NULL; F = F->Rink) {
    if ((n1 == F->N[0] || n1 == F->N[1] || n1 == F->N[2]) &&
        (n2 == F->N[0] || n2 == F->N[1] || n2 == F->N[2]) &&
        (n3 == F->N[0] || n3 == F->N[1] || n3 == F->N[2])) {
      F->T[1] = T;
      return F;
    }
  }
  FacetList = F = AddFacet (FacetList, n1, n2, n3, n4, n5, n6, T);
  return F;
}
```

6.
```
/*-------------------------------------------------------------*
 * Facet *AddFacet                                             *
 *-------------------------------------------------------------*/
Facet *AddFacet (Facet *beg, int n1, int n2, int n3,
                 int n4, int n5, int n6, Tetra *T)
{
  Facet *F;     /*  Add a Facet to the linked list */
  F       = calloc (1, sizeof(Facet));
  F->posi = 0;
  F->N[0] = n1;  F->N[1] = n2;  F->N[2] = n3;
  F->N[3] = n4;  F->N[4] = n5;  F->N[5] = n6;
  F->T[0] = T;
  F->Rink = beg;
  F->Link = NULL;
  if (beg != NULL) beg->Link = F;
  return F;
}
```

```
/*----------------------------------------------------------------*
 * void *SegmentFacet                                             *
 *----------------------------------------------------------------*/
void SegmentFacet (Segment *S, Facet *F)
{
  int nf = S->nf;
  int j;
  for (j = 0; j < nf; j++) if (S->F[j] == F) return;
  AddFaceToSegment (S, F);
  return;
}
/*----------------------------------------------------------------*
 * void *AddFaceToSegment                                         *
 *----------------------------------------------------------------*/
void AddFaceToSegment (Segment *S, Facet *F)
{
  int nf = S->nf;
  nf++;
  S->F  = realloc (S->F, nf*sizeof(Facet));
  S->F[nf - 1] = F;
  S->nf = nf;
  return;
}
```

7.

Appendix B

Code for the insertion of a new surface into a 3D mesh: (1) driver; (2) insertion of a new `facet` into the data structures; (3) changes in the data structures required by the duplication of a mid node; (Appendix A, 4) a new `segment` is added; (4) the list of the `tetrahedra` incident to the original `segment` is traversed and the `tetrahedra` are moved from the old to the new `segment`; (5) the list of the `facets` incident to the original `segment` is traversed and the `facets` are moved from the old to the new `segment`; (6) update of the cohesive element connectivity; (7) recursive subroutine to check the existence of additional connections between the Top and the Bottom `tetrahedron` before duplicating a corner node; (8) recursive subroutine to perform changes in the data structures required by the duplication of a corner node (the `tetrahedron` connectivity is update, and the incident `segments` and `facets` are updated; thus the adjacent `tetrahedra` are checked); (9) reallocation of the nodal vectors, (10) reallocation of element vectors. The last two subroutines must be completed with the reallocation of all the nodal and elemental vectors defined in the code.

```
/*-------------------------------------------------------------*
 * void CreateSurface                                          *
 *-------------------------------------------------------------*/
void CreateSurface (int cohmate, Facet *facet)
{
  Tetra   *TEB, *TET;   /*  Top and Bottom tetrahedra */
  int      open[3];     /*  Boundary sides counters */
  Segment *S[3];        /*  Facet Segments */
  Facet   *facetnew;    /*  New Facet */
  int      i, j;
                        /* Get the six nodes on the Facet */
  for (i = 0; i < 6; i++) node[i] = nold[i] = facet->N[i];
  TET  = facet->T[0];
  TEB  = facet->T[1];
  for (i = 0; i < 3; i++) {
    S[i] = facet->S[i];
    open[i] = S[i]->posi;
  }                                /* add a new facet */
  FacetList = facetnew = AddFacet (FacetList, node[0], node[2], node[1],
                                   node[5], node[4], node[3], TET);
  UpdateNewFacet (facet, facetnew, TEB, TET, cohmate);
  for (i = 0; i < 3; i++) {      /*  Check the midside node */
    if (open[i] == 0) continue;
    nodes++;
    node[i + 3] = nodes;
    UpdateMidNodes (TET, S[i], node[i + 3], cohmate);
    DefineNodeVectors (node[i + 3], nold[i + 3]);
  }                                /*  Check the corner node */
  counted = calloc (elements + 1, sizeof(int));
  for (i = 0; i < 3; i++) {
    if (open[i] == 0 || open[perm[i]] == 0) continue;
    for (j = 1; j <= TetraElementNumber; j++) counted[j] = 0;
    if (CornerToOpen (TET, TEB, nold[i]) == 0) continue;
    nodes++;
    node[i] = nodes;
    UpdateCornerNodes (TET, node[i], nold[i], cohmate);
    DefineNodeVectors (node[i], nold[i]);
  }
  free (counted);
  if (cohmate > 0) AddCohesive (cohmate, trli);
  return;
}
```

1.

```
/*-------------------------------------------------------------*
 * void UpdateNewFacet                                         *
 *-------------------------------------------------------------*/
void UpdateNewFacet (Facet *facet, Facet *facetnew,
                     Tetra *TEB, Tetra *TET, int cohmate)
{
  Segment *S[3];
  int      move[3] = {2,1,0};
  int      i;
/*  Update the old Facet */
  facet->T[1] = NULL;
  facet->posi = 1;
/*  Update the new Facet */
  facetnew->posi = 1;
/*  Add Segments to new Facet and new Facet to Segments */
  for (i = 0; i < 3; i++) {
    S[i] = facet->S[i];
    S[i]->posi = 1;
    facetnew->S[move[i]] = S[i];
    S[i] = AddFaceToSegment (S[i], facetnew);
  }
/*  Update the Facet and adjacency of the Tets */
  for (i = 0; i < 4; i++) {
    if (TEB->F[i] == facet) {
      TEB->T[i] = NULL;
      if (cohmate > 0) {
        TEB->C[i] = elements + 1;
        TEB->L[i] = 0;
      }
    }
    if (TET->F[i] == facet) {
      TET->F[i] = facetnew;
      TET->T[i] = NULL;
      if (cohmate > 0) {
        TET->C[i] = elements + 1;
        TET->L[i] = 1;
      }
    }
  }
  return;
}
```

2.

```
/*-------------------------------------------------------------*
 * void UpdateMidNodes                                         *
 *-------------------------------------------------------------*/
void UpdateMidNodes (Tetra *TET, Segment *SO, int nn, int cohmate)
{
  Segment *SN;
  Tetra   *T;
  int      n1 = SO->N[0];
  int      n2 = SO->N[2];
  int      ot = SO->nt;
  int      of = SO->nf;

/*  Insert a new Segment */
  SegmentList = SN = AddSegment (SegmentList, n1, nn, n2, TET);
  SN->posi = 1;
  SN->nt   = 0;

/*  Transfer Tets from the old to the new Segment */
  SN->T = realloc (SN->T, ot*sizeof(Tetra));
  TetraInSegments (TET, SO, SN, cohmate);
  SN->T = realloc (SN->T, SN->nt*sizeof(Tetra));
  SO->T = realloc (SO->T, SO->nt*sizeof(Tetra));

/*  Transfer Facets between the two Segments */
  SN->F = realloc (SN->F, of*sizeof(Facet));
  FacetInSegments (SO, SN);
  SN->F = realloc (SN->F, SN->nf*sizeof(Facet));
  SO->F = realloc (SO->F, SO->nf*sizeof(Facet));
  return;
}
```

3.

```
/*-------------------------------------------------------------*
 * void TetraInSegments                                        *
 *-------------------------------------------------------------*/
void TetraInSegments (Tetra *TET, Segment *SO, Segment *SN, int cohmate)
{
  Tetra *T;
  int    el = (TET->el - 1)*nodes_element;
  int    no = SO->N[1];
  int    nn = SN->N[1];
  int    ot = SO->nt;
  int    nt = SN->nt;
  int    i, j;
  for (i = 4; i < 10; i++) { /*  Change the connectivity */
    if (TET->N[i] != no) continue;
    TET->N[i] = connectivity[el + i] = nn;
    if (cohmate > 0) UpdateCohesive (TET, nn, no, 3);
  }
  for (j = 0; j < 6; j++) {  /*  Change the Segment in the Tet */
    if (TET->S[j] != SO) continue;
    TET->S[j] = SN;
  }
4.  for (i = 0; i < ot; i++) { /*  Move Tet from old to new Segment */
    T = SO->T[i];
    if (T != TET) continue;
    SN->T[nt] = T;
    nt++;
    SO->T[i] = NULL;
    break;
  }
  SN->nt = nt;
  for (j = i + 1; j < ot; j++, i++) SO->T[i] = SO->T[j];
  ot--;
  SO->nt = ot;
  for (i = 0; i < ot; i++) { /*  Look at adjacent Tets */
    T = SO->T[i];
    for (j = 0; j < 4; j++) {
      if (T->T[j] != TET) continue;
      TetraInSegments (T, SO, SN, cohmate);
      return;
    }
  }
  return;
}
```

```
/*-------------------------------------------------------------*
 * void FacetInSegments                                        *
 *-------------------------------------------------------------*/
void FacetInSegments (Segment *SO, Segment *SN)
{
  Tetra *T;
  Facet *F;
  int    nn = SN->N[1];
  int    of = 0;
  int    nf = 0;
  int    i, j, k;
  for (i = 0; i < SN->nt; i++) { /*  Update connectivities */
    T = SN->T[i];
    for (j = 0; j < 4; j++) {
      F = T->F[j];
      for (k = 0; k < 3; k++) {
        if (F->S[k] != SO) continue;
        F->S[k]     = SN;
        F->N[3 + k] = nn;
        SN->F[nf]   = F;
        nf++;
        break;
      }
    }
  }
  SN->nf = nf;
  for (i = 0; i < SO->nt; i++) { /*  Update the incident Facets  */
    T = SO->T[i];
    for (j = 0; j < 4; j++) {
      F = T->F[j];
      for (k = 0; k < 3; k++) {
        if (F->S[k] != SO) continue;
        SO->F[of] = F;
        of++;
        break;
      }
    }
  }
  SO->nf = of;
  return;
}
```

6.
```
/*-------------------------------------------------------------*
 * void UpdateCohesive                                         *
 *-------------------------------------------------------------*/
void UpdateCohesive (Tetra *T, int nn, int no, int add)
{
  int ce, cc, i, j;
  for (i = 0; i < 4; i++) {
    ce = T->C[i] - 1;
    if (ce < 0 || ce == elements) continue;
    cc = ce*nodes_element + T->L[i]*6 + add;
    for (j = 0; j < 3; j++) {
      if (connectivity[cc + j] != no) continue;
      connectivity[cc + j] = nn;
    }
  }
  return;
}
```

7.
```
/*-------------------------------------------------------------*
 * void CornerToOpen                                           *
 *-------------------------------------------------------------*/
int CornerToOpen (Tetra *TET, Tetra *TEB, int no)
{
  Tetra *T;
  int    i, j, res;
  counted [TET->el] = 1;
  for (i = 0; i < 4; i++) {
    T = TET->T[i];
    if (T == NULL) continue;
    for (j = 0; j < 4; j++) {
      if (T->N[j] != no) continue;
      if (T == TEB) return 0;
      if (counted[T->el] > 0) continue;
      if (CornerToOpen (T, TEB, no) == 0) return 0;
    }
  }
  return 1;
}
```

```
/*-------------------------------------------------------------*
 * void UpdateCornerNodes                                      *
 *-------------------------------------------------------------*/
void UpdateCornerNodes (Tetra *TET, int nn, int no, int cohmate)
{
  Segment *S;
  Facet   *F;
  Tetra   *T;
  int      el = (TET->el - 1)*nodes_element;
  int      j, i;

  counted[TET->el] = 0;       /*  Flag the Tet as checked */

  for (j = 0; j < 4; j++) {   /*  Check Tet and connectivity */
    if (TET->N[j] != no) continue;
    TET->N[j] = nn;
    connectivity[el + j] = nn;
    if (cohmate > 0) UpdateCohesive (TET, nn, no, 0);
    break;
  }
  for (j = 0; j < 6; j++) {   /*  Update Segments */
     S = TET->S[j];
     if (S->N[0] == no) S->N[0] = nn;
     if (S->N[2] == no) S->N[2] = nn;
  }
  for (i = 0; i < 4; i++) {   /*  Update Facets */
    F = TET->F[i];
    if (F->N[0] == no) F->N[0] = nn;
    if (F->N[1] == no) F->N[1] = nn;
    if (F->N[2] == no) F->N[2] = nn;
  }
   for (i = 0; i < 4; i++) {  /*  Next adjacency */
    T = TET->T[i];
    if (T == NULL) continue;
    if (counted[T->el] == 0) continue;
    UpdateCornerNodes (T, nn, no, cohmate);
  }
  return;
}
```

9.
```
/*-------------------------------------------------------------*
 * void DefineNodeVectors                                      *
 *-------------------------------------------------------------*/
void DefineNodeVectors (int node, int nold)
{
  int nd = nodes*dof_node;
  int nn = (node - 1)*dof_node;
  int no = (nold - 1)*dof_node;
  int j;
  coordinates = realloc (coordinates, nd*REAL);
  for (j = 0; j < dof_node; j++) {
    coordinates[nn + j] = coordinates[no + j];
  }
  return;
}
```

10.
```
/*-------------------------------------------------------------*
 * void AddCohesive                                            *
 *-------------------------------------------------------------*/
void AddCohesive (int cohmate, double trli)
{
  int     k, i;
  k = nodes_element * elements;
  elements++;
  connectivity     = realloc (connectivity,     (k + 1)*sizeof(int));
  element_material = realloc (element_material, elements*sizeof(int));
  for (i = 0; i < 6; i++) {
    connectivity[k + i    ] = nold[i];
    connectivity[k + i + 6] = node[i];
  }
  element_material [elements - 1] = cohmate;
  return;
}
```

Chapter 4

Numerical Investigation of the Dynamic Behavior of Advanced Ceramics

Abstract

This paper studies the dynamic behavior of advanced ceramics by a finite element model. It implements the direct simulation of fracture and fragmentation together with a mixed-mode cohesive law to describe the fracture process. In particular, we simulate dynamic Brazilian tests performed with a Hopkinson bar, at strain rates ranging from 65 to 89 s^{-1}, on six different materials: three kinds of alumina with different average grain sizes and degrees of purity, a blend of alumina and zirconia, silicon carbide and boron carbide. The rate dependence of the results emerges explicitly from the calculations, thanks both to the inertia attendant to the fracture process, and to the time effect provided by the cohesive law. Indeed, the simulations give accurate values for the dynamic strength of the six ceramics under study. The simulations also predict the main features of the crack pattern[1].

4.1 Introduction

Advanced ceramics are widely used as ballistic armors due to their excellent stiffness to weight and resistance to weight ratios. Another appealing property of advanced ceramics is their capacity for dissipating energy by fracture and friction when they are comminuted by the impact of a projectile. Thus, the dynamic mechanical response of these materials is especially important to grant the required level of protection to an armor. This is why some of the scientific research in this field has focused on the

[1] **This paper has been published in a peer reviewed journal paper in 2004**.
Rena C. Yu, Gonzalo Ruiz, and Anna Pandolfi. Numerical Investigation of the Dynamic Behavior of Advanced Ceramics *Engineering Fracture Mechanics*, 71 (4-6), 897-911 (2004).

determination of their dynamic properties and the development of accurate constitutive models and failure criteria at high strain rates.

As with other quasi-brittle materials, advanced ceramics perform very well under compression, but their tensile strength is low, approximately one order of magnitude below the compressive strength. Hence most times failure takes place when the tensile strength is reached, rendering it an essential property in the modelization of these materials. Several different tests have been proposed to measure the tensile strength of ceramics and it has been found that it grows with the strain rate under every experimental configuration. In particular, the diametral compression test or Brazilian test performed by means of a Hopkinson bar is seen by some experimentalists as a convenient set up giving reliable measurements.

Gálvez, Rodríguez, Sánchez-Gálvez and Navarro are a case in hand. They recently carried out a series of dynamic Brazilian tests on several advanced ceramics to show the feasibility of this experimental method to get the tensile strength at high strain rates [164, 73, 71, 72]. They studied six different materials: three aluminas (Al_2O_3) with different grain size and degree of purity, alumina blended with zirconia (Al_2O_3+ZrO_2), silicon carbide (SiC) and boron carbide (C_4B); the specimens were cylinders whose diameter and thickness were 8 and 4 mm respectively. The increase in the tensile strength for the dynamic tests (performed at strain rates ranging from 65 to 89 s^{-1}) with respect to the static tests (7 to 10×10^{-7} s^{-1}) varied from 20% for the SiC to almost 90% for the blend of alumina and zirconia. They also studied the rupture mechanisms by means of high-speed photography and performed a fractographic study of the crack surfaces using a scanning electron microscope. The latter revealed that there was no hint of plastic deformation and that the fracture was predominantly transgranular, with no change in the fracture mode with the strain rate [71, 72].

Here we use their results to validate a model that was originally applied to concrete undergoing the same test conditions [168] and that also gave good results studying the propagation of dynamic cracks under mixed-mode loading [169]. It consists of a finite element model which allows fragmentation, i.e. the opening of a crack where and when tension reaches the tensile strength, and that uses a mixed-mode cohesive model to control the fracture process [133].

Cohesive models are suitable for simulating cracking processes in advanced ceramics, since these materials, in spite of their relative small grain size, develop long fracture process zones —of the order of millimeters, depending on the microstructure and geometry of the specimen— due to the bridging and interlocking of the grains in the wake

of the crack [189, 25, 89, 77, 184]. These process zones constitute the main energy dissipation mechanism for this kind of materials [26, 184]. Indeed, cohesive theories applied to advanced ceramics have successfully explained the dependency of some of their properties and methods of characterization —like the R-curve— on the shape and size of the specimen [63, 150]. Furthermore, cohesive models are feasible for handling the dynamic effects appearing in advanced ceramics, for they automatically discriminate between slow and fast rates of loading [30] and thus there is no need to include the rate dependency within the description of the constitutive equations.

Another interesting feature of our finite-element model is the explicit treatment of fracture and fragmentation [141]. It tracks individual cracks as they nucleate, propagate, branch and possibly link up to form fragments, the ensuing granular flow of the comminuted materials also simulated explicitly. It is incumbent upon the mesh to provide a rich enough set of possible fracture paths since the model allows decohesion to occur along element boundaries only. However, no mesh dependency is expected as long as the cohesive elements adequately resolve the fracture process zone of the material [168, 30]. It is also interesting to note that the microinertia attendant to the material in the dynamic fragmentation process contributes to the correct simulation of the rate effects [168, 169, 30].

The simulations in this paper give a good prediction of the tensile strength for each material and come out with crack patterns very similar to the actual ones observed in the experiments. The model predicts the formation of a principal crack that nucleates in the center of the specimen and grows towards the bearing areas, as well as some secondary cracking parallel to the main crack and near to the loading areas.

The paper is organized as follows: a brief account of the main assumptions of the model and of its finite element implementation is given next. Section 4.3 describes the experimental set-up (4.3.1), the specimen geometry and material parameters (4.3.2), the load and boundary conditions (4.3.3), the mesh used in the simulations (4.3.4), and the simulation results (4.3.5). Finally, in Section 4.4, we draw several conclusions regarding the applicability of cohesive models to study the dynamic behavior of advanced ceramics.

4.2 Finite-element model

For completeness and posterior reference, in this section we summarize the main features of the cohesive law used in the calculations. An extensive account of the theory

and its finite-element implementation may be found elsewhere [133, 30].

A simple class of mixed-mode cohesive laws accounting for tension-shear coupling (see Camacho and Ortiz [30] and others [133, 51]) is obtained by the introduction of an effective opening displacement δ, which assigns different weights to the normal δ_n and sliding δ_S opening displacements

$$\delta = \sqrt{\beta^2 \delta_S^2 + \delta_n^2}, \qquad \delta_n = \boldsymbol{\delta} \cdot \boldsymbol{n}, \qquad \delta_S = |\boldsymbol{\delta}_S| = |\boldsymbol{\delta} - \delta_n \boldsymbol{n}|. \tag{4.1}$$

Here δ_n and δ_S are the normal and tangential opening displacements across the cohesive surface, respectively. Assuming that the cohesive free-energy density depends on the opening displacements only through the effective opening displacement δ, the cohesive law reduces to [30, 133]

$$\boldsymbol{t} = \frac{t}{\delta}(\beta^2 \boldsymbol{\delta}_S + \delta_n \boldsymbol{n}), \tag{4.2}$$

where

$$t = \sqrt{\beta^{-2} |\boldsymbol{t}_S|^2 + t_n^2} \tag{4.3}$$

is an effective cohesive traction, to be related to δ by a reduced cohesive law, and $\boldsymbol{t}_S$ and t_n are the shear and the normal tractions, respectively. From this relationship, we observe that the weighting coefficient β defines the ratio between the shear and the normal critical tractions (and thus it also roughly defines the ratio of K_{IIc} to K_{Ic}). We assume the existence of a loading envelope defining a relation between t and δ under the conditions of monotonic loading. We additionally assume that unloading is irreversible. A simple and convenient type of irreversible cohesive law is furnished by the linearly decreasing envelope shown in Fig. 4.1, where σ_c is the tensile strength and δ_c the critical opening displacement. Following Camacho and Ortiz [30] we assume linear unloading to the origin, Fig. 4.1.

Cohesive theories introduce a well-defined length scale into the material description and, in consequence, are sensitive to the size of the specimen (see, e.g. Reference [16]). The characteristic length of the material may be expressed as

$$\ell_c = \frac{E G_c}{f_{ts}^2} \tag{4.4}$$

where G_c is the fracture energy and t_{ts} the static tensile strength. Camacho and Ortiz [30] have noted that, when inertia is accounted for, cohesive models introduce a

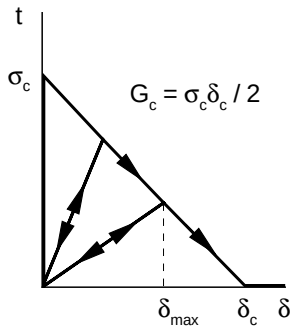

Figure 4.1: Linear irreversible cohesive law.

characteristic time as well. This characteristic or intrinsic time is:

$$t_c = \frac{\rho c \delta_c}{2 f_{ts}} \tag{4.5}$$

where ρ is the mass density and c the longitudinal wave speed. Owing to this intrinsic time scale, the material behaves differently when subjected to fast and slow loading rates. This sensitivity to the rate of loading confers to cohesive models the ability to reproduce subtle features of the dynamic behavior of brittle solids, such as crack-growth initiation times and propagation speeds [168, 138], and the dependence of the pattern of fracture and fragmentation on strain rate [140]. In addition, they account for the dynamic strength of brittle solids, i.e., the dependence of the dynamic strength on strain rate [168].

In calculations, we allow for decohesion to occur along element boundaries only. Initially, all element boundaries are perfectly coherent and the elements conform in the usual sense of the displacement finite element method. When the critical cohesive traction is attained at the interface between two volume elements, we proceed to insert a cohesive element at that location. The cohesive element subsequently governs the opening of the cohesive surface. Details of the finite element implementation may be found elsewhere [30, 133]

4.3 Simulation of the dynamic behavior of advanced ceramics

The simulations in this paper refer to experiments reported by Rodríguez, Navarro and Sánchez-Gálvez [164], Gálvez, Rodríguez and Sánchez Gálvez [73], Gálvez [71] and Gálvez, Rodríguez and Sánchez-Gálvez [72]. The experiments consist of Brazilian tests performed with a Hopkinson bar on six different advanced ceramics. As follows we briefly describe the experimental set-up (4.3.1), the specimen geometry and material parameters (4.3.2), the load and boundary conditions (4.3.3), the mesh used in the simulations (4.3.4), and the simulation results (4.3.5).

4.3.1 Experimental set-up

The Hopkinson bar consists of an incident bar and a transmitter bar, with a short specimen placed between them and a striker bar that produces an impact on the incident bar to generate a longitudinal compressive pulse that propagates toward the specimen (Fig. 4.2a). The pulse is partially reflected in the border of the incident bar, and partially transmitted through the specimen. In this case the diametral loading generates tension perpendicular to the load plane (Fig. 4.2b), which eventually causes the specimen to split.

The strain records of the incident, reflected and transmitted pulses are used to calculate the corresponding stress pulses and the tensile stress in the loading plane, which derives from the following equation:

$$\sigma = \frac{2\,P}{\pi\,W\,D} \tag{4.6}$$

where P is the load transmitted through the cylinder and W and D are respectively the width and diameter of the cylinder. P is in turn calculated from the transmitted stress. The dynamic tensile strength, f_{td}, is obtained using Eq. (4.6) for the maximum transmitted load. The strain rate follows as

$$\dot{\epsilon} = \frac{1}{E}\frac{\partial \sigma}{\partial t} \tag{4.7}$$

where E is the elastic modulus of the specimen material, σ is given by (4.6), and the derivative is restricted to the linear ramp-up of the stress history.

The experimental set-up was completed with a high speed photography system which was synchronized with the mechanical pulses so as to obtain several shots during the fracture process.

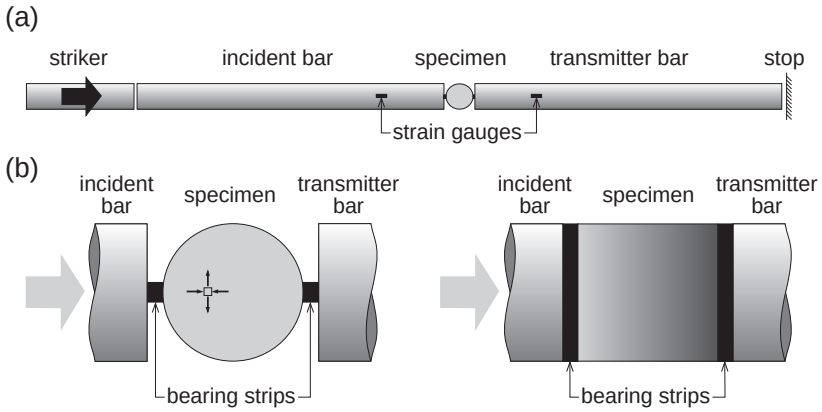

Figure 4.2: Experimental set-up (a), and details of the specimen (b).

4.3.2 Specimen geometry and material parameters

The specimens are cylinders whose diameter and thickness are 8 mm and 4 mm respectively. The authors of the experimental program tested up to six different materials: three kinds of alumina with 94, 98 and 99% degree of purity (which from now on are referred to as A94, A98 and A99), a combination of alumina plus zirconia (AZR), silicon carbide (SiC) and boron carbide (B4C). Geometrical and static mechanical properties are given in Table 4.1. All of them were obtained by independent tests except the fracture energy, that is estimated here from a general handbook on ceramics [171]. The characteristic length and time are calculated from the rest of the properties using (4.4) and (4.5). The coupling parameter β is taken to be 2 for all materials after some references reporting the ratio K_{IIc}/K_{Ic} for alumina and other advanced ceramics [174, 175, 173, 178, 183]. The influence of the β parameter is negligible though, because the crack opens mainly in mode I [168]. The cohesive envelope is assumed to be linear-irreversible, which seems to be a convenient and reasonable choice after some investigations devoted to characterize the fracture process zone in advanced ceramics [184, 77, 165, 78].

4.3.3 Load and boundary conditions

Figure 4.3 shows the stress history generated in the bars during one of the tests of a SiC specimen, which the authors of the experimental program provided us with. The dashed line averages the oscillations in the plateau of the incident pulse and it was used

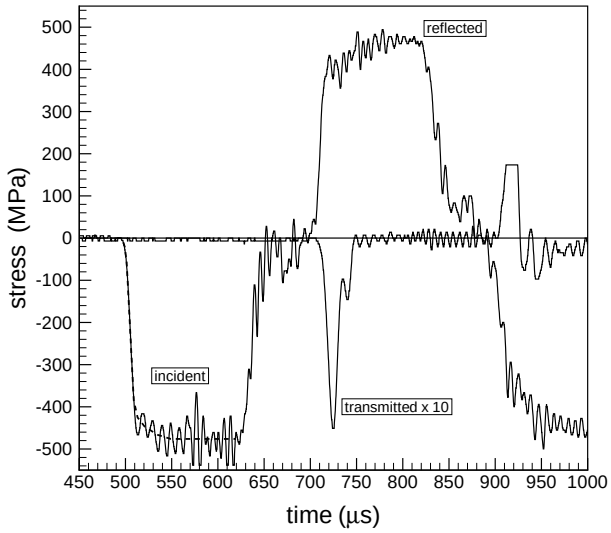

Figure 4.3: Incident stress pulse.

to estimate the prescribed velocity at contact with the specimen by using the following relation [123]

$$v = \frac{\sigma}{\rho c}, \tag{4.8}$$

where ρ and c are the density and wave speed of the incident bar respectively, and σ is the incident stress. Eq. (4.8) simply amounts to requiring that the motion of the specimen matches the incident wave profile. By way of contrast, the contact between the specimen and the transmitter bar is assumed to be rigid, leading to constrained displacements over the width of the bearing area. This simplification is warranted by the observation that the transmitted pulses measured in the tests were very weak, approximately one order of magnitude lower than the incident pulses (Fig. 4.3).

In order to avoid plastic deformation in the bars, the specimens were stricken through alumina cubes whose edges were on average 6 mm long. There were some tests in which the cubes together with the specimen broke, but these were not considered valid. By measuring the imprints left in these cubes by the cylinders after the tests, it was determined that the width of the loading area varied from 5 to 10% of the diameter length. Nevertheless, in the simulations we opted for a bearing width of 16% of the diameter in order to avoid spurious fragmentation near the supports. Rocco

Material name	A94	A98	A99	AZR	SiC	B4C
Composition	Al_2O_3 94%	Al_2O_3 98%	Al_2O_3 99%	Al_2O_3+ZrO_2	SiC	B_4C
Average grain size (μm)	8.3	2.4	10.4	2.0	3.3	–
Density (kg/m^3)	3658	3877	3905	4027	3132	2512
Static mechanical properties						
Elastic modulus (GPa)	303	366	391	348	420	461
Tensile strength (MPa)	161	179	161	155	214	211
Fracture energy (N/m)	119	98	92	162	38	88
Characteristic cohesive parameters						
Length (mm)	1.4	1.1	1.4	2.3	0.35	0.91
Time (μs)	0.15	0.12	0.14	0.25	0.031	0.069

Table 4.1: Geometrical and static mechanical properties.

et al. [162, 161] showed that, in static Brazilian tests and for high values of the ratio D/ℓ_c (diameter/characteristic length), the relative error in the tensile strength given by this increase of the bearing width is of 3%, which, bearing in mind the scatter of the experimental results, can be viewed as negligible.

4.3.4 Meshes used in the simulations

In order to make the simulations in 3D computationally efficient, we take a slice of 1/3 mm, which is 1/12 of the real thickness of the specimen, and impose plane strain boundary conditions. Figure 4.4 shows the meshes used in the simulations. The one on the left comprises 2462 10-node quadratic tetrahedra. The average distance between nodes in the midplane of the cylinder is 1/18 mm, which ranges from 1/6 to 1/40 of the characteristic cohesive length of the material in the cases we are studying. For instance, for A99 the characteristic length is calculated to be 1.4 mm, which is about 25 times the average distance between nodes, and thus it follows that the characteristic length is adequately resolved [30, 168].

Nevertheless, for SiC we have $\ell_c = 0.35$ mm, roughly 6 times the average distance between nodes with the mesh on the left in Fig. 4.4. Hence, in order to check whether the results for this material show mesh-dependency or not, we also consider the finer mesh in Fig. 4.4, which is formed by 5814 10-node quadratic tetrahedra. There are 485 nodes in the midplane, and thus the average distance between nodes is 1/60 mm.

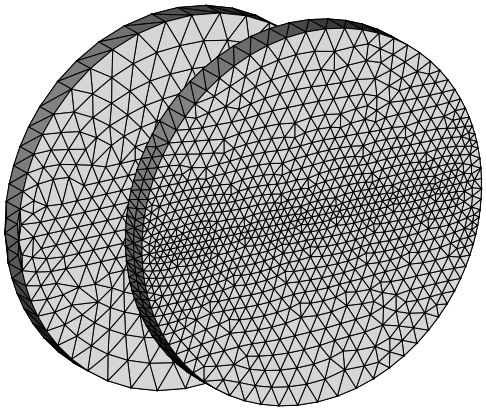

Figure 4.4: Meshes used in the simulations.

It follows that the characteristic length of SiC is resolved in this case by 21 nodes. The results for SiC using the regular and the finer mesh are basically the same in terms of transmitted load and of energy dissipation up to the complete unloading of the specimen and thus we can conclude that even the regular mesh in Fig. 4.4 gives a good resolution for the six different materials.

It should be carefully noted that, unlike other brittle or quasi-brittle materials like concrete, for the advanced ceramics we are dealing with here the characteristic length is of two orders of magnitude above the average grain size (see Table 4.1), and so capturing the grain length scale by choosing an element size of that order of magnitude would lead to extremely fine meshes, and subsequently to a very long computational time. Nevertheless, these materials develop fracture process zones comparable in size to the characteristic length [189, 25, 89, 77, 184], and so as long as the characteristic length is adequately resolved, the simulations are expected to give objective and mesh-size insensitive results [30]. A detailed study of the convergence upon mesh refinement in a similar problem can be found in [168].

4.3.5 Simulation results

Selected results of the calculations and comparisons with experimental data are presented in Table 4.2 and in Figs. 4.5–4.8. The main features of these results are discussed next.

Dynamic strength and rate sensitivity

The dynamic tensile strength and corresponding strain rate emerging from the simulations, together with the experimental results (mean value and standard deviation), are presented in Table 4.2 for all the materials under consideration. Figure 4.5 shows the same data in a bar chart. It includes a bar representing the static tensile strength, graphically demonstrating the rate effects.

The precision in the calculation of the peak transmitted load and, by extension, of the dynamic strength, Eq. (4.6), is noteworthy, specially in the case of A99, SiC and B4C, where the relative error of the computed dynamic strength is less than 5%. It is also remarkable that the strain rate calculated with Eq. (4.7) from the output of the numerical tests fit the experimental strain rate very accurately. Indeed, the relative error in the strain rate for the three aluminas is once again below 5%.

It bears emphasis that these features of the dynamic behavior of advanced ceramics are *predicted* by the theory. In fact, the sole strength parameter of the theory is the static tensile strength of the cohesive material. In addition, the cohesive law is itself rate-independent. The good correlation between theory and experiments just reported suggests that microinertia associated with microcracking and dynamic fracture is the dominant mechanism underlying the effective rate-sensitivity of advanced ceramics. This same conclusion is furnished by the fractographic analysis performed on the crack surfaces [71, 72], which showed that there was no hint of plastic deformation and which did not reveal any change in the fracture mode, predominantly transgranular, with the strain rate.

The aforementioned lack of change in the micromechanisms of fracture is in apparent contradiction with experimental findings by Kobayashi [89], who reported an increase in the percentage areas of transgranular fracture (associated with a higher specific energy consumption) with faster crack propagation. Nevertheless, it is important to notice that the crack velocity is not directly proportional to the strain rate in the loading plane obtained by Eq. (4.7), and actually all of the static tests were unstable [71], i.e. the elastic energy stored in the specimen was suddenly released leading to the formation of the crack and to its subsequent fast propagation. The crack speed in the static tests may not be as fast as in the dynamic tests, but is fast enough to produce the same degree of transgranular fracture. Regrettably the crack speed was not measured in the tests we are studying here and so we cannot quantify its relation to the strain rate.

As regards the reported standard deviations in Table 4.2, it is evident that the experimental scatter is substantial. For instance, focusing on the SiC tests only, the

	A94	A98	A99	AZR	SiC	B4C
Static tests						
f_{ts} (MPa)	161 (23)	179 (21)	161 (26)	155 (12)	214 (55)	211 (52)
$\dot{\epsilon}$ ($10^{-8}\,s^{-1}$)	83 (13)	92 (36)	73 (29)	99 (3)	69 (6)	69 (6)
Dynamic tests						
f_{td} (MPa)	278 (28)	285 (31)	243 (43)	288 (30)	248 (58)	261 (50)
$\dot{\epsilon}$ (s^{-1})	89 (14)	77 (10)	76 (20)	85 (10)	66 (18)	65 (12)
Numerical tests						
f_{td} (MPa)	230	256	235	240	245	272
$\dot{\epsilon}$ (s^{-1})	88	80	74	94	71	77
Error in						
f_{td} (%)	17	10	3	17	1	4
$\dot{\epsilon}$ (%)	1	4	3	11	8	18

Table 4.2: Tensile strength and strain rate emerging from the tests. The experimental standard deviation is shown in brackets.

standard deviation of the dynamic strength is 23% of the mean value. Actually, the values obtained for f_{td} among the 9 SiC specimens that were tested varied form 162 to 327 MPa [71]. These differences in the response of nominally identical specimens subjected to the same loading conditions are inherent to ceramics, mainly due to the presence of a random distribution of small defects and impurities within the bulk of the material. Other sources of scatter can be found, for example, in the virtual impossibility of repeating the same incident pulse, or in small variations in the local conditions at the supports. Of course, there are also sources of uncertainty in the computed solutions, in spite of the attainment of convergence in terms of average macroscopic quantities as the dynamic strength or the strain rate. For instance, as alluded to above, our simulations show some spurious cracking near the supports for narrow width areas under some mesh configurations, and —as in [168]— the post-peak solution exhibits a random stochastic character. Both, experimental and numerical uncertainties, have to be borne in mind in making meaningful comparisons between real and simulated tests.

Crack patterns

The predicted sequence of crack patterns closely follows the experimental patterns observed by means of a high speed photography system [73, 71]. Figs. 4.6a and 4.7a show two snapshots corresponding to a SiC specimen, to be specific the one labeled BRSIC04 in [71]. The first shot (Fig. 4.6a) was taken exactly at the peak load and the

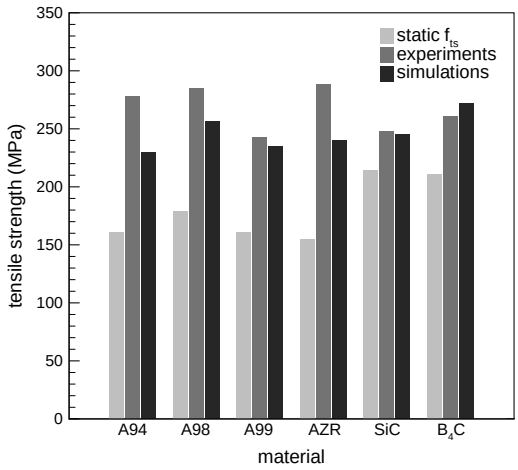

Figure 4.5: Comparison between the experimental and numerical dynamic tensile strength for each material. The static tensile strength is also displayed to show the effect of the strain rate.

second one falls right in the bottom of the valley before the secondary peak (Fig. 4.8). The delay between the two shots was 10 μs, and the exposure time for the two of them was 2 μs. Figs. 4.6b and 4.7b depict their numeric counterparts showing the distribution of cracks. It should be carefully noted that in these plots, in order to aid visualization, displacements have been magnified by a factor of 10. Also shown in the figures are level contours of damage, defined as the ratio of expended fracture energy to total fracture energy per unit surface. A fully cracked surface is shaded in black, whereas the zones that are intact remain in white, and as damage progresses between the two extremes the shade representing the damage goes through the gray scale. It is worth emphasizing that this damage field is defined on any internal surface of the body, and thus in Figs. 4.6b and 4.7b the damage field just remarks the location of the cracks as they appear in the front circular surface.

Remarkably, both the experimental observation and the numerical solution exhibit a main crack on the midplane of the specimen which initiates near the center of the cylinder and subsequently propagates towards the bearing areas, eventually causing the specimen to split into two main fragments. This through-crack is clearly seen in the snapshots in Fig. 4.6, which are taken just at the peak-load.

In keeping with experimental observation, Fig. 4.7b further reveals the development

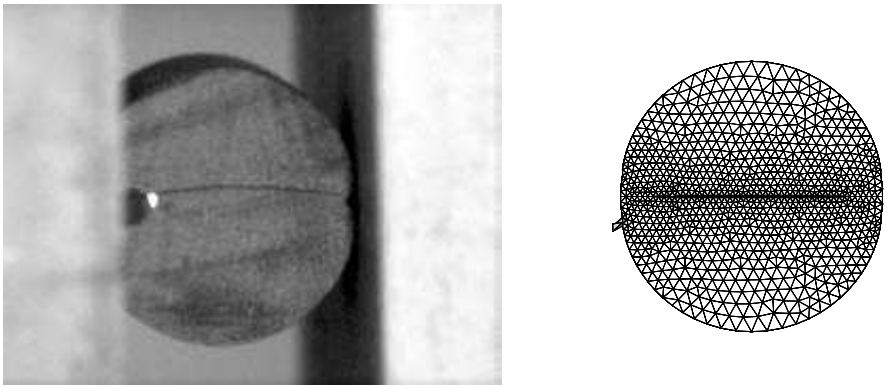

(a) (b)

Figure 4.6: Snapshot of the main crack appearing at the peak load in a SiC specimen (a), compared to its numeric counterpart (b).

of profuse cracking at the loading areas which even leads to some fragmentation. Secondary cracks, parallel to the main diametral crack, also appear as the load decreases, leading to the typical columnar failure of Brazilian tests [160]. The simulation also captures the inclined cracks leading to the formation of a wedge under the loading areas, as can be seen in the right part of the cylinder in Fig. 4.7b. This generalized microcracking occasions a sharp upturn in energy dissipation, as we will note in the next section by the energy history provided by the simulations. The ability to account for such complex fracture patterns with relative ease is a remarkable feature of cohesive theories of fracture.

Load and energy history curves

Figure 4.8 shows the load and energy history curves for a SiC specimen. The data are rendered in dimensionless form in order to facilitate the discussion that follows later in this section. To this end, we define the normalized transmitted load as:

$$P^* = \frac{\sigma}{f_{ts}}, \tag{4.9}$$

where σ is given by Eq. (4.6). With this convention P^* gives the ratio f_{td}/f_{ts} at peak load, and $P^* = 1$ when the transmitted load is equal to the theoretical maximum static load. We normalize the cumulative cohesive energy W_{coh} by the fracture energy

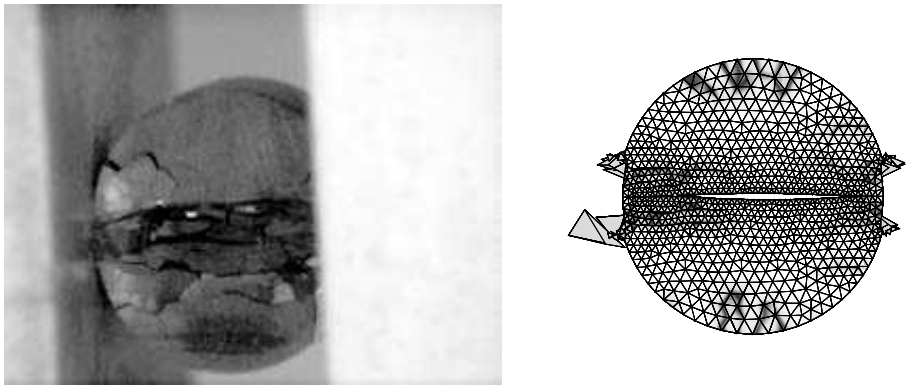

(a) (b)

Figure 4.7: Snapshot of the crack pattern at the bottom of the valley previous to the secondary peak load in a SiC specimen (a), compared to its numeric counterpart (b).

required to cleave the cylinder along its load plane into two equal half-cylinders, with the result:

$$W^*_{\text{coh}} = \frac{W_{\text{coh}}}{G_c W D}. \tag{4.10}$$

Finally, we define the normalized time as:

$$t^* = \frac{t}{t_c}\frac{\ell_c}{D}, \tag{4.11}$$

where t_c and ℓ_c are the characteristic time and length of the material, respectively, Eqs. 4.5 and 4.4 (the factor ℓ_c/D would bring to coincidence the initial stages of the numeric $P^* - t^*$ curves for specimens of different materials and different sizes).

It should be noted that the experimental scattering makes it difficult to compare our results with experimental transmitted load curves even for nominally identical specimens. Nevertheless, we choose an artifact to do so here, consisting of plotting an experimental curve after multiplying both records (P^* and t^*) by the coefficients that take it to give the mean experimental values. This curve is the dashed line in Fig. 4.8a, and corresponds to the same test discussed in the previous section (SiC specimen labeled BRSIC04 in [71]). It gave a dynamic tensile strength of 162 MPa at a strain rate of 36 s^{-1}, in both cases far below the mean values. The solid curves are given by the simulation of a SiC specimen using the fine mesh in Fig. 4.4, the S-shaped

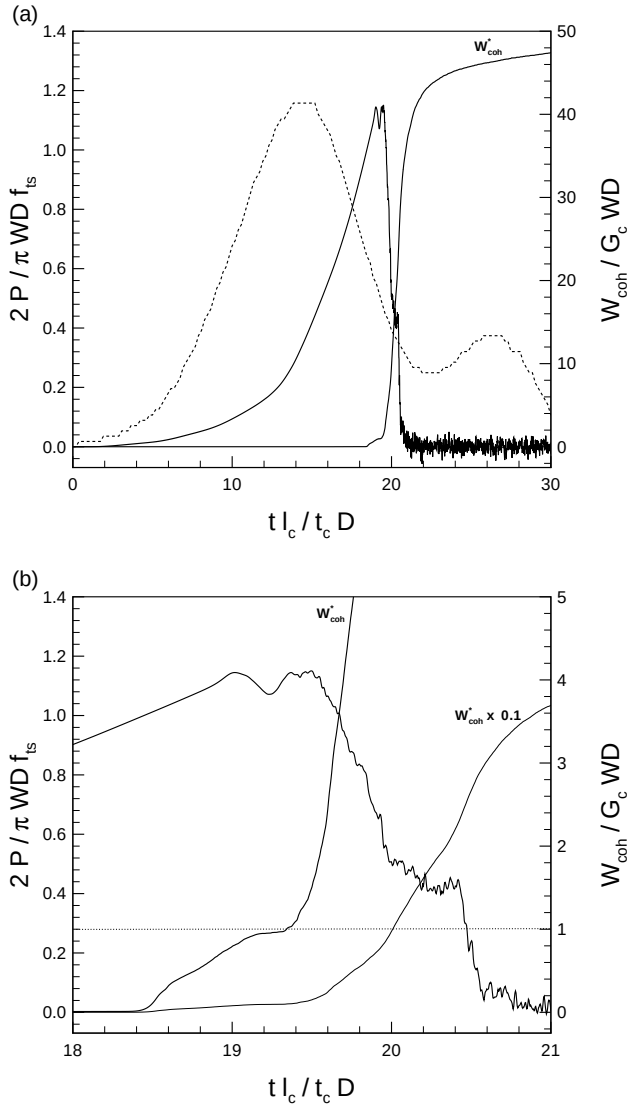

Figure 4.8: Simulated load and energy consumption histories for a SiC specimen (solid lines) and averaged experimental load history (dashed line) (a). Details of the peak and post-peak histories (b).

curve representing the normalized cumulative cohesive energy, W^*_{coh}.

It is interesting to note that the time required for elastic pressure waves to travel trough the diameter of the cylinder is of the order of 0.7 μs (approximately 1 in dimensionless time units). In view of the smoothness of the rising part of the transmitted load history, it would appear that the number of reverberations which take place during the ramp-up time of the loading pulse is sufficient to establish a rather uniform state of deformation within the specimen. It follows as a corollary that the waviness of the softening part of the load history curve is due to fracture processes rather than to wave effects. Furthermore, the absence of significant wave effects justifies the use of the test data for purposes of inferring constitutive properties of the material.

The comparison between load histories, experimental and numerical, displays graphically the good prediction of the dynamic tensile strength and of the strain rate, since both curves show the same maximum value and linear ramp-up slopes. The agreement is not as good when it comes to the time at which the peak takes place, which could be attributed to the imperfect simulation of the local conditions at the supports. It is also evident that the post peak behavior is rather sharp in the simulations. Indeed, the experimental curve unloads at 15×10^6 MPa/s, while the simulations predict roughly four times this unloading speed. By way of contrast, the softening part of the numerical curve catches interesting features, like the secondary peak due to the extension of microcracking throughout the specimen (Fig. 4.8b).

Regarding the cohesive energy curve, its S-shaped curve responds to the the way in which the fracture process of the specimen takes place. W^*_{coh} is strictly equal to zero while the specimen remains intact. Nevertheless, fracture starts before the maximum load is attained, as is revealed by Fig. 4.8b, which shows a linear ramp-up in the energy curve before the maximum load is reached and gives a value of $W^*_{\text{coh}} = 0.81$ at the peak load. Actually, as noted earlier, a main through-crack is well developed in the loading plane when the specimen transmits the maximum load (Fig. 4.6). The development of this crack generates relief waves which temporarily halt the splitting process. The specimen subsequently reloads, inducing a further crack growth as well as some microcracking in the bearing areas. The energy consumption surpasses the energy required to split the cylinder into two halves, $G_c WD$ (which is indicated with a dotted line in Fig. 4.8b), and a new peak load is attained.

The softening part of the load curve corresponds to a great increase in the cohesive energy consumption caused by microcraking. It starts in the bearing areas and extends along planes parallel to the midplane, which leads to the formation of a columnar

pattern of cracks that is characteristic in splitting tests [160], as can be seen in Fig. 4.7. At some point the array of columns that has been formed is able to resist some external load before collapsing by buckling, which generates a secondary peak that can be clearly seen in Fig. 4.8b. The simulations predict a value for this peak of $P^* = 0.45$, roughly 20% above the secondary peak given by the averaged experimental curve, which again attests to the fidelity of the simulations to the actual rupture mechanisms. This new loading process is accompanied by the opening of the parallel cracks, which generates a higher rate of cohesive energy consumption, and by the formation of new wedge-shaped inclined cracks due to the intensity of the shear stresses near the supports, Fig. 4.7. The simulations also report the formation of radial cracks starting in the circular border and growing to the center, Fig. 4.7b. After the secondary peak, microcracking advances up to virtually complete comminution of the cylinder. The rate of energy expenditure increases and, once the cylinder is not able to transmit load any more, tends to a horizontal asymptote representing the maximum energy consumption allowed by the mesh.

As regards the extension of microcracking in dynamic Brazilian tests, it has been noted [168] that it depends on the size of the specimen. For small sizes microcracking extends to the entire specimen and the expenditure of fracture energy increases linearly with the diameter, while for large sizes the effect of microcracing becomes increasingly localized and therefore the expended fracture energy tends asymptotically to the nominal value $G_c WD$ when D increases. Logically, there is a threshold diameter, D_c, that separates the two aforementioned trends, and it can be expressed as [168]:

$$D_c = \frac{P_{\max}}{2W\sigma_c}, \tag{4.12}$$

where $P_{\max}$ is the maximum applied load and σ_c is the tensile strength of the material. For the calculations shown in Fig. 4.8 one has $D_c = 7.2$ mm. Thus, the SiC cylinders we are studying here —whose D is 8 mm— are close to the transitional regime in which the effect of microcracking saturates, as it is confirmed by both the experiments and the simulations.

4.4 Summary and conclusions

We used cohesive theories of fracture, in conjunction with the direct simulation of fracture and fragmentation, to describe processes of tensile damage and compressive crushing in advanced ceramics subjected to dynamic loading. Indeed, cohesive models

are suitable for simulating cracking processes in advanced ceramics, since these materials develop long fracture process zones —two or three orders of magnitude longer than the average grain size— due to the bridging and interlocking of the grains in the wake of the crack, and these process zones constitute the main energy dissipation mechanism for this kind of materials.

The configuration contemplated in this study is the Brazilian cylinder test performed in a Hopkinson bar, which has been proposed as a convenient and reliable experimental method to obtain the dynamic tensile strength of these materials. Our approach accounts explicitly for the development of macroscopic cracks, and uses a mixed-mode cohesive law to control the fragmentation process. The effective dynamic behavior of six different types of advanced ceramics is predicted as an outcome of the calculations. In particular, our simulations capture closely the experimentally observed rate-sensitivity of the dynamic strength of advanced ceramics, i.e., the increase in dynamic strength with strain-rate. The model also predicts key features of the fracture pattern such as the primary cracks in the load plane, as well as the secondary profuse cracking near the supports and along planes parallel to the load plane.

We have assumed that the cohesive properties of the material are rate-independent and therefore determined by static properties such as the static tensile strength. However, we have noted that cohesive theories, in addition to building a characteristic length into the material description, endow the material with an intrinsic time scale as well. This intrinsic time scale accounts for the ability of the model to predict key aspects of the dynamic behavior of advanced ceramics, such as the strain-rate sensitivity of the tensile strength. Our results suggest, therefore, that most of the strain-sensitivity of advanced ceramics is attributable to the microinertia attendant to dynamic microcracking and fracture.

4.5 Acknowledgments

We are indebted to Prof. Michael Ortiz for providing us with access to his numerical codes at the Graduate Aeronautical Laboratories, California Institute of Technology, as well as for his advice during the development of this work. We are also thankful to Dr. Francisco Gálvez and Prof. Jesús Rodríguez for providing us with some records of their tests and insights into their excellent experimental work. Rena C. Yu and Gonzalo Ruiz thank the *Ministerio de Educación, Cultura y Deporte*, Spain, for the scholarship SB2000-0191, which makes possible their joint work at the *ETSI de Caminos, C., y*

P., Universidad de Castilla-La Mancha (UCLM). Gonzalo Ruiz acknowledges financial support from the *Ministerio de Ciencia y Tecnología*, Spain, under grant MAT2000-0705, and the UCLM, Spain, under grant 011,1075.

Chapter 5

A Recursive-Faulting Model of Distributed Damage in Confined Brittle Materials

Abstract

We develop a model of distributed damage in brittle materials deforming in triaxial compression based on the explicit construction of special microstructures obtained by *recursive faulting*. The model aims to predict the effective or macroscopic behavior of the material from its elastic and fracture properties; and to predict the microstructures underlying the microscopic behavior. The model accounts for the elasticity of the matrix, fault nucleation and the cohesive and frictional behavior of the faults. We analyze the resulting quasistatic boundary value problem and determine the relaxation of the potential energy, which describes the macroscopic material behavior averaged over all possible fine-scale structures. Finally, we present numerical calculations of the dynamic multi-axial compression experiments on sintered aluminum nitride (AlN) of Chen and Ravichandran [33, 34, 35, 36]. The model correctly predicts the general trends regarding the observed damage patterns; and the brittle-to-ductile transition resulting under increasing confinement[1].

5.1 Introduction

This paper is concerned with the formulation of a model of distributed damage in brittle materials under triaxial compression. The conditions under consideration here arise in a number of situations of interest, including: geological formations; confined structural ceramics and brittle-matrix composites; crushed concrete; and others. The

[1] **This paper has been published in a peer reviewed journal paper in 2006**.
Anna Pandolfi, Sergio Conti and Michael Ortiz. A Recursive-Faulting Model of Distributed Damage in Confined Brittle Materials. *Journal of the Mechanics and Physics of Solids*, 54, 1972-2003, 2006.

objectives of the theory are to compute the effective or macroscopic behavior of the material from its elastic and fracture properties; and to predict the microstructures underlying the microscopic behavior. The present work is also concerned with the numerical implementation of the damage model within a concurrent multiscale framework; and with the validation of the model against the experimental data of [34] pertaining to compressive damage in confined ceramics.

Processes of distributed damage in brittle materials have been the subject of extensive research and have been modelled by a variety of means (e. g., [95, 129, 10, 15, 109, 179, 12, 55, 103, 39, 13]). Most of these models are empirical and are based on special solutions from linear elasticity, internal variable formalisms, and other modelling schemes. Local models of distributed damage have also been misapplied to processes of fracture in brittle solids under tension, where fracture mechanics is expected to govern the behavior of the solid. Indeed, the essential distinction between damage and fracture has not always been appreciated fully. Thus, whereas damage is a distributed processes and is described by constitutive laws relating stress to strain, fracture is localized to surfaces and is described, e. g., by cohesive laws relating tractions to opening displacements. One of the aims of the present paper is to elucidate the conditions under which damage occurs in a distributed fashion, and therefore can be described by a damage model. We show that distributed damage occurs when $J = \det(\boldsymbol{F}) < 1$, where $\boldsymbol{F}$ is the average or macroscopic deformation gradient. Thus, distributed damage, as opposed to fracture, is a compressive phenomenon and only occurs when sufficient confinement is present.

The approach followed in the present paper is based on methods of the calculus of variations, especially on recent work on fracture as a free-discontinuity problem [57, 68, 49]. Thus, we suppose that the displacement field jumps discontinuously across a *singular set* of co-dimension 1, and that the energy is composed of two terms: the elastic strain energy obtained by volume integration outside the singular set; and the cohesive fracture energy obtained by surface integration over the singular set (e. g., [50, 49]). However, in contrast to recent work on free-discontinuity problems in fracture mechanics, that has emphasized tensile conditions leading to the formation of isolated dominant cracks, here we envision conditions of triaxial compression resulting in a distributed singular set. We specifically consider singular sets that are composed of *recursive or nested faults*, and show that these microstructures or damage patterns suffice to fully relax the energy.

A recursive fault pattern may be constructed by introducing into the solid a family

of parallel planar cohesive cracks, or *faults*, and subsequently applying that construction recursively to the intervening matrix between the faults. Recursive faulting is similar to the sequential-lamination constructions used to relax non-convex energies arising in other areas of application [92, 47, 111, 69, 37, 142, 101, 118, 21, 60, 96, 134, 135, 7]. In particular, the different levels of faulting are only approximately compatible. However, recursive faulting differs from sequential lamination in some notable respects. Thus, the state of stress within each level of faulting is uniform, and therefore in equilibrium. This greatly simplifies the implementation of recursive faulting relative to sequential lamination algorithms, which must necessarily equilibrate the entire microstructure at considerable computational cost [135, 7]. By contrast, recursive faulting can be implemented simply by means of a recursive call, and the entire microstructure needs not be considered at any time during the construction.

The approximate compatibility between levels of faulting has the effect of building additional misfit elastic energy into the microstructure. We estimate this misfit elastic energy simply by modelling the approximate interfaces as rows of dislocation dipoles. This simple estimate permits the calculation of the separation between the faults, and provides a natural termination criterion for the recursive faulting algorithm. It should be carefully noted that recursive faults are likely to cease being optimal once the misfit elastic energy is taken into consideration. Experience with model problems in martensite and crystal plasticity [90, 91, 20, 40] suggest that more complex microstructures, e. g., involving fault branching, are likely to be optimal instead. However, these enhancements of the theory will not be consider here in the interest of simplicity.

We begin by considering rank-1 microstructures consisting of one single level of faulting. The kinematics of such microstructures,

The organization of the paper is as follows. In Section 5.2 the general recursive faulting model is built in steps. We begin by considering rank-1 microstructures consisting of one single level of faulting. The kinematics of such microstructures, the cohesive behavior of the faults and frictional characteristics are formulated in Section 5.2.1, Section 5.2.2, and Section 5.2.6, respectively. In all these and subsequent developments, we strongly rely on variational principles in order to complete the formulation of the model, implement it numerically and analyze it mathematically. In particular, we resort to time discretization in order to coach the incremental problem as a minimum problem. In Section 5.2.4 we exploit this variational structure in order to elucidate conditions for the inception of faulting; and in Section 5.2.5 we resort to the minimum principle and a simple non-local extension of the model in order to determine the op-

timal separation of the faults. Finally, in Section 5.2.7 we apply rank-1 construction recursively in order to generate more complex microstructures, which we term *recursive faulting* microstructures. The variational formulation also paves the way for an effective mathematical analysis of the quasistatic boundary value problem. The chief analysis tool that we bring to bear on the problem is relaxation. In particular, in Section 5.3 we characterize the relaxation of the faulting energy functional, starting from a continuous distribution of faults, with locally only one orientation. The relaxed energy functional describes the macroscopic behavior of the material averaged over such fine scale structures; the relaxation automatically includes recursive faulting, i. e., mixing of different faulting directions. In section Section 5.4, as of the range of application of the recursive faulting model and by way of validation, we proceed to simulate the dynamic multi-axial compression experiments on sintered aluminum nitride (AlN) of Chen and Ravichandran [33, 34, 35, 36]. Finally, concluding remarks and a critical discussion of the model are collected in Section 5.5.

5.2 Distributed damage by confined recursive faulting

The model is based on a particular class of deformations, or *microstructures*, consisting of nested families of equi-spaced cohesive faults bounding otherwise elastic matrix material. These microstructures are schematically shown in Fig. 5.1a. We shall refer to this mode of deformation as *recursive faulting*, and the resulting microstructures as *recursive faults*. The primary aim is to devise a means for the effective generation of recursive-fault microstructures and the computation of the effective behavior of the damaged or faulted material. We build the general model in steps. We begin by considering the simple case of one family of faults, and develop the corresponding kinematics of deformation. The assumption of faulting separates the requisite constitutive relations into two independent components: the behavior of the matrix, which we shall assume to be elastic for simplicity; and the behavior of the faults, which we shall assume to be governed by a cohesive relation in the fault initiation stage, and by Coulomb friction and contact henceforth. These aspects of the model are subsequently developed in turn. Finally, we note that the faulting construction can be applied *recursively* in order to generate complex fault patterns.

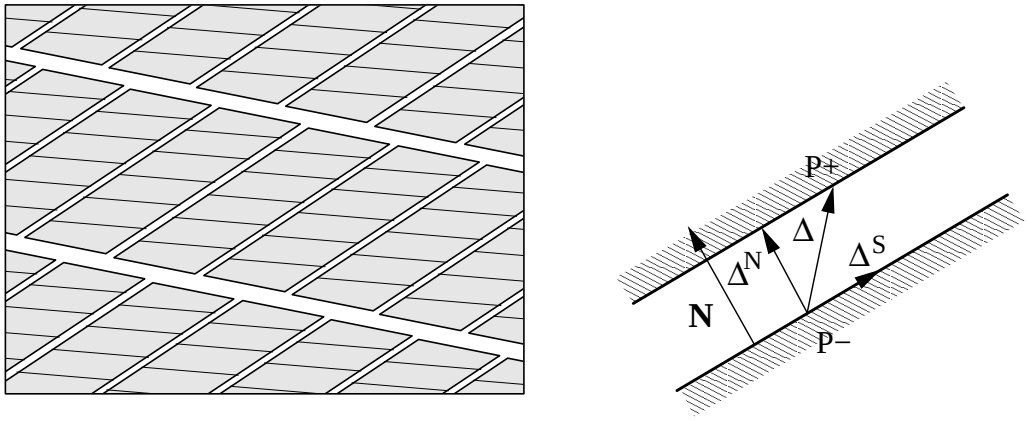

(a) (b)

Figure 5.1: (a) Schematic of the assumed kinematics of deformation, showing elastic blocks of matrix material bounded by nested faults. (b) Decomposition of the opening displacement $\boldsymbol{\Delta}$ into normal component and tangential components.

5.2.1 Kinematics

We begin by considering the particular case of a single family of fault planes of normal $\boldsymbol{N}$ and spacing L. Assuming strict separation of scales, consider a material vector $d\boldsymbol{X}$ which is short on the scale of the macroscopic deformations but much longer than L. Suppose that $d\boldsymbol{X}$ spans two material points P and Q in the reference configuration. The number of faults traversed by the vector is of the order of

$$n = \frac{1}{L}\, d\boldsymbol{X} \cdot \boldsymbol{N} \tag{5.1}$$

Suppose that an opening displacement $\boldsymbol{\Delta}$ is applied to each fault, Fig 5.1b. Let $d\boldsymbol{x}$ be the vector joining P and Q in the deformed configuration. Then,

$$d\boldsymbol{x} = d\boldsymbol{X} + n\boldsymbol{\Delta} = d\boldsymbol{X} + \frac{1}{L}(d\boldsymbol{X} \cdot \boldsymbol{N})\boldsymbol{\Delta} = (\boldsymbol{I} + \frac{1}{L}\boldsymbol{\Delta} \otimes \boldsymbol{N})d\boldsymbol{X} \equiv \boldsymbol{F}^p d\boldsymbol{X} \tag{5.2}$$

where

$$\boldsymbol{F}^p = \boldsymbol{I} + \frac{1}{L}\boldsymbol{\Delta} \otimes \boldsymbol{N} \tag{5.3}$$

may be regarded as the discontinuous or singular deformation component due to fault activity. Suppose in addition that the matrix is given a uniform deformation $\boldsymbol{F}^e$. Then

$$d\boldsymbol{x} = \boldsymbol{F} d\boldsymbol{X} \tag{5.4}$$

where

$$\boldsymbol{F} = \boldsymbol{F}^e \boldsymbol{F}^p \tag{5.5}$$

Thus we arrive at a multiplicative decomposition of the deformation gradient into a discontinuous and a matrix component. We note that, once $\boldsymbol{N}$ and L are supplied, $\boldsymbol{F}^p$ and $\boldsymbol{\Delta}$ are in one-to-one correspondence. In particular, the opening displacements $\boldsymbol{\Delta}$ follow from $\boldsymbol{F}^p$ through the relation

$$\boldsymbol{\Delta} = L\,(\boldsymbol{F}^p - \boldsymbol{I}) \cdot \boldsymbol{N} \tag{5.6}$$

We also note that the inverse of the $\boldsymbol{F}^p$ follows simply by an application of the Sherman-Morrison formula to (5.3), with the result:

$$\boldsymbol{F}^{p-1} = \boldsymbol{I} - \frac{1}{L + \boldsymbol{\Delta} \cdot \boldsymbol{N}} \boldsymbol{\Delta} \otimes \boldsymbol{N} \tag{5.7}$$

5.2.2 Cohesive stage

We assume that during the early states of damage immediately following the inception of of the faults, or *cohesive stage*, the opening of the faults is resisted by cohesive forces. In addition, we confine our attention to brittle materials that behave elastically in the absence of damage. A form of the free energy density consistent with these assumptions is:

$$A(\boldsymbol{F}, \theta, \boldsymbol{\Delta}, \boldsymbol{q}) = W^e(\boldsymbol{F}^e, \theta) + \frac{1}{L}\Phi(\theta, \boldsymbol{\Delta}, \boldsymbol{q}) \tag{5.8}$$

where W is the elastic strain-energy density per unit volume of the matrix, Φ is the cohesive energy per unit fault surface, θ is the absolute temperature, and $\boldsymbol{q}$ is some appropriate set of internal variables describing the state of the faults. The additive structure (5.8) of the free energy density is in line with general mathematical results pertaining to free-discontinuity problems. By material-frame indifference, it follows that W^e can only depend on $\boldsymbol{F}^e$ through the matrix right Cauchy-Green deformation tensor:

$$\boldsymbol{C}^e = \boldsymbol{F}^{eT} \boldsymbol{F}^e = \boldsymbol{F}^{p-T} \boldsymbol{C}\, \boldsymbol{F}^{p-1} \tag{5.9}$$

where $\boldsymbol{C} = \boldsymbol{F}^T\boldsymbol{F}$ is the right Cauchy-Green deformation tensor, whereupon (5.8) simplifies to:

$$A(\boldsymbol{F}, \theta, \boldsymbol{\Delta}, \boldsymbol{q}) = W^e(\boldsymbol{C}^e, \theta) + \frac{1}{L}\Phi(\theta, \boldsymbol{\Delta}, \boldsymbol{q}) \tag{5.10}$$

A simple class of three-dimensional cohesive laws governing the cohesive stage of the faults can be constructed as follows. Following [133], we begin by introducing an effective opening displacement of the form, Fig. 5.1b:

$$\Delta = \sqrt{(1-\beta^2)(\boldsymbol{\Delta}\cdot\boldsymbol{N})^2 + \beta^2|\boldsymbol{\Delta}|^2} \tag{5.11}$$

where $|\boldsymbol{\Delta}|$ is the magnitude or norm of $\boldsymbol{\Delta}$ and β is a material constant which assigns different weights to the normal and tangential components of the opening displacement. We now assume that the cohesive energy $\Phi(\theta, \boldsymbol{\Delta}, \boldsymbol{q})$ depends on $\boldsymbol{\Delta}$ only through the effective opening displacement Δ. In addition, we restrict attention to isothermal processes and omit all explicit references to the temperature θ for simplicity of notation. Under these conditions the cohesive potential takes the form

$$\Phi = \Phi(\Delta, \boldsymbol{q}) \tag{5.12}$$

The corresponding cohesive tractions are:

$$\boldsymbol{T} = \frac{\partial\Phi}{\partial\boldsymbol{\Delta}} = \frac{T}{\Delta}[(1-\beta^2)(\boldsymbol{\Delta}\cdot\boldsymbol{N})\boldsymbol{N} + \beta^2\boldsymbol{\Delta}] \equiv T\boldsymbol{d} \tag{5.13}$$

and the configurational force conjugate to $\boldsymbol{N}$, or configurational torque, is

$$\frac{\partial\Phi}{\partial\boldsymbol{N}} = \frac{T}{\Delta}(1-\beta^2)(\boldsymbol{\Delta}\cdot\boldsymbol{N})\boldsymbol{\Delta} \tag{5.14}$$

where

$$T = \frac{\partial\Phi}{\partial\Delta}(\Delta, \boldsymbol{q}) \tag{5.15}$$

is the effective traction and $\boldsymbol{d}$ is the traction direction. The tangent stiffness of the cohesive plane is given by:

$$\boldsymbol{K} = \frac{\partial^2\Phi}{\partial\boldsymbol{\Delta}\partial\boldsymbol{\Delta}} = \left(K - \frac{T}{\Delta}\right)\boldsymbol{d}\otimes\boldsymbol{d} + \frac{T}{\Delta}[(1-\beta^2)\boldsymbol{N}\otimes\boldsymbol{N} + \beta^2\boldsymbol{I}] \tag{5.16}$$

where

$$K = \frac{\partial T}{\partial\Delta}(\Delta, \boldsymbol{q}) \tag{5.17}$$

is the effective stiffness of the cohesive plane. A simple calculation gives the identity

$$T = \sqrt{(1-\beta^{-2})(\boldsymbol{T}\cdot\boldsymbol{N})^2 + \beta^{-2}|\boldsymbol{T}|^2} \tag{5.18}$$

which shows that T is a weighted combination of the normal and tangential tractions to the fault.

Following [30, 133], we render the cohesive law irreversible by assuming unloading to the origin. In this model, the sole internal variable q of the material is the maximum attained effective opening displacement, and the corresponding kinetic equation is, therefore,

$$\dot{q} = \begin{cases} \dot{\Delta}, & \text{if } \Delta = q \text{ and } \dot{\Delta} \geq 0 \\ 0, & \text{otherwise} \end{cases} \tag{5.19}$$

The first of these cases corresponds to *loading* or the faults and the second case to *unloading*. Let $\Phi_0(\Delta)$ be the monotonic cohesive energy, i. e., a function such that

$$T_0(\Delta) = \frac{\partial \Phi_0}{\partial \Delta}(\Delta) \tag{5.20}$$

$$K_0(\Delta) = \frac{\partial T_0}{\partial \Delta}(\Delta) \tag{5.21}$$

are the effective tractions and stiffness under monotonically growing Δ. Then, the cohesive energy and its derivatives follows as

$$\Phi(\Delta, q) = \Phi_0(q) + \frac{1}{2}\frac{T_0(q)}{q}(\Delta^2 - q^2) \tag{5.22}$$

$$T(\Delta, q) \equiv \frac{\partial \Phi}{\partial \Delta}(\Delta, q) = \frac{T_0(q)}{q}\Delta \tag{5.23}$$

$$-Y(\Delta, q) \equiv \frac{\partial \Phi}{\partial q}(\Delta, q) = \frac{1}{2}\big[K_0(q)q - T_0(q)\big]\left[(\Delta/q)^2 - 1\right] \tag{5.24}$$

$$K(\Delta, q) \equiv \frac{\partial T}{\partial \Delta}(\Delta, q) = \begin{cases} K_0(q), & \text{loading} \\ T_0(q)/q, & \text{unloading} \end{cases} \tag{5.25}$$

where $Y(\Delta, q)$ is the thermodynamic driving force for damage. We shall assume throughout the inequality

$$K_0(q)q < T_0(q), \tag{5.26}$$

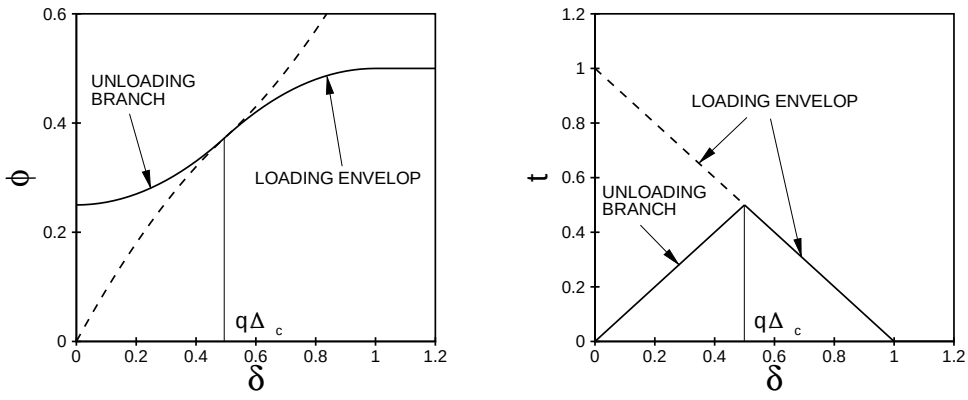

(a) (b)

Figure 5.2: Normalized linearly decreasing cohesive envelop: $\delta = \Delta/\Delta_c$, $\phi = \Phi(\Delta)/T_c\Delta_c$, $t = T/T_c$.

which ensures that unloading to the origin is well defined. This inequality is satisfied by all commonly used cohesive envelops.

For lack of a better term, we shall refer to the cohesive model described in the foregoing, consisting in the introduction of a scalar effective opening displacement, a monotonic cohesive envelop and unloading to the origin, as the *effective opening displacement* (EOD) cohesive model. In calculations we additionally use the simple cohesive envelop [30, 168, 169]:

$$\Phi_0 = \begin{cases} T_c\Delta - T_c\Delta^2/2\Delta_c, & \text{if } \Delta \leq \Delta_c \\ G_c = T_c\Delta_c/2, & \text{otherwise} \end{cases} \tag{5.27}$$

The corresponding cohesive law consists of rigid behavior, i. e., $\Delta = 0$, for $T < T_c$, followed by a linearly decreasing dependence of T on Δ for $\Delta < \Delta_c$, and $T = 0$ thenceforth, Fig. 5.2.

5.2.3 Time discretization

We shall strongly rely on variational principles in order to complete the formulation of the model, implement it numerically and analyze it mathematically. The behavior of irreversible materials can be characterized variationally by recourse to time discretization. To this end, we envision a process of incremental deformation and seek

to determine the state of the material at times t_0, ..., $t_{n+1} = t_n + \Delta t$, ... Suppose that the state of the material is known at time t_n and let the deformation $\boldsymbol{F}_{n+1}$ at time t_{n+1} be given. The problem is to determine the state of the material at time t_{n+1}.

We begin by considering the case in which one family of faults is present in the material and the behavior of the faults is cohesive. Following [136] we define an incremental strain-energy density

$$W_n(\boldsymbol{F}_{n+1}) = \inf_{\substack{\boldsymbol{\Delta}_{n+1},\, q_{n+1} \\ \boldsymbol{\Delta}_{n+1}\cdot\boldsymbol{N} \geq 0 \\ q_{n+1} \geq q_n}} A(\boldsymbol{F}_{n+1}, \boldsymbol{\Delta}_{n+1}, q_{n+1}) \tag{5.28}$$

We note that by virtue of the irreversibility constraint, $q_{n+1} \geq q_n$, $W_n(\boldsymbol{F}_{n+1})$ depends tacitly on the initial conditions at time t_n. We signify this dependence by means of the subindex n. In particular, $W_n(\boldsymbol{F}_{n+1})$ varies between time steps, which allows for irreversibility, hysteresis and path dependency. It should be noted that the irreversible character of the effective strain-energy density W_n is expressed through the damage scalar q_n and through the fault orientation $\boldsymbol{N}$ (see the case of an undamaged material in section 5.2.4). It can be shown [136] that $W_n(\boldsymbol{F}_{n+1})$ acts as a potential for the first Piola-Kirchhoff stress tensor $\boldsymbol{P}_{n+1}$ at time t_{n+1}, i. e., as

$$\boldsymbol{P}_{n+1} = \frac{\partial W_n}{\partial \boldsymbol{F}_{n+1}}(\boldsymbol{F}_{n+1}) \tag{5.29}$$

Consequently, the stable equilibrium configurations can be characterized as the minimizers of the corresponding potential energy.

The constraints appended to the minimum problem (5.28) can be enforced by means of Lagrange multipliers. The corresponding optimality conditions are (cf, e. g., [163])

$$\frac{\partial}{\partial \Delta_I}[A + \lambda_1 \boldsymbol{\Delta}\cdot\boldsymbol{N}] = -\frac{1}{L + \boldsymbol{\Delta}\cdot\boldsymbol{N}} N_J \frac{\partial W}{\partial F^e_{iJ}} F^e_{iI} + \frac{1}{L}\frac{\partial \Phi}{\partial \Delta_I} + \lambda_1 N_I = 0 \tag{5.30a}$$

$$\frac{\partial}{\partial q}[A + \lambda_2(q - q_n)] = \frac{1}{L}\frac{\partial \Phi}{\partial q} + \lambda_2 = 0 \tag{5.30b}$$

$$\boldsymbol{\Delta}\cdot\boldsymbol{N} \geq 0, \quad \lambda_1 \leq 0 \quad \text{and} \quad \lambda_1 \boldsymbol{\Delta}\cdot\boldsymbol{N} = 0 \tag{5.30c}$$

$$q - q_n \geq 0, \quad \lambda_2 \leq 0 \quad \text{and} \quad \lambda_2(q - q_n) = 0 \tag{5.30d}$$

where here and subsequently we have omitted the subindex $n+1$ for clarity of notation.

For the EOD cohesive model, the tractions $\partial_{\boldsymbol{\Delta}}\Phi$ in (5.30a) are given by (5.13), (5.15) and (5.23); and the driving force $-\partial_q\Phi$ in (5.30b) is given by (5.24). It is clear from the optimality conditions that λ_1 may be regarded as a contact normal traction and λ_2 as a driving force for damage. The Kuhn-Tucker condition (5.30c) then requires that the contact tractions be compressive during contact or zero during opening; and the Kuhn-Tucker condition (5.30d) then requires that the driving for damage be zero during damage or negative during unloading. These latter conditions are in analogy to rate-independent models of plasticity, which require the material to be at yield, i. e., the overstress to be zero during plastic deformation; and the response to be elastic when the material is below yield, i. e., when the overstress is negative.

A strategy for finding optimal solutions consists in looking first for an unloaded open-fault solution, i. e., assuming $\boldsymbol{\Delta}\cdot\boldsymbol{N}\geq 0$ and $q=q_n$. In this case, $\lambda_1=0$, $\lambda_2\geq 0$. Therefore, $\boldsymbol{\Delta}$ can be computed directly from (5.30a), e. g., by a Newton-Raphson iteration. The requisite tangents for this iteration are

$$\begin{aligned} L\frac{\partial^2 A}{\partial\Delta_I\partial\Delta_K} &= \frac{\partial^2\Phi}{\partial\Delta_I\partial\Delta_K}+\frac{L}{(L+\boldsymbol{\Delta}\cdot\boldsymbol{N})^2} \\ &\left[\frac{\partial^2 W}{\partial F^e_{iJ}\partial F^e_{kL}}F^e_{iI}F^e_{kK}N_L+\frac{\partial W}{\partial F^e_{iJ}}F^e_{iK}N_I+\frac{\partial W}{\partial F^e_{iJ}}F^e_{iI}N_K\right]N_J \end{aligned} \tag{5.31}$$

In addition, it follows from (5.30b) and (5.24) that $\Delta\leq q_n$. In reaching this conclusion we have used the constitutive inequality (5.26). Thus, the solution is valid if $\boldsymbol{\Delta}$ satisfies the inequalities: $\boldsymbol{\Delta}\cdot\boldsymbol{N}\geq 0$ and $\Delta\leq q_n$. Suppose now that the unloading-opening predictor fails to return a feasible solution. Then we repeat the calculation by activating the most violated constraint, i. e., we activate the contact constraint if $|\boldsymbol{\Delta}\cdot\boldsymbol{N}|<|q-q_n|$, and we activate damage if $|q-q_n|<|\boldsymbol{\Delta}\cdot\boldsymbol{N}|$. The iteration terminates when all the optimality conditions are satisfied simultaneously.

Once the optimal values of $\boldsymbol{\Delta}$ and q at time t_{n+1} are know, the first Piola-Kirchhoff stress tensor follows from (5.29) as

$$P_{Ji}=\frac{\partial W_n}{\partial F_{iJ}}=\left(\frac{\partial W}{\partial F^e_{iK}}F^e_{kK}\right)F^{-1}_{Jk} \tag{5.32}$$

The term is parenthesis follows directly from the elasticity of the matrix. The consistent tangent moduli follow by linearization of (5.29), i. e.,

$$D\boldsymbol{P}_{n+1}=\frac{\partial^2 W_n}{\partial\boldsymbol{F}_{n+1}\partial\boldsymbol{F}_{n+1}}(\boldsymbol{F}_{n+1}) \tag{5.33}$$

Evidently, the tangent moduli are symmetric owing to the potential character of the incremental stress-strain relations. A straightforward calculation gives

$$\frac{\partial P_{Ji}}{\partial F_{kL}} = \frac{\partial^2 W_n}{\partial F_{iJ}\partial F_{kL}} = \frac{\partial^2 A}{\partial F_{iJ}\partial F_{kL}} - \frac{\partial^2 A}{\partial F_{iJ}\partial \Delta_M}\left(\frac{\partial^2 A}{\partial \Delta_M \partial \Delta_N}\right)^{-1}\frac{\partial^2 A}{\partial \Delta_N \partial F_{kL}} \tag{5.34}$$

Again, the first term in this expression follows directly from the elasticity of the matrix as

$$\frac{\partial^2 A}{\partial F_{iJ}\partial F_{kL}} = \frac{\partial^2 W}{\partial F^e_{iM}\partial F^e_{kN}}(F^p)^{-1}_{JM}(F^p)^{-1}_{LN} \tag{5.35}$$

The second derivatives of A with respect to $\boldsymbol{\Delta}_{n+1}$ are given in (5.16). Finally, the cross derivatives required to evaluate the tangents (5.34) are found to be:

$$\frac{\partial^2 A}{\partial F_{iJ}\,\partial \Delta_K} = -\frac{1}{L + \boldsymbol{\Delta}\cdot\boldsymbol{N}}\left(\frac{\partial^2 W}{\partial F^e_{iL}\partial F^e_{nM}}F^e_{nK}F^e_{mL} + \frac{\partial W}{\partial F^e_{iM}}F^e_{mK}\right)F^{-1}_{Jm}N_M \tag{5.36}$$

5.2.4 Fault inception and orientation

Suppose that the material is undamaged at time t_n and that we are given the deformation $\boldsymbol{F}_{n+1}$ at time t_{n+1}. We wish to determine whether in insertion of faults is energetically favorable; and the optimal orientation of the faults. We ascertain these questions with the aid of the time-discretized variational formulation developed in the preceding question. Thus, for the given deformation $\boldsymbol{F}_{n+1}$ we test two end states of the material, one with faults and another without faults. The orientation of the faults in the latter state is obtained variationally, as described in this section. We then choose the end state which results in the lowest incremental energy density $W_n(\boldsymbol{F}_{n+1})$.

The optimal orientation $\boldsymbol{N}$ of the faults and the remaining state variables at time t_{n+1} follow from the extended minimum problem:

$$\begin{aligned} W_n(\boldsymbol{F}_{n+1}) = \inf_{\substack{\boldsymbol{\Delta}_{n+1},\, q_{n+1},\, \boldsymbol{N} \\ \boldsymbol{\Delta}_{n+1}\cdot\boldsymbol{N} \geq 0 \\ q_{n+1} \geq q_n \\ |\boldsymbol{N}|^2 = 1}} & A(\boldsymbol{F}_{n+1}, \boldsymbol{\Delta}_{n+1}, q_{n+1}, \boldsymbol{N}) \end{aligned} \tag{5.37}$$

The corresponding optimality conditions are

$$\frac{\partial}{\partial \Delta_I}[A + \lambda_1 \boldsymbol{\Delta}\cdot\boldsymbol{N}] = -\frac{1}{L+\boldsymbol{\Delta}\cdot\boldsymbol{N}} N_J \frac{\partial W^e}{\partial F^e_{iJ}} F^e_{iI} + \frac{1}{L}\frac{\partial \Phi}{\partial \Delta_I} + \lambda_1 N_I = 0 \tag{5.38a}$$

$$\frac{\partial}{\partial q}[A + \lambda_2 (q - q_n)] = \frac{1}{L}\frac{\partial \Phi}{\partial q} + \lambda_2 = 0 \tag{5.38b}$$

$$\frac{\partial}{\partial N_I}[A + \lambda_1 \boldsymbol{\Delta}\cdot\boldsymbol{N} + \lambda_3 |\boldsymbol{N}|^2] = - \frac{\Delta_J}{L+\boldsymbol{\Delta}\cdot\boldsymbol{N}} \frac{\partial W^e}{\partial F^e_{iJ}} F^e_{iI} + \frac{1}{L}\frac{\partial \Phi}{\partial N_I} + \lambda_1 \Delta_I + 2\lambda_3 N_I = 0 \tag{5.38c}$$

$$\boldsymbol{\Delta}\cdot\boldsymbol{N} \geq 0, \quad \lambda_1 \leq 0 \quad \text{and} \quad \lambda_1 \boldsymbol{\Delta}\cdot\boldsymbol{N} = 0 \tag{5.38d}$$

$$q - q_n \geq 0, \quad \lambda_2 \leq 0 \quad \text{and} \quad \lambda_2 (q - q_n) = 0 \tag{5.38e}$$

$$|\boldsymbol{N}|^2 = 1 \tag{5.38f}$$

For the EOD cohesive model the configurational torque $-\partial_{\boldsymbol{N}}\Phi$ in (5.38c) is given by (5.14), (5.15) and (5.23).

Suppose that the incipient fault undergoes opening, i. e., $\boldsymbol{\Delta}\cdot\boldsymbol{N} > 0$ and, correspondingly, $\lambda_1 = 0$. Then, it is possible to satisfy eqs. (5.38a) and (5.38c) simultaneously by setting $\boldsymbol{\Delta} = (\boldsymbol{\Delta}\cdot\boldsymbol{N})\boldsymbol{N}$. This identity in turn implies that the normal to the incipient fault aligns itself with the direction of opening. Then (5.38a) and (5.38c) reduce to the symmetric eigenvalue problem

$$S^e_{IJ} N_J = \Lambda N_I \tag{5.39}$$

where

$$S^e_{IJ} = F^e_{iI} \frac{\partial W^e}{\partial F^e_{iJ}} \tag{5.40}$$

is a symmetric second Piola-Kirchhoff stress tensor for the matrix, and

$$\Lambda = (L + \boldsymbol{\Delta}\cdot\boldsymbol{N})\frac{T}{L} = (L + \boldsymbol{\Delta}\cdot\boldsymbol{N})\left(\frac{T}{L}(1-\beta^2) + \frac{2\lambda_3}{\boldsymbol{\Delta}\cdot\boldsymbol{N}}\right) \tag{5.41}$$

It follows from the first of these identities that the eigenvalue Λ is a tensile principal stress of the matrix and, therefore, the case under consideration fails to yield solutions if the stress in the matrix is compressive in all directions. In cases of multiaxial tension, the largest tensile direction is energetically favorable since, by eq. (5.41), it corresponds to the largest effective traction T and hence results in the least expense of cohesive energy. When two or three of the principal stresses of the matrix are tensile and equal the optimal value of $\boldsymbol{N}$ is indeterminate and, in calculations, is chosen randomly.

Suppose that the matrix is in all around compression. Then the incipient faults are necessarily closed and deform by sliding, i. e., $\boldsymbol{\Delta} \cdot \boldsymbol{N} = 0$. Under these conditions, inserting (5.13) and (5.14) into (5.38a) and (5.38c) gives

$$-\frac{1}{L} S^e_{IJ} N_J + \frac{\beta T}{L} M_I + \lambda_1 N_I = 0 \tag{5.42}$$

$$-\frac{1}{L} S^e_{IJ} M_J + \lambda_1 M_I + \frac{2\lambda_3}{|\boldsymbol{\Delta}|} N_I = 0 \tag{5.43}$$

where $\boldsymbol{M} = \boldsymbol{\Delta}/|\boldsymbol{\Delta}|$ is the unit vector in the direction of $\boldsymbol{\Delta}$. Multiplying the first of these equations by $\boldsymbol{M}$ and the second by $\boldsymbol{N}$ we obtain the identities

$$\frac{1}{L} S^e_{IJ} M_I N_J = \frac{\beta T}{L} = \frac{2\lambda_3}{|\boldsymbol{\Delta}|} \tag{5.44}$$

The resulting equations imply that $\boldsymbol{N}$ is a plane of maximum shear of the matrix stress $\boldsymbol{S}^e$.

In summary, faults can form in two modes: opening and sliding. In the opening mode, the faults orient themselves so that their normal is aligned with the direction of opening. This mode can only occur if at least one of the principal directions of stress in the matrix is tensile. In the sliding mode, the incipient faults orient themselves along planes of maximum shear of the matrix. The sliding mode can operate when there are maximum shear planes that are under normal compression. In cases in which both the opening and sliding modes can operate, they are evaluated in turn and the operative mode is chosen to be the energy-minimizing one.

5.2.5 Nonlocal extension and the size of the microstructure

In the previous developments, the length L has been regarded as a known parameter. Alternatively, it can be computed variationally as part of the incremental update (5.28). However, in order to obtain meaningful values of the fault spacing L it is important to account for the *misfit energy*, i. e., the energy contained in the boundary layers that forms where the faults meet a confining boundary, Fig. 5.3a. Thus, the compatibility between the faults and their container is only *approximate*, or on average, and this gives rise to boundary layers that penetrate into the faulted region to a certain depth.

The effect of this extension is to replace a scale-invariant model by another model that contains a length scale. Mathematically, this extension may be regarded as the

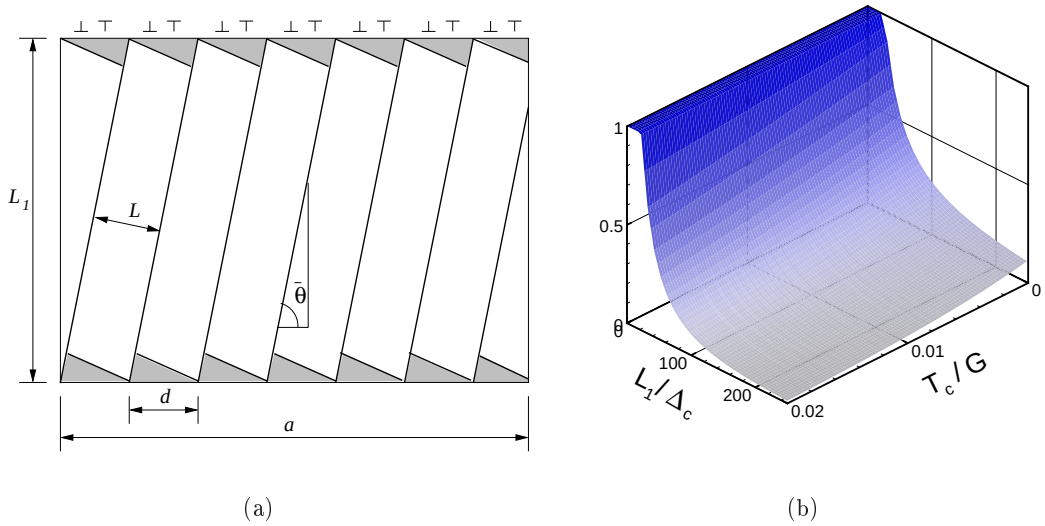

(a) (b)

Figure 5.3: a) Dislocation model used to estimate the misfit energy. b) Plot of the optimum L as function of T_c/G and L_1/Δ_c for the piecewise-linear cohesive law. In the plot we take $L_0 = 10\ \Delta_c$.

addition of a singular perturbation to the energy functional. By virtue of this addition, the scale of the microstructure is no longer arbitrary but results from the balancing of the (already treated) nonconvexity of the energy functional and the (newly included) scale-dependent nonlocal term. In this manner, the addition of the higher-order term to the energy furnishes a selection mechanism among all possible microstructures leading to the relaxed energy. Whereas the relaxation of the local problem effectively describes the qualitative behavior of the full model, the nonlocal extension is both more tractable numerically as well as more predictive, since the degeneracy of the local model is largely eliminated and the predicted microstructures possess a well-characterized finite size.

In order to estimate the misfit energy, and subsequently compute the resulting optimal spacing between faults, we model the boundary layer as an array of dislocations of alternating sign, Fig. 5.3. The Burgers vector of the misfit dislocations is of the order of $|\mathbf{\Delta}|$. This suggests the model misfit energy density

$$E^{\text{mis}}(\mathbf{\Delta}, L) = C\frac{|\mathbf{\Delta}|^2}{L_1}\frac{1}{L}\log\frac{L}{L_0} \tag{5.45}$$

where C is a constant elastic modulus, L_1 the size of the confining container and L_0 plays the role of a 'core cut off'. Accounting for the misfit energy, the total free-energy

density of the faulted region becomes

$$\begin{aligned} &A(\boldsymbol{F}_{n+1}, \boldsymbol{\Delta}_{n+1}, q_{n+1}, L_{n+1}) = \\ &W^e(\boldsymbol{F}^e_{n+1}, L_{n+1}) + \frac{1}{L_{n+1}}\Phi(\boldsymbol{\Delta}_{n+1}, \boldsymbol{q}_{n+1}) + E^{\text{mis}}(\boldsymbol{\Delta}_{n+1}, L_{n+1}) \end{aligned} \tag{5.46}$$

The variational update (5.28) now becomes

$$W_n(\boldsymbol{F}_{n+1}) = \inf_{\substack{\boldsymbol{\Delta}_{n+1}, q_{n+1}, L_{n+1} \\ \boldsymbol{\Delta}_{n+1} \cdot \boldsymbol{N} \geq 0 \\ q_{n+1} \geq q_n}} A(\boldsymbol{F}_{n+1}, \boldsymbol{\Delta}_{n+1}, q_{n+1}, L_{n+1}) \tag{5.47}$$

It is clear from the form of the free energy (5.46) and, in particular, of the misfit energy (5.45) that the optimal fault separation is determined by two competing demands. On one hand, the cohesive energy favors a large value of L resulting in fewer faults per unit volume. On the other hand, the misfit energy favors a small value of L resulting in a narrow boundary layer. Minimization with respect to L_{n+1} gives the equation

$$\frac{1}{L^2}\left(\frac{\partial\Phi}{\partial\Delta_K}\Delta_K - \Phi + \frac{C|\boldsymbol{\Delta}|^2}{L_1} - \frac{C|\boldsymbol{\Delta}|^2}{L_1}\log\frac{L}{L_0}\right) = 0 \tag{5.48}$$

whence we find

$$L = L_0 \exp\left[1 - \frac{L_1}{C}\Gamma(\boldsymbol{\Delta})\right] \tag{5.49}$$

where

$$\Gamma(\boldsymbol{\Delta}) = \frac{1}{|\boldsymbol{\Delta}|^2}\left[\Phi(\boldsymbol{\Delta}) - \frac{\partial\Phi}{\partial\Delta_K}\Delta_K\right] \tag{5.50}$$

For the EOD model with a linearly decreasing monotonic envelop we obtain the particularly simple result

$$\Gamma(\boldsymbol{\Delta}) = \frac{T_c}{2\Delta_c} = \text{constant} \tag{5.51}$$

and the corresponding fault separation follows explicitly as

$$L = L_0 \exp\left[1 - \frac{L_1}{C}\frac{T_c}{2\Delta_c}\right] \tag{5.52}$$

independently of the opening displacement $\boldsymbol{\Delta}$. Thus, in this model the separation between the faults is set at the inception of the faults and conveniently remains constant thereafter. The resulting dependence of L/L_1 on the parameters T_c/G and L_1/Δ_c is

shown in Fig. 5.3b, where G is the shear modulus, and we take $L_0 = 10\ \Delta_c$. As expected, L decreases with increasing cohesive strength T_c and critical opening displacement Δ_c, since an increase in these parameters implies a corresponding increase in the specific cohesive energy of the material.

5.2.6 Frictional stage

Internal *friction* is an important dissipation mechanism in brittle materials, especially in geological applications, applications to structural ceramics, and others. We shall therefore assume that friction operates at the faults *concurrently* with cohesion. However, if the faults loose cohesion completely, e. g., upon the attainment of a critical opening displacement, friction may become the sole dissipation mechanism at the faults.

In considering friction, we wish to retain the variational structure of the model. In particular, we wish to define an incremental strain energy density $W_n(\boldsymbol{F}_{n+1})$ with the property that it be a potential for the stresses through relation (5.29). To this end, we follow Pandolfi *et al.* [139] and define the extended update

$$W_n(\boldsymbol{F}_{n+1}) = \inf_{\substack{\boldsymbol{\Delta}_{n+1},\, q_{n+1} \\ \boldsymbol{\Delta}_{n+1}\cdot\boldsymbol{N}\geq 0 \\ q_{n+1}\geq q_n}} A(\boldsymbol{F}_{n+1},\boldsymbol{\Delta}_{n+1},q_{n+1}) + \frac{\Delta t}{L}\,\psi^*\left(\frac{\boldsymbol{\Delta}_{n+1}-\boldsymbol{\Delta}_n}{\Delta t};\boldsymbol{F}_{n+1},\boldsymbol{\Delta}_{n+1},q_{n+1}\right) \tag{5.53}$$

where for simplicity we consider the case of $L =$ constant. In (5.53) $\psi^*(\dot{\boldsymbol{\Delta}};\boldsymbol{F},\boldsymbol{\Delta},q)$ is a dual kinetic potential per unit area with the following properties:

i) $\psi^* = 0$ if the contact traction $\lambda_1 = 0$, cf eq. (5.30c), i. e., if the faults undergo opening.

ii) If $\lambda_1 < 0$, cf eq. (5.30c), i. e., if the faults are closed, then $\psi^*(\,\cdot\,;\boldsymbol{F},\boldsymbol{\Delta},q)$ is convex and is minimized at $\dot{\boldsymbol{\Delta}} = \boldsymbol{0}$.

We note that during closure, $\lambda_1 < 0$, the contact constraint $\boldsymbol{\Delta}\cdot\boldsymbol{N} = 0$ is active and only the *sliding* opening displacements are nonzero. Hence, frictional dissipation is always associated with fault sliding, as required. We also note that, upon multiplication by

$\boldsymbol{N}$, the equilibrium equation (5.30a) gives the contact traction in the form

$$\lambda_1 = \frac{1}{L}\left(\boldsymbol{N}\cdot S^e\boldsymbol{N} - \frac{\partial\Phi}{\partial\boldsymbol{\Delta}}\cdot\boldsymbol{N}\right) \tag{5.54}$$

Thus, condition (i) can be restated as the requirement that $\psi^* = 0$ if the right hand side of (5.54) vanishes. In the presence of friction, the traction equilibrium equation (5.30a) becomes

$$\frac{1}{L}\left[-S^e_{IJ}N_J + \frac{\partial\Phi}{\partial\Delta_I} + \partial_{\dot{\boldsymbol{\Delta}}}\psi^*\left(\frac{\boldsymbol{\Delta}-\boldsymbol{\Delta}_n}{\Delta t};\boldsymbol{F},\boldsymbol{\Delta},q\right)\right] + \lambda_1 N_I = O(\Delta t) \tag{5.55}$$

where the terms of order $O(\Delta t)$ arise from the dependence of ψ^* on the state variables $(\boldsymbol{F},\boldsymbol{\Delta},q)$. As expected, the frictional forces contribute to the equilibrium of tangential tractions at the faults. It is evident from (5.55) that the update (5.53) is consistent with the frictional rate equations up to admissible truncation errors of order $O(\Delta t)$.

In calculations we assume Coulomb friction and set

$$\psi^*(\dot{\boldsymbol{\Delta}};\boldsymbol{F},\boldsymbol{\Delta},q) = \mu\max\left\{0,\ \frac{\partial\Phi}{\partial\boldsymbol{\Delta}}\cdot\boldsymbol{N} - \boldsymbol{N}\cdot S^e\boldsymbol{N}\right\}|\dot{\boldsymbol{\Delta}}| \tag{5.56}$$

where μ is the coefficient of friction. We note that this choice of dual dissipation potential satisfies conditions (i) and (ii), as required. As befits Coulomb friction, the kinetic potential (5.56) is rate-independent, i. e., is positively homogeneous of degree 1 in $\dot{\boldsymbol{\Delta}}$, and proportional to the contact pressure. We also note that for the EOD model $\partial_{\boldsymbol{\Delta}}\Phi\cdot\boldsymbol{N} = 0$ if $\boldsymbol{\Delta}\cdot\boldsymbol{N} = 0$ and (5.56) simplifies to

$$\psi^*(\dot{\boldsymbol{\Delta}};\boldsymbol{F},\boldsymbol{\Delta},q) = \mu\max\{0,\ -\boldsymbol{N}\cdot S^e\boldsymbol{N}\}\ |\dot{\boldsymbol{\Delta}}| \tag{5.57}$$

It should be carefully noted that the variational formulation (5.53) of fault friction, and the more general one of Pandolfi *et al.* [139], is non-standard in that it results in an incremental minimization problem. In particular, the tangent stiffness corresponding to the incremental equilibrium problem is symmetric, contrary to what is generally expected of *non-associative* materials. The difference between a direct, or non-symmetric, and a variational update for these materials resides in the $O(\Delta t)$ terms in eq. (5.55). Thus, these terms ensure the variational structure of the update without affecting its consistency. In particular, as already mentioned, the variational update defines an incremental strain-energy density $W_n(\boldsymbol{F}_{n+1})$ with the fundamental property (5.29), as desired.

5.2.7 Recursive faulting

So far we have consider either an intact material or a single family of parallel faults. We shall refer to the latter microstructure as a *rank*-1 faulting pattern. More complex microstructures, which we name *recursive faulting patterns*, can effectively be generated by applying the rank-1 construction *recursively*. In the first level of recursion, in (5.8) and (5.28) we simply replace the elastic strain-energy density $W(\boldsymbol{F}^e)$ of the matrix by $W_n(\boldsymbol{F}^e)$, i. e., by the effective strain-energy density of a rank-1 faulting pattern. This substitution can now be iterated, resulting in a recursive definition of $W_n(\boldsymbol{F}_{n+1})$. The recursion stops when $W_n(\boldsymbol{F}^e) = W(\boldsymbol{F}^e)$, i. e., when intervening matrix between the faults remains elastic. The resulting microstructures are shown in Fig. 5.1a, and consist of *faults within faults*. The level of recursion is the *rank* of the microstructure.

As noted in the introduction, recursive faulting is similar in spirit to the sequential-lamination constructions used to relax non-convex energies arising in other areas of application (cf, e. g., [47, 118] and references therein). In particular, as in laminates the different levels of faulting are only approximately compatible. However, recursive faulting differs from sequential lamination crucially in that the state of stress within each level of faulting is uniform, and therefore automatically in equilibrium. The implication of this property is that the recursive faulting construction can be implemented simply by means of a recursive call to the rank-1 faulting construction. Conveniently, many programming languages such as C or C++ support recursive function calls. This greatly facilitates the implementation of the model, which is reduced to the implementation of the rank-1 faulting construction. This is in sharp contrast to laminates, which must be equilibrated globally at considerable computational cost and complexity of implementation (cf [135, 7]).

5.3 Relaxation of the faulting model

Next we turn to the boundary value problem of a solid undergoing recursive faulting such as described in the foregoing and proceed to analyze its properties. In order to simplify the analysis we work within a *deformation theory* framework, namely, we consider the incremental strain-energy density $W(\boldsymbol{F})$ that results from applying the entire deformation $\boldsymbol{F}$ to an intact body in one step. Alternatively, this simplification may be regarded as the study of the first time step in the time-discretized framework discussed in Section 5.2.3.

We shall be specifically interested in situations where the size of the body is much

larger than the spacing L of the faults, i. e., in the limiting behavior as $L \to 0$. We focus our attention on the local model introduced in Sections 5.2.1 and 5.2.2 and neglect the lengthscale-dependent corrections discussed in Section 5.2.5. In addition, for every material point we consider faults with one single orientation. In a crystal plasticity framework this constraint corresponds to the assumption of infinite latent hardening (cf, e. g., [134, 40]). The relaxation of the model then gives mixtures of faults of different orientations, which furnishes mathematical justification to the recursive faulting construction discussed in Section 5.2.7. Since we are primarily interested in the macroscopic behavior of the material, our analysis contemplates, locally, a continuous distribution of faults (with a single orientation) from the outset. Including discrete sharp faults, e. g., within a BV (space of functions of bounded variation) framework, results in the same relaxation of the energy, albeit at the expense of technical difficulties arising from a lack of sufficient coercivity to ensure compactness. For general tools for the relaxation of functionals defined on BV see, e. g., [23].

Suppose that we wish to determine the stable configurations of the body. To this end, we introduce the potential energy

$$I(\boldsymbol{u}) = \int_\Omega W(\nabla \boldsymbol{u})\, dV - G(\boldsymbol{u}) \equiv F(\boldsymbol{u}) - G(\boldsymbol{u}) \tag{5.58}$$

where Ω is the domain of analysis; $\boldsymbol{u}$ is the displacement field; dV is the element of volume; and $G(\boldsymbol{u})$ is a loading term, e. g.,

$$G(\boldsymbol{u}) = \int_\Omega \rho \boldsymbol{B} \cdot \boldsymbol{u}\, dV + \int_{\partial\Omega_2} \bar{\boldsymbol{T}} \cdot \boldsymbol{u}\, dS \tag{5.59}$$

where $\rho\boldsymbol{B}$ is a body-force density per unit undeformed volume; $\bar{\boldsymbol{T}}$ are applied tractions per unit undeformed area; $\partial\Omega_2$ is the traction boundary; and dS is the corresponding element of area. We identify the stable configurations of the body with the configurations of minimum potential energy. In this manner we are led to the minimum problem

$$\inf_{\boldsymbol{u}\in X} I(\boldsymbol{u}) \tag{5.60}$$

where X is the configurational space of the body. For instance, an appropriate configuration space is $X = \{\boldsymbol{u} \in W^{1,\infty}(\Omega),\ \boldsymbol{u} = \bar{\boldsymbol{u}} \text{ on } \partial\Omega_1\}$, where $W^{1,\infty}(\Omega)$ is the space of Lipschitz continuous functions; $\partial\Omega_1 = \partial\Omega - \partial\Omega_2$ is the displacement boundary; and $\bar{\boldsymbol{u}}$ is a prescribed boundary displacement function over $\partial\Omega_1$.

We begin by considering the limiting case of frictionless sliding. In this limit, and

for a single level of faulting, the strain energy density can be expressed in the form:

$$W(\boldsymbol{F}) = \inf\{W^e(\boldsymbol{F}^e) + W^p(\boldsymbol{F}^p) : \boldsymbol{F} = \boldsymbol{F}^e\boldsymbol{F}^p\} \tag{5.61}$$

where

$$W^p(\boldsymbol{F}^p) = \begin{cases} f(|\boldsymbol{a}\cdot\boldsymbol{b}|, |\boldsymbol{a}\times\boldsymbol{b}|) & \text{if } \boldsymbol{F}^p = \boldsymbol{I} + \boldsymbol{a}\otimes\boldsymbol{b}\,, \quad \boldsymbol{a}\cdot\boldsymbol{b} \geq 0\,, \\ \infty & \text{otherwise.} \end{cases} \tag{5.62}$$

The elastic energy satisfies

$$W^e(\boldsymbol{F}) = \infty, \text{ if } \det\boldsymbol{F} \leq 0\,, \tag{5.63a}$$

$$W^e(\boldsymbol{F}) < \infty, \text{ if } \det\boldsymbol{F} > 0\,, \tag{5.63b}$$

and is continuous on the set $\{\boldsymbol{F} : \det\boldsymbol{F} > 0\}$. In addition, the function f is continuous, nonnegative, vanishes at the origin and has sublinear growth, in the sense that

$$\lim_{t\to\infty} \frac{f(t\boldsymbol{x})}{|t|} = 0\,, \tag{5.64}$$

for all $\boldsymbol{x} \in \mathbb{R}^2$.

The cohesive energy (5.62) restricts the local fault geometry to be of rank-one, i. e., permits faulting in one direction only at every material point, in analogy to (5.3). Since, in the spirit of relaxation, we are interested in the limit of infinite microstructural refinement, $L \to 0$, we proceed to adapt our notation to this limit. In particular, henceforth we work with the opening-displacement density per unit volume, instead of the opening displacement per fault, which effectively eliminates L in the definition of the variables. Specifically, we use $\boldsymbol{b}$–instead of $\boldsymbol{N}$–to denote the normal to the faulting plane; $\boldsymbol{a}$–instead of $\boldsymbol{\Delta}/L$–to denote the average opening displacement; and we replace the cohesive energy Φ/L by a more general energy density W^p per unit volume which depends, through a sublinear function f, on both the normal and transverse opening displacements, $\boldsymbol{a}\cdot\boldsymbol{b}$ and $|\boldsymbol{a}\times\boldsymbol{b}|$, respectively. These adjustments both streamline as well as add generality to the analysis.

The preceding form of the energy density affords a number of revealing analogies to other models. Thus, within a variational framework of plasticity [136], (5.61) and (5.62) are in analogy to Tresca models of plasticity, in which yielding is assumed to occur instantaneously on a single–but otherwise arbitrary–slip system. However, an

important difference between the present model and Tresca plasticity is that the faults are allowed to open in addition to sliding. Thus, in (5.62) the faulting model requires that $\boldsymbol{a} \cdot \boldsymbol{b} \geq 0$, whereas Tresca plasticity requires that $\boldsymbol{a} \cdot \boldsymbol{b} = 0$, corresponding to a deformation of pure slip. These differences notwithstanding, within the analogy to variational plasticity the assumption (5.64) of sublinear growth corresponds to an assumption of *strain softening*. On the strength of this analogy, we expect the static problem (5.60) to be highly degenerate. In particular, we expect the material to lose its bearing capacity in shear under conditions of all-around confinement; and to have no resistance to tensile fracture, or toughness. This latter property makes local softening models poor models of tensile fracture in general.

These expectations are rigorously born out by an investigation of the *relaxation* of the potential energy functional $I(\boldsymbol{u})$. This functional is not lower semicontinuous, and minimizing sequences form fine-scale oscillations. The aim then is to obtain the relaxation $J(\boldsymbol{u})$ of $I(\boldsymbol{u})$, which describes the macroscopic material behavior averaged over such fine scale structures. We recall that $J(\boldsymbol{u})$ is characterized by the two properties

1. *Lower bound.* For each sequence $\boldsymbol{u}_h$ converging to $\boldsymbol{u}$,

$$J(\boldsymbol{u}) \leq \liminf_{h\to\infty} I(\boldsymbol{u}_h)$$

2. *Recovery sequence.* For every $\boldsymbol{u}$ there is a sequence $\boldsymbol{u}_h$ converging to $\boldsymbol{u}$ such that

$$J(\boldsymbol{u}) = \lim_{h\to\infty} I(\boldsymbol{u}_h)\,.$$

Here convergence is understood in the sense of the weak-$W^{1,\infty}$ topology, i. e., we say that the sequence $\boldsymbol{u}_h$ converges to $\boldsymbol{u}$ if $\{\boldsymbol{u}_h\}$ is uniformly Lipschitz and $\boldsymbol{u}_h$ converges uniformly to $\boldsymbol{u}$. Standard theory shows that, if W is continuous,

$$J(\boldsymbol{u}) = \int_\Omega W^{\mathrm{qc}}(\nabla \boldsymbol{u}) dV - G(\boldsymbol{u}) \tag{5.65}$$

where

$$W^{\mathrm{qc}}(\boldsymbol{F}) = \inf_{\boldsymbol{v}\in W_0^{1,\infty}(E)} \frac{1}{|E|} \int_E W(F + \nabla \boldsymbol{v}) dV \tag{5.66}$$

is the *quasi-convex* envelope of W. Here $E \subset \mathbb{R}^3$ is any open bounded set, and $W_0^{1,\infty}(E)$ is the space of Lipschitz continuous functions which vanish on the boundary ∂E. A scaling and covering argument shows that the definition of $W^{\mathrm{qc}}(\boldsymbol{F})$ does not depend

on the choice of the domain E.

Standard theory also provides a compelling connection between the minimizers of $J(\boldsymbol{u})$ and $I(\boldsymbol{u})$. In particular, $\inf_{\boldsymbol{u}\in X} I(\boldsymbol{u}) = \inf_{\boldsymbol{u}\in X} J(\boldsymbol{u})$ and every cluster point of a minimizing sequence of $I(\boldsymbol{u})$ is a minimum point of $J(\boldsymbol{u})$. Conversely, every minimum point of $J(\boldsymbol{u})$ is the limit of a minimizing sequence of $I(\boldsymbol{u})$ in X. The relaxed functional $J(\boldsymbol{u})$ is always lower semi-continuous. If $I(\boldsymbol{u})$ is coercive, then $J(\boldsymbol{u})$ is also coercive and, hence, has a minimum point in X. These properties of relaxation show that the functional $I(\boldsymbol{u})$ can be replaced by the better-behaved functional $J(\boldsymbol{u})$ without essential loss of information. The minimizing sequences of $I(\boldsymbol{u})$ then correspond to *microstructures* and minimizers of $J(\boldsymbol{u})$ characterize their average properties. For a precise exposition of these and related concepts, see e. g., [47, Sect. 5.2] and [118, Sect. 4].

In the present setting, the functional $I(\boldsymbol{u})$ is not coercive and, therefore, existence cannot be guaranteed in general even for the relaxed functional. This degeneracy, which is illustrated by the examples after Proposition 1, owes to the lack of macroscopic resistance to tension and slip (cf also the discussion below). Further, since the energy density W under consideration incorporates a positive-determinant constraint the general results that link the relaxed functional to the quasiconvex envelope W^{qc} hold for C^1 displacement fields $\boldsymbol{u}$ only.

Our main result is a characterization of the quasiconvex envelope of W.

Proposition 1. *The quasiconvex envelope of W, defined in (5.61-5.64), is:*

$$W^{\mathrm{qc}}(\boldsymbol{F}) = \varphi^{**}(\det \boldsymbol{F}) \tag{5.67}$$

where φ^{**} is the convex envelope of the function

$$\varphi(t) = \inf\left\{W^e(\boldsymbol{F}^e) : \ \det \boldsymbol{F}^e \leq t\right\} . \tag{5.68}$$

The proof of this proposition is given in the appendix. To illustrate the significance of this result, we provide two explicit examples.

Example 1: Suppose that $W^e(\boldsymbol{F}) = \mathrm{dist}^2(\boldsymbol{F}, SO(3)) + \psi(\det \boldsymbol{F})$ for some convex nonnegative ψ with $\psi(1) = 0$ and $\psi(t) = \infty$ for $t < 0$. Since

$$\mathrm{dist}^2(\boldsymbol{F}, SO(3)) = \sum_{i=1}^{3} (\lambda_i(\boldsymbol{F}) - 1)^2 , \tag{5.69}$$

where $\lambda_i(\boldsymbol{F})$ are the singular values of $\boldsymbol{F}$, we get

$$\inf\{W^e(\boldsymbol{F}):\ \det\boldsymbol{F}=t\}=3(t^{1/3}-1)^2+\psi(t)\,. \tag{5.70}$$

Then it follows that

$$\varphi^{**}(t)=\varphi(t)=\begin{cases}\infty & \text{if } t<0\\ 3(t^{1/3}-1)^2+\psi(t) & \text{if } 0\le t<1\\ 0 & \text{if } t\ge 1\,.\end{cases} \tag{5.71}$$

□

Example 2: Let $W^e(\boldsymbol{F})=W^{\rm dev}(\boldsymbol{F}^{\rm dev})+\psi(\det\boldsymbol{F})$, with ψ as above, $\boldsymbol{F}^{\rm dev}\equiv(\det\boldsymbol{F})^{-1/3}\boldsymbol{F}$, $W^{\rm dev}$ nonnegative and $W^{\rm dev}(\boldsymbol{I})=0$. Then

$$\inf\left\{W^{\rm dev}(\boldsymbol{F}^{\rm dev}):\ \det\boldsymbol{F}=t\right\}=0 \tag{5.72}$$

for any $t\neq 0$, e. g., by choosing $\boldsymbol{F}=t^{1/3}\boldsymbol{I}$. Therefore

$$\varphi(t)=\inf\{\psi(s):\ s\le t\}\ , \tag{5.73}$$

and, consequently,

$$\varphi^{**}(t)=\varphi(t)=\begin{cases}\infty & \text{if } t<0\\ \psi(t) & \text{if } 0\le t<1\\ 0 & \text{if } t\ge 1\,.\end{cases} \tag{5.74}$$

□

Proposition 1 can be readily extended to polycrystals. To this end, suppose that the domain Ω is subdivided into countably many Lipschitz subsets ω_i with an orientation $\boldsymbol{Q}_i\in SO(3)$ ascribed to each subset. The corresponding strain energy is

$$I(\boldsymbol{u})=\sum_i\int_{\omega_i}W(\nabla\boldsymbol{u}\boldsymbol{Q}_i)dV \tag{5.75}$$

Then, an application of Proposition 1 to each grain yields the following result.

Corollary 1. *The relaxation of $I(\boldsymbol{u})$, eq. (5.75), is given on maps $\boldsymbol{u}\in C^1(\Omega,\mathbb{R}^3)$ by the isotropic functional*

$$J(\boldsymbol{u})=\int_\Omega W^{\rm qc}(\nabla\boldsymbol{u})dV\,. \tag{5.76}$$

The preceding results shed considerable light into the properties of the quasistatic problem (5.60) defined by the local and frictionless recursive faulting model. Thus, proposition 1 and the subsequent examples show that, for a broad range of commonly assumed elastic energy densities, the effective behavior of the material falls into two well-differentiated regimes: the *compressive regime*, $\det \boldsymbol{F} < 1$, corresponding to strong all-around confinement; and the *tensile regime*, $\det \boldsymbol{F} > 1$, characterized by the presence of directions of large tensile deformation. In the compressive regime, the material retains is volumetric load-bearing capacity but loses its shear load-bearing capacity completely. In the tensile regime, the material disintegrates completely. It is interesting to note that, as shown in the appendix, recursive faulting does indeed provide a class of minimizing sequences that delivers the relaxation of the material, which justifies the recursive faulting construction described in Section 5.2.7.

In practice there are several sources of regularizaton that prevent the attainment of the degenerate limit just described. Firstly, relaxation represents a highly idealized limit that is attained only if the material is capable of exploring all possible microstructures. A more common type of physical behavior is *metastability*, in which the system falls in local minima instead of attaining the infimum of the energy. Other common sources of regularization are viscosity and dynamics [70, 151]. In the present context the role of viscosity, albeit rate-independent, is played by friction. In this case, the sublinear growth (5.64) is replaced by linear growth and the material no longer exhibits softening. The relaxation of the resulting energy is beyond the scope of this paper, but may be expected to be similar to that of other models having linear growth, including single-crystal plasticity [40]. Finally, in a time-discretized framework the effect of inertia is to add an L^2-continuous quadratic positive-definite term to the incremental energy functional [70, 151]. The resulting stabilizing effect of inertia in otherwise non-convex problems has been investigated by Dolzmann and Friesecke [70] and Demoulini [59]. However, even allowing for metastability and frictional and dynamical regularization the relaxation result of proposition 1 does provide useful information about the general trends in the expected macroscopic behavior, such as the existence of well-differentiated compressive and tensile regimes.

5.4 Validation examples

As an example of application of the recursive faulting model, and by way of validation, we proceed to simulate the dynamic multi-axial compression experiments on

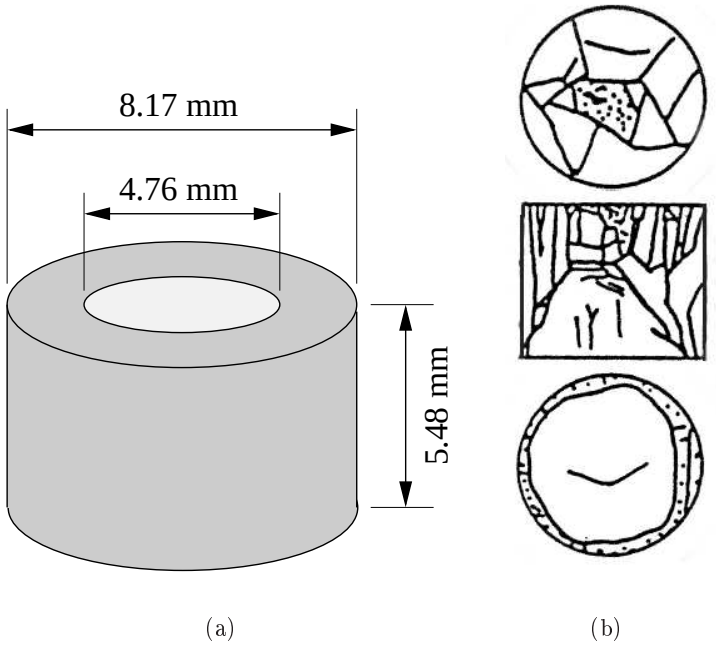

Figure 5.4: (a) Geometry of the sleeved specimen used in the experiments of Chen and Ravichandran [34, 36]. Internal diameter 4.76 mm, external diameter 8.17 mm, height 5.48 mm. (b) Schematic of the damage patterns in the confined specimen at the end of the experiment (Fig. 8 in [34]), from top to bottom: top view, vertical cross section, and bottom view.

sintered aluminum nitride (AlN) of Chen and Ravichandran [33, 34, 35, 36]. Chen and Ravichandran's experimental technique is designed for imposing controlled lateral confinement on specimens subjected to dynamic uniaxial compression [33, 35]. In Chen and Ravichandran's experiments, an axial compression is applied by a split Hopkinson pressure bar modified to subject the specimen to a single loading pulse during the experiment. The specimen is confined laterally by a shrink-fit metal sleeve, Fig. 5.4a. We specifically focus on Chen and Ravichandran's data for for aluminum nitride (AlN) [34, 36]. The experiments provide a wealth of validation data, including loading histories, the axial stress-strain curves, as well as detailed crack patterns in the confined specimen, Fig. 5.4b. The data show that failure occurs by fragmentation due to axial splitting under uniaxial stress conditions; and by localized shear deformation under moderate lateral confinement. The compressive failure strength of ceramic materials increases with increasing confinement pressure. It is also observed that the propensity for ceramics to fragment is suppressed by lateral confinement. Furthermore, ceramics exhibit some inelasticity in the stress-strain behavior in the presence of lateral confinement.

The material properties of AlN used in the calculations are collected in Table 2. The elastic modulus E, the Poisson coefficient ν and the mass density ρ are reported in [34]. The tensile strength T_c is chose in the middle of the experimental range of 155-214 MPa characteristic of structural ceramics [207]. The coupling parameter β is estimated from the difference between tensile and compressive strengths of the material. The critical opening displacement Δ_c is estimated from static data. From the top view of the observed damage pattern, Fig. 5.4b, the distribution of rank-1 faults is assumed to be coarse and, in consequence, the fault separation L is taken to be one half of the specimen diameter.

E (GPa)	ν	T_c (MPa)	Δ_c (μm)	β	L (mm)	μ	ρ (kg/m^3)
310	0.237	180	1.8	3.464	2.38	0.25	3200

Table 2. AlN material constants adopted in the calculation.

The AlN specimen under consideration is 4.76 mm in diameter and 5.48 mm in length, Fig. 5.4a. The outer diameter of the sleeve is 8.17 mm, and the inner diameter is 0.025 mm less than the specimen diameter. The specimen is loaded by imposing the experimentally recorded velocity profile (Fig. 4, [34]) on the side of the incident bar. For

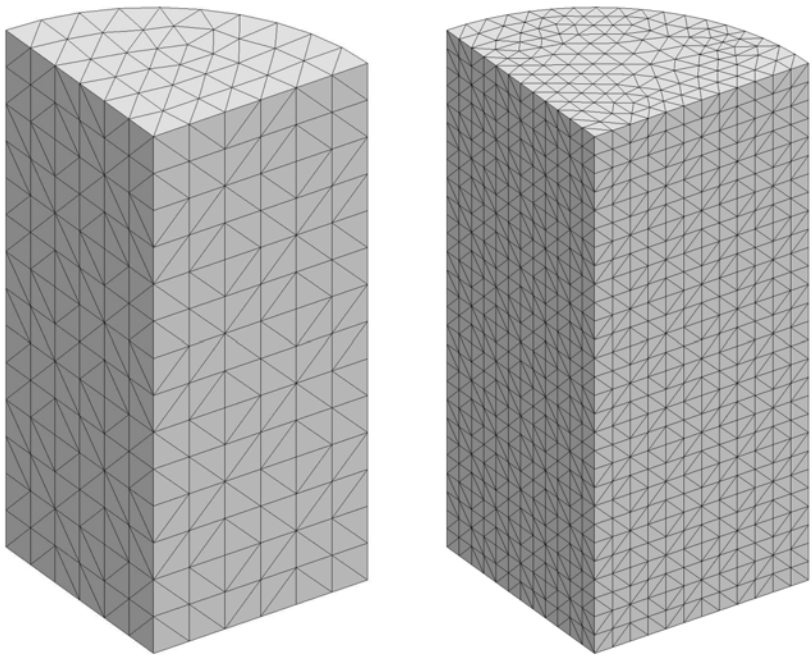

(a) (b)

Figure 5.5: Finite element meshes used in the calculations (a) Coarse 217-elements mesh; and (b) fine 2004-elements mesh.

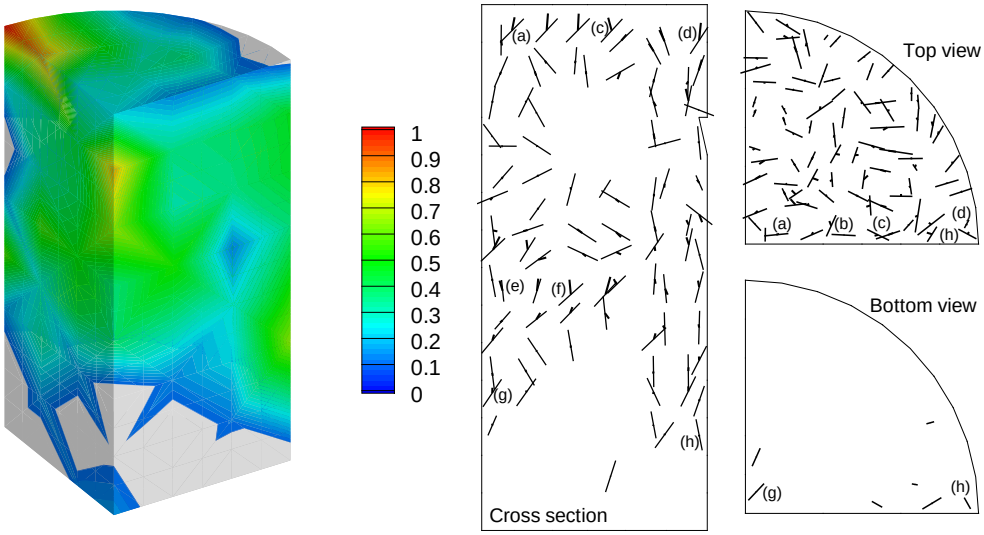

(a) (b)

Figure 5.6: Numerical simulation of the confined specimen allowing for rank-1 faulting only. a) Computed contour levels of damage in rank-1 faulting calculations. The damage variable ranges from 0 to 1 and represents the fraction of specific fracture energy expended by the material. b) Cross section, top view and bottom view of the fault distribution. The lines represent the fault planes and the arrows the opening displacement vector. The fault structures labelled (a)-(h) are shown in Fig. 5.7.

simplicity, we consider the limiting cases of and unconfined specimen, corresponding to a traction-free lateral surface; and rigid confinement, corresponding to constraining the radial displacement of the lateral surface. Owing to the symmetry of the problem we may model one fourth of the specimen only. In order to investigate matters of mesh-size dependency we consider two meshes: a course mesh consisting of 217 10-node tetrahedral finite elements (504 nodes); and a second finer mesh consisting of 2004 10-node tetrahedra and 3428 nodes. The geometry of the sleeve-core assembly and the two meshes used in the simulations are shown in Fig. 5.4a and 5.5, respectively.

The results of a first set of simulations of the confined case obtained by allowing rank-1 faulting only are shown in Figs. 5.6, 5.7 and 5.8. Fig. 5.6 shows the general distribution of damage at the end of the simulation of the confined case. Damage is represented by means of a damage parameter defined as the ratio between the energy expended in fracture and the specific fracture energy of the material. By virtue of this definition, the damage parameter ranges from 0 for the undamaged material to

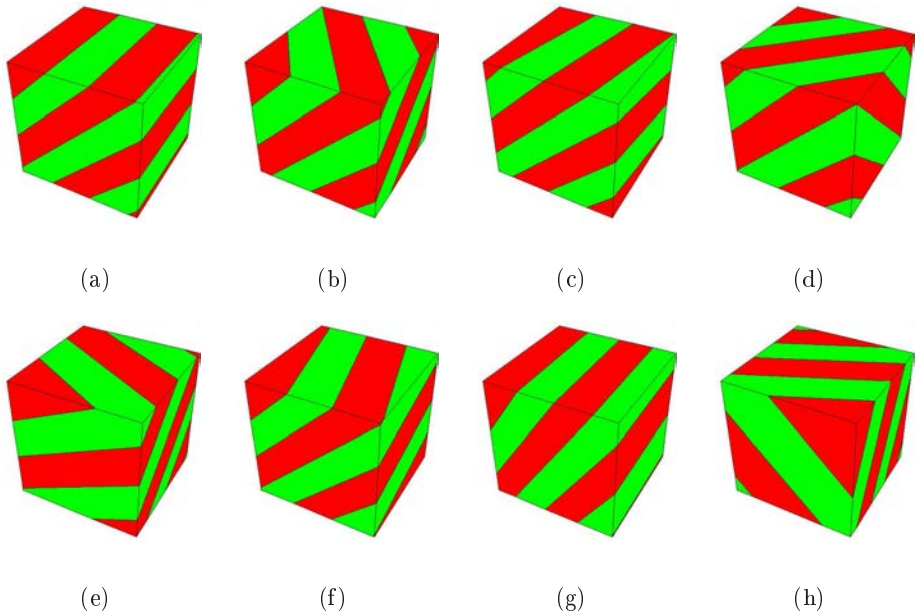

Figure 5.7: Numerical simulation of the confined specimen allowing for rank-1 faulting only. Detailed view of rank-1 fault structures computed at points (a)-(h) of Fig. 5.6b.

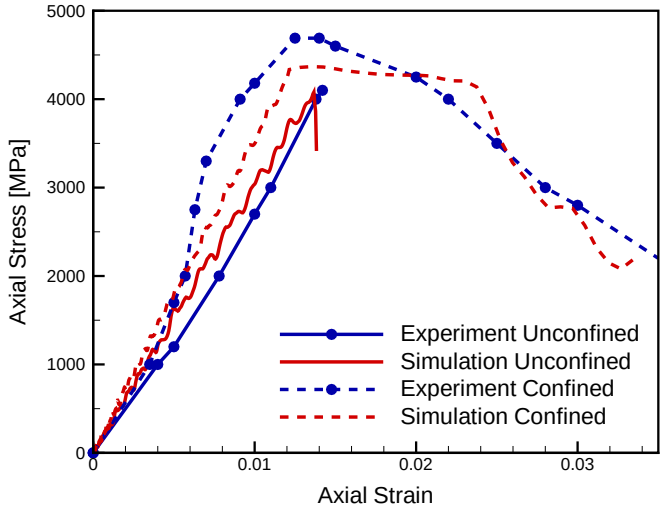

Figure 5.8: Numerical simulation of the confined specimen allowing for rank-1 faulting only. Experimental and predicted axial stress *vs.* axial strain curves.

1 for fully developed cracks in tension or shear. In the confined case the computed distribution of damage exhibits characteristic cone failure and a region of extensive compressive damage, or crushing, under the front surface of the specimen, Fig. 5.6, in general agreement with experiment, Fig. 5.4b. The detailed orientation and activity of the faults is shown in Fig. 5.6b. The rank-1 faulting microstructures that develop at selected material points are shown in Fig. 5.7. The computed faults in the crushing zone tend to align vertically, specially in the periphery of the specimen, but do not exhibit a preferred orientation on cross section of the specimen normal to the axis. These trends are generally consistent with the observed fracture patterns, Fig. 5.4b.

In the simulations of the unconfined case, intense damage occurs over vast regions of the specimen, especially in the vicinity of the posterior surface. Deformation trapping at the boundary is known to occur in one-dimensional wave propagation through softening materials ([195]). Comparison of fracture patterns with experiment is not possible in this case since the specimen was not recovered.

Fig. 5.8 shows the plots of axial stress *vs.* axial strain for the unconfined and confined cases. The figure also shows the corresponding experimental data for comparison. The sharp contrast between the unconfined and confined cases is immediately apparent in the figure. Thus, in the unconfined case the specimen fails catastrophically upon the attainment of the tensile strength of the material. Subsequent to the failure point, the load-bearing capacity of the specimen drops precipitously. By way of contrast, the confined specimen exhibits quasi-ductile behavior. Indeed, following the point of inception of damage the specimen enters a yielding regime, though it eventually strain-softens and fails. Thus, the addition of confinement alters the behavior of the specimen from perfectly brittle to quasi-ductile, an effect that may be thought of as a *brittle-to-ductile transition*. These predicted general trends are also clearly visible in the experimental curves. The ability of the model to predict the transition from perfectly brittle to quasi-ductile behavior resulting from the addition of confinement is particularly noteworthy.

The results of numerical simulation allowing for rank-3 recursive faulting microstructures are shown in Fig. 5.9, 5.10 and 5.11. Fig. 5.9 shows that rank-1 microstructures are the most common, with rank-2 and rank-3 microstructures arising with diminishing frequency. In addition, complex recursive fault patterns of rank higher than one develop primarily in the vicinity of the anterior surface of the specimen, and become increasingly rare with depth in the axial direction. This concentration of damage may again be regarded as an instance of deformation trapping [195]. The intricate patterns

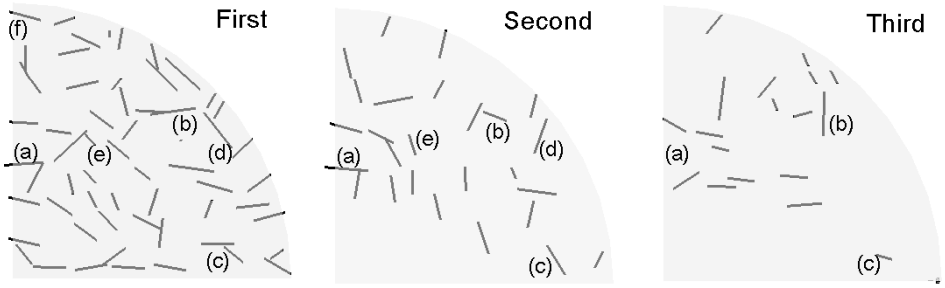

Figure 5.9: Numerical simulation of the confined specimen allowing for rank-3 recursive faulting. Top view of the first, second and third-level fault distribution. Fault structures at points labelled (a)-(f) are shown in Fig. 5.10.

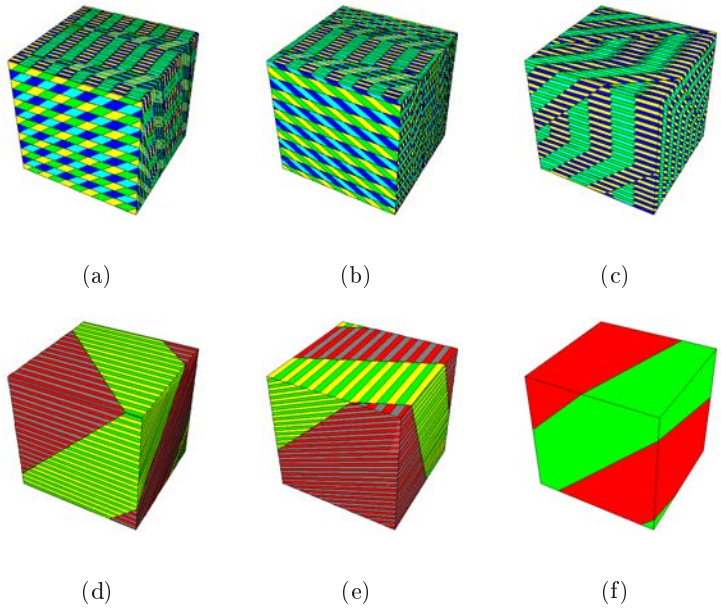

Figure 5.10: Numerical simulation of the confined specimen allowing for rank-3 recursive faulting. Detailed view of recursive faulting structures computed at points (a)-(h) of Fig. 5.9. (a)-(c) Rank-3 microstructures. (d)-(e) Rank-2 microstructures. (f) Rank-1 microstructure.

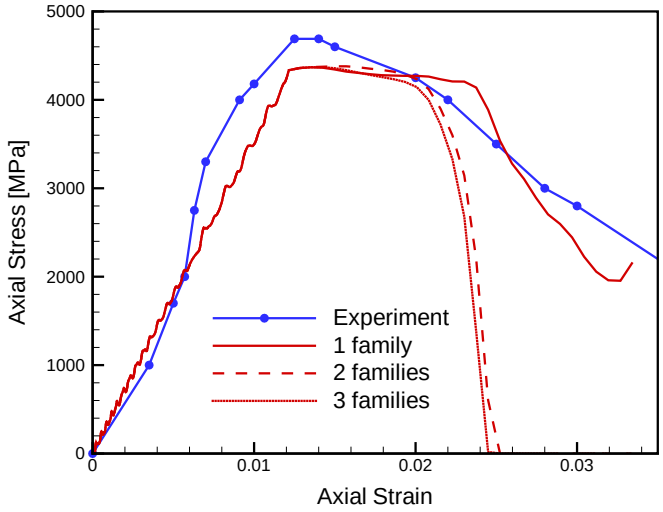

Figure 5.11: Numerical simulation of the confined specimen allowing for rank-3 recursive faulting. Experimental and predicted axial stress *vs.* axial strain curves.

of damage and deformation that correspond to rank-2 and rank-3 microstructures are shown in Fig. 5.10 at selected sampling points. The ability of the model to general complex sub-grid microstructures *on the fly* as part of a macroscopic finite-element calculation is noteworthy. In order to calculate the separations at all levels of faulting, we take the compliance C in (5.52) to be of the order of the shear modulus; and the 'core cut-off' distance L_0 to be of the order of $100\Delta_c$. The resulting fault separations are: 2.38, 0.09 and 0.24 mm, corresponding to levels one, two and three, respectively. The effect of recursive faulting on the macroscopic stress-strain curve is to soften the post-peak response and accelerate failure, Fig. 5.11, partly owing to damage concentration and deformation trapping at the boundary.

Finally, Fig. 5.12 shows a comparison of results corresponding to the coarse and fine meshes depicted in Fig. 5.5. The calculations concern the confined specimen and allow for rank-1 faulting only. The comparison demonstrates the mesh-size independence of the calculations. This mesh-size independence is expected since, under sufficient confinement, damage takes place in a distributed fashion and does not exhibit localization. This diffuse nature of compressive damage in turn owes to the stabilizing effect of inertia and internal friction, as remarked in Section 5.3.

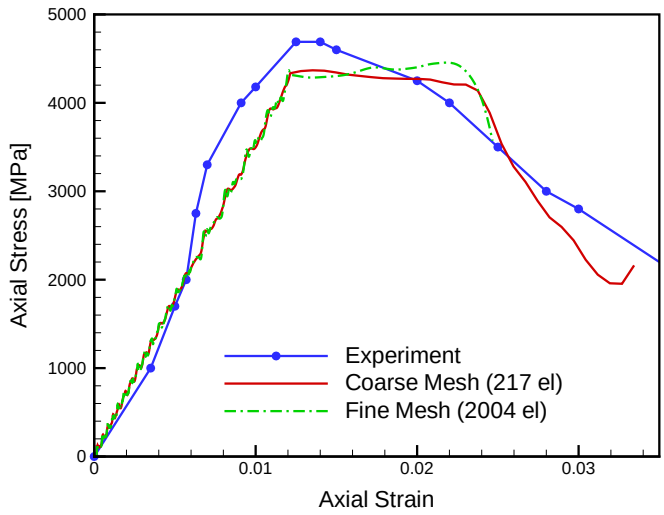

Figure 5.12: Axial stress *vs.* axial strain curves for confined specimens using the meshes shown in Fig. 5.5.

5.5 Summary and concluding remarks

We have developed a model of distributed damage in brittle materials deforming in triaxial compression based on the explicit construction of special microstructures. These microstructures are obtained by *recursive faulting*, i. e., by recursively fitting faults within faults. The model accounts for the elasticity of the matrix, fault nucleation and the cohesive and frictional behavior of the faults. We have also developed a time discretization of the model that confers the incremental problem a variational structure. We resort to this variational structure in order to predict the inception of the faults and their optimal orientation and separation. We also exploit the variational structure of the incremental quasistatic boundary-value problem for purposes of mathematical analysis and determine the relaxation of the potential energy, which describes the macroscopic material behavior averaged over all possible fine-scale structures. This analysis delineates two well-differentiated regimes in the macroscopic behavior of the material: a *compressive regime*, in which the material retains is volumetric load-bearing capacity but tends to lose its shear load-bearing capacity completely; and the *tensile regime*, in which the material tends to disintegrate completely. Finally, we present numerical calculations of the dynamic multi-axial compression experiments on sintered

aluminum nitride (AlN) of Chen and Ravichandran [33, 34, 35, 36]. In this calculations, the microstructure is not resolved by the mesh and is modelled at the sub-grid level. Specifically, the recursive faulting construction is used to generate sub-grid microstructures 'on the fly' as part of a finite-element analysis. In this sense, the approach provides an example of *concurrent multiscale computing*, i. e., of a computational scheme in which two or more length scales are carried simultaneously within the same calculation. The model correctly predicts the general trends regarding the observed damage patterns; and the brittle-to-ductile transition resulting under increasing confinement.

In closing, we point to some of the limitations of the model and related open questions. Firstly, it should be carefully noted that the model makes sense under conditions resulting in diffuse or distributed damage. Our analysis and numerical experiments indicate that these conditions are met in triaxial compression under sufficiently strong confinement, specifically, when $\det(\boldsymbol{F}) < 1$. Under strongly tensile conditions, i. e., when $\det(\boldsymbol{F}) > 1$, localization into a small number of dominant cracks is to be expected and the model ceases to apply. Indeed, damage or softening models are poor models of fracture in general, as they lack a specific fracture energy per unit surface, and a model of discrete fracture is preferable in that regime. We also expect the presence of friction to modify substantially the relaxation of the model. In particular, friction may be expected to confer the material resistance to macroscopic shearing deformation in compression. However, the relaxation of the frictional model is unknown to us at present. Moreover, there is a paucity of mathematical tools for characterizing the macroscopic behavior of solids with microstructure in the presence of inertia. In addition, the question of kinetics of fault nucleation appears to be open at present as well.

Acknowledgements

MO and AP gratefully acknowledge the support of the Department of Energy through Caltech's ASCI ASAP Center for the Simulation of the Dynamic Response of Materials. AP additionally acknowledges the support of the Italian MIUR through the Cofin2003 program "Interfacial damage failure in structural systems: applications to civil engineering and emerging research fields". The work of SC was supported by the Deutsche Forschungsgemeinschaft through the Schwerpunktprogramm 1095 *Analysis, Modeling and Simulation of Multiscale Problems.* This work was partially carried during MO's stay at the Max Planck Institute for Mathematics in the Sciences of Leipzig,

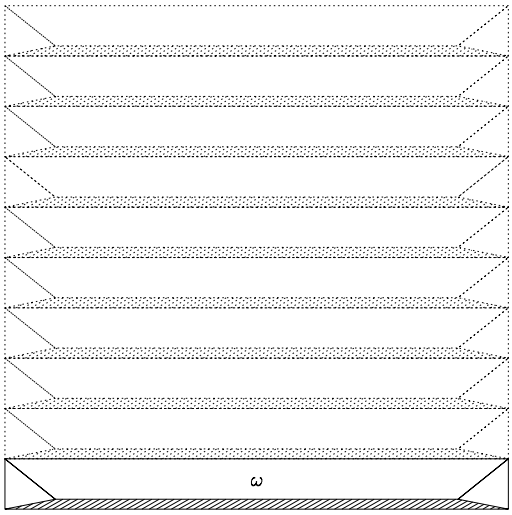

Figure 5.13: Sketch of the construction used to prove (5.77). The dashed area is the set S where the gradient $\boldsymbol{F}_k(\boldsymbol{I}+\varepsilon^{-1}\boldsymbol{a}_k\otimes\boldsymbol{b}_k)$ is used. The dotted parts are copies of R, and indicate the global construction that can be used in the unit square.

Germany, under the auspices of the Humboldt Foundation. MO gratefully acknowledges the financial support provided by the Foundation and the hospitality extended by the Institute.

Appendix: Proof of Proposition 1

We recall that the relaxation extends trivially in the presence of continuous perturbations such as body forces and boundary tractions (e. g., [48, 28]). Since, with the convergence criterion under consideration, $G(\boldsymbol{u})$ in (5.59) is continuous, we may therefore focus on the relaxation of the strain-energy $\boldsymbol{F}(\boldsymbol{u})$. The results thus obtained are immediately applicable to the general boundary value problem which governs the quasistatic deformations of bodies subjected to body forces and displacement boundary conditions on part of $\partial\Omega$.

Proof. We claim that for any $k\in\mathbb{N}$ we have

$$\text{if } \boldsymbol{F}=\boldsymbol{F}^e\prod_{i=1}^{k}(\boldsymbol{I}+\boldsymbol{a}_i\otimes\boldsymbol{b}_i) \text{ with } \boldsymbol{a}_i\cdot\boldsymbol{b}_i\geq 0, \qquad \text{then } W^{\mathrm{qc}}(\boldsymbol{F})\leq W^e(\boldsymbol{F}^e)\,. \tag{5.77}$$

We prove this claim by induction. If $k = 0$ there is nothing to prove. Assume the claim holds for some $k \geq 0$, and consider

$$\boldsymbol{F}_k = \boldsymbol{F}^e \prod_{i=1}^{k} (\boldsymbol{I} + \boldsymbol{a}_i \otimes \boldsymbol{b}_i)\,, \qquad \boldsymbol{F}_{k+1} = \boldsymbol{F}_k(\boldsymbol{I} + \boldsymbol{a}_{k+1} \otimes \boldsymbol{b}_{k+1})\,, \tag{5.78}$$

with all $\boldsymbol{a}_i \cdot \boldsymbol{b}_i \geq 0$. Without loss of generality we can assume $|\boldsymbol{b}_{k+1}| = 1$, and after a rotation $\boldsymbol{b}_{k+1} = \boldsymbol{e}_3$. Fix two small parameters ε and $\delta \in (0,1)$, and consider in (5.66) the domain

$$E = (0,1)^2 \times (0,\delta). \tag{5.79}$$

We shall prove the claim by constructing a suitable test function $\boldsymbol{v}$ on the domain E. Let $g : E \to \mathbb{R}$ be defined by

$$g(\boldsymbol{x}) = \begin{cases} x_3/\varepsilon & \text{if } x_3 \leq \varepsilon\delta \\ \delta & \text{if } x_3 \geq \varepsilon\delta\,, \end{cases} \tag{5.80}$$

and set

$$h(\boldsymbol{x}) = \min(g(\boldsymbol{x}), x_3 + \xi \mathrm{dist}(\boldsymbol{x}, \partial E))\,, \tag{5.81}$$

where ξ is a positive number smaller than $1/|a_{k+1}|$. We define

$$\boldsymbol{u}(\boldsymbol{x}) = \boldsymbol{F}_k \boldsymbol{x} + \boldsymbol{F}_k \boldsymbol{a}_k h(\boldsymbol{x})\,. \tag{5.82}$$

and compute

$$\nabla \boldsymbol{u}(\boldsymbol{x}) = \boldsymbol{F}_k + \boldsymbol{F}_k \boldsymbol{a}_k \otimes \nabla h(\boldsymbol{x})\,. \tag{5.83}$$

This gradient is constant in each of finitely many pieces of E (four in two dimensions, cf Fig. 5.13; six in three dimensions), and it takes values $\boldsymbol{F}_k$, $\boldsymbol{F}_k(\boldsymbol{I} + \varepsilon^{-1}\boldsymbol{a}_{k+1} \otimes \boldsymbol{b}_{k+1})$, $\boldsymbol{F}_k(\boldsymbol{I} + \boldsymbol{a}_{k+1} \otimes (\boldsymbol{e}_3 \pm \xi \boldsymbol{e}_1))$, $\boldsymbol{F}_k(\boldsymbol{I} + \boldsymbol{a}_{k+1} \otimes (\boldsymbol{e}_3 \pm \xi \boldsymbol{e}_2))$, which all have positive determinant. The function $\boldsymbol{u}(\boldsymbol{x})$ is Lipschitz continuous, and equals $F_{k+1}\boldsymbol{x}$ on ∂E. Let ω be the subset of E where $\nabla \boldsymbol{u} = \boldsymbol{F}_k$. By the inductive assumption, $W^{\mathrm{qc}}(\boldsymbol{F}_k) \leq W^e(\boldsymbol{F}^e)$, hence (using the definition (5.66) on the domain ω), for any $\eta > 0$ there is a Lipschitz continuous function $\boldsymbol{v}' : \omega \to \mathbb{R}^3$ such that

$$\boldsymbol{v}'(\boldsymbol{x}) = \boldsymbol{F}_k \boldsymbol{x} \text{ on } \partial\omega\,, \quad \text{and} \quad \frac{1}{|\omega|} \int_\omega W(\nabla \boldsymbol{v}') dV \leq W^e(\boldsymbol{F}^e) + \eta\,. \tag{5.84}$$

We define $\boldsymbol{w} : E \to \mathbb{R}^3$ by

$$\boldsymbol{w}(\boldsymbol{x}) = \begin{cases} \boldsymbol{v}'(\boldsymbol{x}) & \text{if } \boldsymbol{x} \in \omega\,, \\ \boldsymbol{u}(\boldsymbol{x}) & \text{if } \boldsymbol{x} \in E \setminus \omega\,. \end{cases} \tag{5.85}$$

The function $\boldsymbol{w}$ is Lipschitz continuous, and $\boldsymbol{w}(\boldsymbol{x}) = \boldsymbol{F}_{k+1}\boldsymbol{x}$ on ∂E. Therefore $\boldsymbol{v}(\boldsymbol{x}) = \boldsymbol{w}(\boldsymbol{x}) - \boldsymbol{F}_{k+1}\boldsymbol{x} \in W_0^{1,\infty}(E)$ and, from the definition (5.66), we have

$$W^{\mathrm{qc}}(\boldsymbol{F}_{k+1}) \le \frac{1}{|E|}\int_E W(\boldsymbol{F}_{k+1} + \nabla \boldsymbol{v})dV = \frac{1}{|E|}\int_E W(\nabla \boldsymbol{w})dV\,. \tag{5.86}$$

It remains to evaluate the last integral. The contribution from ω is controlled by (5.84). On the rest the gradient $\nabla \boldsymbol{w} = \nabla \boldsymbol{u}$ takes only five distinct values, as mentioned above. The large gradient $\nabla \boldsymbol{u} = \boldsymbol{F}_k(\boldsymbol{I} + \varepsilon^{-1}\boldsymbol{a}_{k+1} \otimes \boldsymbol{b}_{k+1})$ is taken only in a thin strip $S \subset (0,1)^2 \times (0, \varepsilon\delta)$, which has volume controlled by $|S| \le \varepsilon|E|$. The corresponding energy is controlled by

$$\int_S W(\nabla \boldsymbol{w})dV \le |E|\varepsilon \left[W^e(\boldsymbol{F}_k) + f\left(\frac{1}{\varepsilon}\boldsymbol{a}_{k+1} \cdot \boldsymbol{b}_{k+1}, \frac{1}{\varepsilon}|\boldsymbol{a}_{k+1} \times \boldsymbol{b}_{k+1}|\right)\right]\,. \tag{5.87}$$

By (5.64), we get

$$\lim_{\varepsilon \to 0} \varepsilon \left[W^e(\boldsymbol{F}_k) + f\left(\frac{1}{\varepsilon}\boldsymbol{a}_{k+1} \cdot \boldsymbol{b}_{k+1}, \frac{1}{\varepsilon}|\boldsymbol{a}_{k+1} \times \boldsymbol{b}_{k+1}|\right)\right] = 0\,, \tag{5.88}$$

hence we can choose ε sufficiently small so that the integral in (5.87) is less than $|E|\eta$. The remaining pieces are located close to the short sides of E, and have the form of closure domains (see Figure 5.13). Their volume is controlled by is $\delta|E|$, and $\boldsymbol{F}$ there takes the four values $\boldsymbol{F}_k(\boldsymbol{I} + \boldsymbol{a}_{k+1} \otimes (\boldsymbol{e}_3 \pm \xi\boldsymbol{e}_{1,2}))$, which do not depend on ε and δ. Therefore we can choose δ so that

$$\begin{aligned} &\delta|E|W^e\left(\boldsymbol{F}_k(\boldsymbol{I} + \boldsymbol{a}_{k+1} \otimes (\boldsymbol{e}_3 \pm \xi\boldsymbol{e}_1))\right) \\ &\quad + \delta|E|W^e\left(\boldsymbol{F}_k(\boldsymbol{I} + \boldsymbol{a}_{k+1} \otimes (\boldsymbol{e}_3 \pm \xi\boldsymbol{e}_2))\right) \le \eta\,. \end{aligned} \tag{5.89}$$

We conclude that

$$W^{\mathrm{qc}}(\boldsymbol{F}_{k+1}) \le \frac{1}{|E|}\int_\omega W(\nabla \boldsymbol{w})dV + 3\eta \le W^e(\boldsymbol{F}^e) + 4\eta \tag{5.90}$$

which, since η was arbitrary, proves the claimed (5.77).

It remains to be shown that (5.77) implies the thesis. This follows from the fact that any matrix of unit determinant can be written as product of simple shears of the form $\boldsymbol{I} + \lambda \boldsymbol{e}_i \otimes \boldsymbol{e}_j$, with $i \neq j$ and $\lambda \in \mathbb{R}$ (to see this, just consider that multiplying $\boldsymbol{F}$ by $\boldsymbol{I} + \lambda \boldsymbol{e}_i \otimes \boldsymbol{e}_j$ on the left corresponds to adding a multiple of the i-th column to the j-th one, and multiplying on the right does the same on rows. Therefore the claim is equivalent to Gauss reduction). We conclude that given any pair of matrices $\boldsymbol{F}$, $\boldsymbol{F}^e$ with $0 < \det \boldsymbol{F}^e \leq \det \boldsymbol{F}$, one can find vectors $\boldsymbol{a}_i$ and $\boldsymbol{b}_i$ with $\boldsymbol{a}_i \cdot \boldsymbol{b}_i \geq 0$ such that

$$\boldsymbol{F} = \boldsymbol{F}^e \prod_{i=1}^{k} (\boldsymbol{I} + \boldsymbol{a}_i \otimes \boldsymbol{b}_i) \,. \tag{5.91}$$

Then, the claim (5.77) implies that

$$W^{\mathrm{qc}}(\boldsymbol{F}) \leq W^e(\boldsymbol{F}^e) \qquad \text{for all } \boldsymbol{F}^e \text{ with } \det \boldsymbol{F}^e \leq \det \boldsymbol{F} \,. \tag{5.92}$$

We conclude

$$W^{\mathrm{qc}}(\boldsymbol{F}) \leq \varphi(\det \boldsymbol{F}) \,, \tag{5.93}$$

where φ was defined in (5.68). Consider now a matrix $\boldsymbol{F}$, and view it as the average of

$$\boldsymbol{F}_{\pm} = \boldsymbol{F} \left(\boldsymbol{I} \pm \frac{1}{2} \boldsymbol{e}_1 \otimes \boldsymbol{e}_1 \right) . \tag{5.94}$$

By lamination it follows that

$$W^{\mathrm{qc}}(\boldsymbol{F}) \leq \frac{W^{\mathrm{qc}}(\boldsymbol{F}_+) + W^{\mathrm{qc}}(\boldsymbol{F}_-)}{2} \leq \frac{1}{2} \left[\varphi \left(\frac{3}{2} \det \boldsymbol{F} \right) + \varphi \left(\frac{1}{2} \det \boldsymbol{F} \right) \right] , \tag{5.95}$$

and the same can be done with any other weight. This shows that

$$W^{\mathrm{qc}}(\boldsymbol{F}) \leq \varphi^{**}(\det \boldsymbol{F}) \,. \tag{5.96}$$

But $\varphi^{**}(\det \boldsymbol{F})$ is polyconvex function, and $\varphi^{**}(\det \boldsymbol{F}) \leq W(\boldsymbol{F})$, hence equality holds. $\square$

Conclusions

La recherche présentée in ce travail discute le développement des outils numériques basés sur la discrétisation par éléments finis pour la simulation des phénomènes dynamiques de rupture avec des approches cohésives. Les procédures numériques ont été développées entièrement sous tous leurs aspects: contexte théorique, mise en oeuvre des éléments finis, procédures d'adaptativité du maillage, applications, extensions aux modèles de matériau multi-échelle .

Du point de vue théorique, les théories cohésives ont été passées en revue exactement, inséré dans un cadre thermodynamique expliquant la cinématique et l'irréversibilité des materieux non-linéaires. On a proposé une classe générale de lois cohésive capable de traiter le chargement en plusiers modes et on a mise en application et employées dans des applications différentes lois cohésives.

En parallèle, on a développé éléments finis de interface suivants une discrétisation tridimensionnelle quadratique du continus. Un problème important adressé et résolu c'est la définition unique des paramètres géométriques des éléments cohésifs, en particulier la normale, qui permit de séparer les composantes du déplacement d'ouverture sous différentes conditions de charge.

Pour éviter la déformabilité excessive du système discrétisé, ayant pour résultat une séparation preliminaire du maillage, on a développé une procédure spéciale d'adaptation du maillage. À partir d'un premier maillage cohérente, un test de rupture est exécutée sur les surfaces de séparation des éléments à chaque étape du chargement. Si le critère de rupture est satisfait, l'interface est rompue, en ajoutant de nouveaux noeuds à le maillage et en actualisant la liste de connectivité. Comme conséquence de la rupture, la topologie du corps peut changer considérablement, et des fragmentations complexes peuvent être suivis.

Des applications aux matériaux ductiles (acier et aluminium), aux matériaux fragiles (béton, céramique, PMMA), et aux matériaux polymèriques, repliant beaucoup d'observations expérimentales, ont démontré la bonne performance de la procédure

adaptative. En particulier, dû à la échelle intrinsèque de longueur des théories cohésives, nous pourrions obtenir des résultats indépendants du maillage en termes de propagation de fissure et de réponses globales des simulations. L'échelle du temps résultant de l'accouplement des théories cohésives et de la dynamique peut capturer la dépendance de la vitesse de déformations observée dans la dynamique, pour beaucoup de matériaux et beaucoup de conditions de chargement.

Les modèles cohésifs distribuée, convenablement insérés dans les modèles de materiau continu, peuvent prévoir le comportement des matériaux fragiles subissant un état compressif global. Ces modèles des matériaux sont particulièrement avantageux pour des applications géologiques, et ceci représente une des subjects de notre recherche courante.

Les outils développés sont employés pour analyser nouveaux matériaux, en particulier les tissus biologiques qui subissent de grandes déformations et sont caractcrisés par la présence des fibres de renforcement en collagène. Ces matcriaux cassent autant que d'autres matériaux, mais la rupture n'est pas typiquement fragile. Nouvelles lois cohésives, tenant compte de l'anisotropie et des comportements dépendant du vitesse de déformation sont à l'étude, en applications modelizant la rupture dans les artères humaines affectées par l'athérosclérose et la chirurgie d'angioplastie.

Comme décrit dans la partie finale de l'introduction, un autre champ stimulant qui réclame l'utilisation des méthodes cohésives est le cheminement quasi-statique de la fissure, basé sur considérations cnergetiques. Cette dernière subject, qui prend prvsentement la majeure partie de notre temps de recherche, semble bien plus difficile que celle que nous avons explorée et avons partiellement résolu jusqu'à maintenant. Nous sommes confiants que nos instruments peuvent nous aider à avancer quelques pas en avant dans ces domaines fascinants.

Bibliography

[1] E. C. Aifantis. On the microstructural origin of certain inelastic models. *Journal of Engineering Materials and Technology*, 106:326–330, 1984.

[2] E. C. Aifantis. The physics of plastic deformations. *International Journal of Plasticity*, 3:211–247, 1987.

[3] L. Ambrosio. A compactness theorem for a new class of functions of bounded variation. *Bollettino dell'Unione Matematica Italiana*, 3-B:857–881, 1989.

[4] L. Ambrosio. Existence theory for a new class of variational problems. *Archives of Rational Mechanics and Analysis*, 111:291–322, 1990.

[5] L. Ambrosio and A. Braides. Energies in SBV and variational models in fracture mechanics. In D. Cioranescu, A. Damlamian, and P. Donato, editors, *Homogenization and Applications to Material Sciences*, pages 1–22. GAKUTO, Gakkotosho, Tokio, Japan, 1997.

[6] F. Armero and K. Garikipati. An analysis of strong discontinuities in multiplicative finite strain plasticity and their relation with the numerical simulation of strain localization in solids. *International Journal of Solids and Structures*, 33:2863–2885, 1996.

[7] S. Aubry, M. Fago, and M. Ortiz. A constrained sequential-lamination algorithm for the simulation of sub-grid microstructures in martensitic materials. *Computer Methods in Applied Mechanics and Engineering*, 192:2823–2843, 2003.

[8] G. I. Barenblatt. The mathematical theory of equilibrium of cracks in brittle fracture. *Advances in Applied Mechanics*, 7:55–129, 1962.

[9] Z. P. Bažant. Instability, ductility and size-effect in strain-softening concrete. *Journal of Engineering Mechanics/ASCE*, 102:331–344, 1976.

[10] Z. P. Bažant. Mechanics of distributed cracking. *Applied Mechanics Reviews*, 39:675–705, 1986.

[11] Z. P. Bažant and L. Cedolin. *Stability of Dtructures: Elastic, Inelastic, Fracture and Damage Theories*. Martinus Nijhoff, Dordrecht, The Netherlands, 1986.

[12] Z. P. Bažant and M. Jirasek. Nonlocal model based on crack interactions: A localization study. *Journal of Engineering Materials and Technology*, 116:256–259, 1994.

[13] Z. P. Bažant and M. Jirasek. Nonlocal integral formulations of plasticity and damage: survey of progress. *Journal of Engineering Mechanics/ASCE*, 128:1119–1149, 2002.

[14] Z. P. Bažant and Cedolin L. Blunt crack propagation in finite element analysis. *Journal of Engineering Mechanics/ASCE*, 105:297–315, 1979.

[15] Z. P. Bažant and G. Pijaudier-Cabot. Nonlocal continuum damage, localization instability and convergence. *Journal of Applied Mechanics*, 55:287–293, 1988.

[16] Z. P. Bažant and J. Planas. *Fracture and Size Effect in Concrete and Other Quasibrittle Materials*. CRC Press, Boca Raton, Florida, 1998.

[17] G. E. Beltz and J. R. Rice. Book Chapter: Dislocation Nucleation versus Cleavage Decohesion at Crack Tips. In T. C. Lowe, A. D. Rollett, P. S. Follansbee, and G. S. Daehn, editors, *Modeling the Deformation of Crystalline Solids: Physical Theory, Application and Experimental Comparisons*, pages 457–480. TSM-AIME, Warrendale, PA, 1991.

[18] T. Belytschko. An overview of semidiscretization and time integration procedures. In T. Belytschko and T. J. R. Hughes, editors, *Computational Methods for Transient Analysis*, pages 1–65. North-Holland, 1983.

[19] T. Belytschko, J. Fish, and B. E. Englemann. A finite element with embedded localization zones. *Computer Methods in Applied Mechanics and Engineering*, 70:59–89, 1988.

[20] H. Ben Belgacem, S. Conti, A. De Simone, and S. Müller. Energy scaling of compressed elastic films. *Archives of Rational Mechanics and Analysis*, 164:1–37, 2002.

[21] K. Bhattacharya and M. Luskin. The simply laminated microstructure in martensitic crystals that undergo a cubic-to-orthorhombic phase transformation. *Archives of Rational Mechanics and Analysis*, 149:123–154, 1999.

[22] P. Bocca, A. Carpinteri, and Valente S. Mixed-mode fracture of concrete. *International Journal of Solids and Structures*, 27:1139–1153, 1991.

[23] G. Bouchitté, I. Fonseca, and L. Mascarenhas. A global method for relaxation. *Archives of Rational Mechanics and Analysis*, 145:51–98, 1998.

[24] B. Bourdin, G. A. Francfort, and J. J. Marigo. Numerical experiment in revised brittle fracture. *Journal of the Mechanics and Physics of Solids*, 48:797–826, 2000.

[25] A. F. Bower and M. Ortiz. A 3-dimensional analysis of crack trapping and bridging by tough particles. *Journal of the Mechanics and Physics of Solids*, 39:815–858, 1991.

[26] A. F. Bower and M. Ortiz. The influence of grain size on the toughness of monolithic ceramics. *Transactions of the ASME*, 115:228–236, 1993.

[27] A. Braides and V. Chiadò Piat. Integral representation results for functionals defined on SBV. *SISSA ISAS*, 198/M:1–31, 1994.

[28] A. Braides and A. Defranceschi. *Homogenization of multiple integrals*. Claredon Press, Oxford, 1998.

[29] A. Braides, A. Defranceschi, and E. Vitali. Homogenization of free discontinuity problems. *Archives of Rational Mechanics and Analysis*, 135:297–356, 1996.

[30] G. T. Camacho and M. Ortiz. Computational modelling of impact damage in brittle materials. *International Journal of Solids and Structures*, 33:2899–2938, 1996.

[31] G. T. Camacho and M. Ortiz. Adaptive lagrangian modelling of ballistic penetration of metallic targets. *Computer Methods in Applied Mechanics and Engineering*, 142:269–301, 1997.

[32] A. Carpinteri. *Mechanical Damage and Crack Growth in Concrete*. Martinus Nijhoff, Dordrecht, The Netherlands, 1986.

[33] G. Chen, W. N. and Ravichandran. Dynamic compressive behavior of ceramics under lateral confinement. *Journal de Physique IV*, 4:177–182, 1994.

[34] G. Chen, W. N. and Ravichandran. Static and dynamic compressive behavior of aluminum nitride under moderate confinement. *Journal of the American Ceramic Society*, 79:579–584, 1996.

[35] W. Chen and G. Ravichandran. An experimental technique for imposing dynamic multiaxial compression with mechanical confinement. *Experimental Mechanics*, 36:155–158, 1996.

[36] W. Chen and G. Ravichandran. Failure mode transition in ceramics under dynamic multiaxial compression. *International Journal of Fracture*, 101:141–159, 2000.

[37] K.E. Clark and G.W. Milton. Modeling the effective conductivity function of an arbitrary 2-dimensional polycrystal using sequential laminates. *Proceedings of the Royal Society of Edinburgh A*, 124:757–783, 1994.

[38] D. Coker and A. J. Rosakis. Experimental observations of intersonic crack growth in asymmetrically loaded unidirectional composites plates. *Philosophical Magazine A*, 81(3):571–595, 2001.

[39] C. Comi. Computational modelling of gradient-enhanced damage in quasi-brittle materials. *Mechanics of Cohesive and Frictional Materials*, 4:17–36, 1999.

[40] S. Conti and M. Ortiz. Dislocation microstructures and the effective behavior of single crystals. *Archives of Rational Mechanics and Analysis*, 176:103–147, 2005.

[41] A. Corigliano and O. Allix. Some aspects of interlaminar degradation in composites. *Computer Methods in Applied Mechanics and Engineering*, 185:203–224, 2000.

[42] A. Corigliano, S. Mariani, and A. Pandolfi. Numerical modeling of rate-dependent debonding processes in composites. *Composites Structures*, 61:39–50, 2003.

[43] A. Corigliano, S. Mariani, and A. Pandolfi. Numerical analysis of rate-dependent dynamic c omposite delamination. *Composites Science and Technology*, 66:766–775, 2006.

[44] A. Corigliano and M. Ricci. Rate-dependent interface models: formulation and numerical applications. *International Journal of Solids and Structures*, 38:547–576, 1999.

[45] E. Cosserat and F. Cosserat. *Théorie de Corps Deformables*. Hermann, A., Paris, 1909.

[46] A. M. Cuitiño and M. Ortiz. A material-independent method for extending stress update algorithms from small-strain plasticity to finite plasticity with multiplicative kinematics. *Engineering Computations*, 9:437–451, 1992.

[47] B. Dacorogna. *Direct methods in the calculus of variations*. Springer-Verlag, New York, 1989.

[48] G. Dal Maso. *An introduction to* Γ*-convergence*. Birkhäuser, Boston, 1993.

[49] G. Dal Maso, G. A. Francfort, and R. Toader. Quasistatic crack growth in nonlinear elasticity. *Archives of Rational Mechanics and Analysis*, 176:165–225, 2005.

[50] G. Dal Maso and R. Toader. A model for the quasi-static growth of brittle fracture: existence and approximation results. *Archives of Rational Mechanics and Analysis*, 162:101–135, 2002.

[51] A. De-Andrés, J. L. Pérez, and M. Ortiz. Elastoplastic finite element analysis of three-dimensional fatigue crack growth in aluminum shafts subjected to axial loading. *International Journal of Solids and Structures*, 36:2231–3358, 1999.

[52] R. de Borst. A generalization of J2-flow theory for polar continua. *Computer Methods in Applied Mechanics and Engineering*, 103:347–362, 1993.

[53] R. de Borst. Some recent developments in computational modelling of concrete fracture. *International Journal of Fracture*, 86:5–36, 1997.

[54] R. de Borst and H. B. Mühlhaus. Gradient-dependend plasticity. Formulation and algorithmic aspects. *International Journal for Numerical Methods in Engineering*, 35:521–539, 1992.

[55] R. de Borst, J. Pamin, R. H. J. Peerlings, and L. J. Sluys. On gradient-enhanced damage and plasticity models for failure in quasi-brittle and frictional materials. *Computational Mechanics*, 17:130–141, 2001.

[56] E. De Giorgi and L. Ambrosio. Un nuovo funzionale del calcolo delle variazioni. *Atti dell'Accademia Nazionale dei Lincei. Rendiconti della Classe di Scienze Fisiche, Matematiche e Naturali*, 82:199–210, 1988.

[57] E. De Giorgi, M. Carriero, and A. Leaci. Existence theorem for a minimum problem with free discontinuity set. *Archives of Rational Mechanics and Analysis*, 108:105–218, 1989.

[58] E. De Giorgi and T. Franzoni. Su un tipo di convergenza variazionale. *Atti dell'Accademia Nazionale dei Lincei. Rendiconti della Classe di Scienze Fisiche, Matematiche e Naturali*, 58:842–850, 1975.

[59] S. Demoulini. Young measure solutions for nonlinear evolutionary systems of mixed type. *Annales de L'Institute Henri Poincaré d'Analyse Non Linéaire*, 14:143–162, 1997.

[60] G. Dolzmann. Numerical computation of rank-one convex envelopes. *SIAM Journal of Numerical Analysis*, 36:1621–1635, 1999.

[61] J. Du, J. H. Yon, N. M Hawkins, K. Arakawa, and A. S. Kobayashi. Fracture process zone for concrete for dynamic loading. *ACI Materials Journal*, 89:252–258, 1992.

[62] D. S. Dugdale. Yielding of steel sheets containing slits. *Journal of the Mechanics and Physics of Solids*, 8:100–104, 1960.

[63] M. Elices and J. Planas. The equivalent elastic crack. 1. Load-Y equivalences. *International Journal of Fracture*, 61:159–172, 1993.

[64] M. L. Falk, A. Needleman, and J. R. Rice. A critical evaluation of cohesive zone models of dynamic fracture. *Journal de Physique IV*, 11 (PR5):43–50, 2001.

[65] J.E. Field, Q. Sun, and D. Townsend. Modeling the deformation of crystalline solids: Physical theory, application and experimental comparisons. In *Ballistic Impact of Ceramics, Institute of Physics Conference Series No 102: Session 7*, Oxford, 1989.

[66] N. A. Fleck and J. W. Hutchinson. A reformulation of strain gradient plasticity. *Journal of the Mechanics and Physics of Solids*, 49:2245–2271, 2001.

[67] I. Fonseca and G. A. Francfort. Relaxation in BV versus quasiconvexification in $W^{1,p}$; a model for the interaction between fracture and damage. *Calculus of Variations*, 3:407–446, 1995.

[68] G. A. Francfort and J. J. Marigo. Revisiting brittle fracture as an energy minimization problem. *Journal of the Mechanics and Physics of Solids*, 46:1319–1342, 1998.

[69] G. A. Francfort and G. W. Milton. Sets of conductivity and elasticity tensors stable under lamination composite-materials with poisson ratios close to -1. *Communications on Pure and Applied Mathematics*, 47:257–279, 1992.

[70] G. Friesecke and G. Dolzmann. Implicit time discretization and global existence for a quasi-linear evolution equation with nonconvex energy. *SIAM Journal of Numerical Analysis*, 28:363–380, 1997.

[71] F. Gálvez. *Caracterización Mecánica de Materiales Cerámicos Avanzados a Altas Velocidades de Deformación*. PhD thesis, Departamento de Motopropulsión y Fluidodinámica, ETS de Ingenieros Aeronáuticos, Universidad Politécnica de Madrid, Spain, 1999. (*Mechanical Characterization of Advanced Ceramics at High Strain Rates*, in Spanish).

[72] F. Gálvez, J. Rodríguez, and V. Sánchez-Gálvez. Influence of the strain rate on the tensile strength in aluminas of different purity. *Journal de Physique IV*, 10:323–328.

[73] F. Gálvez, J. Rodríguez, and V. Sánchez-Gálvez. Tensile measurements of ceramic materials at high rates of strain. *Journal de Physique IV*, C3:151–156, 1997.

[74] T. C. Gasser and G. A. Holzapfel. Modeling 3d crack propagation in unreinforced concrete using pufem. *Computer Methods in Applied Mechanics and Engineering*, 194:2859–2896, 2005.

[75] A. A. Griffith. The phenomena of rupture and flow in solids. *Philosophical Transactions of the Royal Society of London A*, 221:163–197, 1921.

[76] Z. K. Guo, A. S. Kobayashi, and N. M Hawkins. Dynamic mixed mode fracture of concrete. *International Journal of Solids and Structures*, 32:2591–2607, 1995.

[77] Z. K. Guo, A. S. Kobayashi, J. C. Hay, and K. W. White. Fracture process zone modeling of monolithic Al_2O_3. *Engineering Fracture Mechanics*, 63:115–129, 1999.

[78] J. C. Hay and K. E. White. Grain boundary phases and wake zone characterization in monolithic alumina. *Journal of the American Ceramic Society*, 78:1025–1032, 1995.

[79] A. Hillerborg, M. Modeer, P. E. Petersson, and A. Needleman. Analysis of crack formation and crack growth in concrete by means of fracture mechanics and finite elements. *Cement Concrete Resarch*, 6:773–782, 1976.

[80] C. M. Hoffmann. *Geometric and Solid Modeling*. Morgan Kaufmann Publishers, San Mateo, California, 1989.

[81] M. L. Hughes, J. W. Tedesco, and A. Ross. Numerical analysis of high strain rate splitting-tensile tests. *Composites Structures*, 47:653–671, 1993.

[82] T. J. R. Hughes. Analysis of transient algorithms with particular reference to stability behavior. In T. Belytschko and T. J. R. Hughes, editors, *Computational Methods for Transient Analysis*, pages 67–155. North-Holland, 1983.

[83] C. E. Inglis. Stresses in a plate dur to the presence of cracks and sharp corners. *Trans. Inst. Naval Arch.*, V.LV:219–230, 1913.

[84] G. R. Irwin. Analysis of stresses and strains near the end of a crack traversing a plate. *Journal of Applied Mechanics*, 79:361–364, 1957.

[85] M. Jirásek. Comparative study of finite elements with embedded discontinuities. *Computer Methods in Applied Mechanics and Engineering*, 188:307–330, 2000.

[86] J. W. Ju. On energy-based coupled elastoplastic damage theories: constitutive modelling and computational aspects. *International Journal of Solids and Structures*, 25:803–833, 1989.

[87] C. Kane, E. A. Repetto, M. Ortiz, and J. E. Marsden. Finite element analysis of nonsmooth contact. *Computer Methods in Applied Mechanics and Engineering*, 180:1–26, 1999.

[88] M. E. Kipp, D. E. Grady, and J. W. Swegle. Numerical and experimental studies of high-velocity impact fragmentation. *International Journal of Impact Engineering*, 14:427–438, 1993.

[89] A. S. Kobayashi. Dinamic fracture of ceramics and ceramic composites. *Materials Science and Engineering*, A143:111–117, 1991.

[90] R. V. Kohn and S. Müller. Branching of twins near an austenite-twinned-martensite interface. *Philosophical Magazine A*, 66:697–715, 1992.

[91] R. V. Kohn and Müller S. Surface energy and microstructure in coherent phase transitions. *Communications on Pure and Applied Mathematics*, 47:405–435, 1994.

[92] R. V. Kohn and G. Strang. Optimal design and relaxation of variational problems, I, II and III. *Communications on Pure and Applied Mathematics*, 39:113–137, 139–182, 353–377, 1986.

[93] I. A. Kunin. *Elastic media with microstructure I. One-dimensional models.* Springer-Verlag, Berlin, Heidelberg, New-York, 1982.

[94] I. A. Kunin. *Elastic media with microstructure 1II. Three-dimensional models.* Springer-Verlag, Berlin, Heidelberg, New-York, 1983.

[95] J. Lemaitre. How to use damage mechanics. *Nuclear Engineeering Design*, 80:233–245, 1984.

[96] B. Li and M. Luskin. Approximation of a martensitic laminate with varying volume fractions. *Mathematical Modelling and Numerical Analysis M2AN*, 33:67–87, 1999.

[97] C. Liu, W. . Knauss, and A. J. Rosakis. Loading rates and the dynamic initiation toughness in brittle solids. *International Journal of Fracture*, 90:103–118, 1998.

[98] R. Löhner and P. Parikh. Generation of three-dimensional unstructure grids by the advancing-front method. *International Journal for Numerical Methods in Fluids*, 8:1135–1149, 1988.

[99] J. Lubliner. On the thermodynamic foundations of non-linear solid mechanics. *International Journal of Non-Linear Mechanics*, 7:237–254, 1972.

[100] J. Lubliner. On the structure of the rate equations of materials with internal variables. *Acta Mechanica*, 17:109–119, 1973.

[101] M. Luskin. On the computation of crystalline microstructure. *Acta Numerica*, 5:191–257, 1996.

[102] V. Lyakhovsky. Scaling of fracture length and distributed damage. *Geophysical Journal International*, 144:114–122, 2001.

[103] V. Lyakhovsky, Y. Ben-Zion, and Agnon A. Distributed damage, faulting, and friction. *Journal of Geophysical Research - Solid Earth*, 102:27635–27649, 1997.

[104] M. Mantyla. *An Introduction to Solid Modeling.* Computer Science Press, Rockwille, Maryland, 1988.

[105] S. Mariani, A. Pandolfi, and R. Pavani. Coupled space-time multiscale simulations of dynamic delamination. *Materials Science – Poland*, 23:509–519, 2005.

[106] J. E. Marsden and T. J. R. Hughes. *Mathematical Foundations of Elasticity*. Prentice-Hall, Englewood Cliffs, N.J., 1983.

[107] T. D. Marusich and M. Ortiz. Modelling and simulation of high-speed machining. *International Journal for Numerical Methods in Engineering*, 38:3675–3694, 1995.

[108] K. K Mathur, A. Needleman, and V. Tvergaard. Three dimensional analysis of dynamic ductile crack growth in a thin plate. *Journal of the Mechanics and Physics of Solids*, 44:439–464, 1996.

[109] J. Mazars and G. Pijaudier-Cabot. Continuum damage theory — application to concrete. *Journal of Engineering Mechanics/ASCE*, 115:345–365, 1989.

[110] J. M Melenk and I. Babuska. The partition of unity finite element method. Basic theory and applications. *Computer Methods in Applied Mechanics and Engineering*, 139:289–314, 1996.

[111] G. W. Milton. Composite materials with poisson's ratios close to -1. *Journal of the Mechanics and Physics of Solids*, 40:1105–1137, 1992.

[112] R. D. Mindlin. Micro-structure in linear elasticity. *Archives of Rational Mechanics and Analysis*, 16:51–78, 1964.

[113] N. Moës and T. Belytschko. A finte element method for crack growth without remeshing. *Engineering Fracture Mechanics*, 69:813–833, 2002.

[114] N. Moës, J. Dolbow, and T. Belytschko. A finte element method for crack growth without remeshing. *International Journal for Numerical Methods in Engineering*, 46:131–150, 1999.

[115] J. F. Molinari, G. Gazonas, R. Raghupathy, A. Rusinek, and F. Zhou. The cohesive element approach to dynamic fragmentation: The question of energy convergence. *International Journal for Numerical Methods in Engineering*, 69:483–503, 2007.

[116] J. F. Molinari and M. Ortiz. Three-dimensional adaptive meshing by subdivision and edge-collapse in finite-deformation dynamic-plasticity problems with application to adiabatic shear banding. *International Journal for Numerical Methods in Engineering*, 53:1101–1126, 2002.

[117] J. W. Morrissey and J. R. Rice. Crack front waves. *Journal of the Mechanics and Physics of Solids*, 46:467–487, 1998.

[118] S. Müller. Variational models for microstructure and phase transitions. In F. Bethuel et al., editors, *in: Calculus of variations and geometric evolution problems*, Springer Lecture Notes in Math. 1713, pages 85–210. Springer, Berlin, 1999.

[119] A. Needleman. A continuum model for void nucleation by inclusion debonding. *Journal of Applied Mechanics*, 54:525–531, 1987.

[120] A. Needleman. An analysis of decohesion along an imperfect interface. *International Journal of Fracture*, 42:21–40, 1990.

[121] A. Needleman. Micromechanical modeling of interfacial decohesion. *Ultramicroscopy*, 40:203–214, 1992.

[122] O. Nguyen and M. Ortiz. Coarse-graining and renormalization of atomistic binding relations and universal macroscopic cohesive behavior. *Journal of the Mechanics and Physics of Solids*, 50:1727–1741, 2002.

[123] T. Nicholas and R. F. Recht. Introduction to Impact Phenomena. In J. A. Zukas, editor, *High Velocity Impact Dynamics*, pages 1–63. John Wiley and Sons, 1990.

[124] J. Oliver, M. Cervera, and O. Manzoli. On the use of j2-plasticity models for the simulation of strong discontinuities in solids. In D. .R. J. Oden, E. Oñate, and E. Hinton, editors, *Computational Plasticity: Fundamentals and Applications*, pages 38–55, Proceedings of COMPLAS V, CIMNE, Barcelona, 1997. Baklema, Rotterdam.

[125] J. Oliver, A. E. Huespe, M. D. G. Pulido, and E. Samaniego. On the strong discontinuity approach in finite deformation settings. *International Journal for Numerical Methods in Engineering*, 56:1051–1082, 2003.

[126] J. Oliver, A. E. Huespe, and E. Samaniego. A study on finite elements for capturing strong discontinuities. *International Journal for Numerical Methods in Engineering*, 57:2135–2161, 2003.

[127] J. Oliver and D. G. Pulido. On the use of strain-softening damage constitutive equations to model cracking of concrete. In R. de Borst, N. Bićanić, and H. Mang, editors, *Computational Modelling of Concrete Structures*, pages 363–372. Baklema, Rotterdam, 1998.

[128] J. Oliver and J. C. Simo. Modelling strong discontinuities in solid mechanics by means of strain softening constitutive equations. In H. Mang, N. Bićanić, and R. de Borst, editors, *Computational Modelling of Concrete Structures*, pages 363–372. Pineridge, Swansea, 1994.

[129] M. Ortiz. A constitutive theory for the inelastic behavior of concrete. *Mechanics of Materials*, 4:67–93, 1985.

[130] M. Ortiz. Microcrack coalescence and macroscopic crack growth initiation in brittle solids. *International Journal of Solids and Structures*, 24:231–250, 1988.

[131] M. Ortiz. Computational micromechanics. *Computational Mechanics*, 18:321–338, 1996.

[132] M. Ortiz, Y. Leroy, and A. Needleman. A finite element method for localized failure analysis. *Computer Methods in Applied Mechanics and Engineering*, 61:189–214, 1987.

[133] M. Ortiz and A. Pandolfi. A class of cohesive elements for the simulation of three-dimensional crack propagation. *International Journal for Numerical Methods in Engineering*, 44:1267–1282, 1999.

[134] M. Ortiz and E. A. Repetto. Nonconvex energy minimization and dislocation structures in ductile single crystals. *Journal of the Mechanics and Physics of Solids*, 47:397–462, 1999.

[135] M. Ortiz, E. A. Repetto, and L. Stainier. A theory of subgrain dislocation structures. *Journal of the Mechanics and Physics of Solids*, 48:2077–2114, 2000.

[136] M. Ortiz and L. Stainier. The variational formulation of viscoplastic constitutive updates. *Computer Methods in Applied Mechanics and Engineering*, 171:419–444, 1999.

[137] M. Ortiz and S. Suresh. Statistical properties of residual stresses and intergranular fracture in ceramic materials. *Journal of Applied Mechanics*, 60:77–84, 1993.

[138] A. Pandolfi, P. R. Guduru, M. Ortiz, and A. J. Rosakis. Three dimensional cohesive-element analysis and experiments of dynamic fracture in c300 steel. *International Journal of Solids and Structures*, 37:3733–3760, 2000.

[139] A. Pandolfi, C. Kane, M. Ortiz, and J. E. Marsden. Time-discretized variational formulation of nonsmooth frictional contact. *International Journal for Numerical Methods in Engineering*, 53:1801–1830, 2002.

[140] A. Pandolfi, P. Krysl, and M. Ortiz. Finite element simulation of ring expansion and fragmentation. The capturing of length and time scales through cohesive models of fracture. *International Journal of Fracture*, 95:1–18, 1999.

[141] A. Pandolfi and M. Ortiz. Solid modeling aspects of three-dimensional fragmentation. *Engineering with Computers*, 14:287–308, 1998.

[142] P. Pedregal. Laminates and microstructure. *European Journal of Applied Mathematics*, 4:121–149, 1993.

[143] J. Peraire, J. Peiro, L. Formaggia, K. Morgan, and O.C. Zienkiewicz. Finite element euler computations in three dimensions. *International Journal for Numerical Methods in Engineering*, 26:2135–2159, 1988.

[144] J. Peraire, M. Vahdati, K. Morgan, and O. C. Zienkiewicz. Adaptive remeshing for compressible flow computations. *Journal of Computational Physics*, 72:449–466, 1987.

[145] A.J Piekutowski. Fragmentation of a sphere initiated by hypervelocity impact with a thin sheet. *International Journal of Impact Engineering*, 17:627–638, 1995.

[146] S. Pietruszczak and Z. Mroz. Finite element analysis of deformation of strain softening matrials. *International Journal for Numerical Methods in Engineering*, 17:327–334, 1981.

[147] G. Pijaudier-Cabot and Z. P. Bazant. Nonlocal damage theory. *Journal of Engineering Mechanics/ASCE*, 113:1512–1533, 1987.

[148] G. Pijaudier-Cabot, Z. P. Bazant, and M. Tabbara. Comparison of various models of strain softening. *Engineering Computations*, 5:141–150, 1988.

[149] J. Planas, M. Elices, and G. V. Guinea. Cohesive cracks as a solution of a class of nonlocal problems. In Z. P. Bazant, editor, *Fracture and Damage in Quasibrittle Structures. Experiment, modelling and Computer analysis*. E & FN SPON, 1994.

[150] J. Planas, M. Elices, and G. Ruiz. The equivalent elastic crack. 2. X-Y equivalences and asymptotic analysis. *International Journal of Fracture*, 61:231–246, 1993.

[151] R. Radovitzky and M. Ortiz. Error estimation and adaptive meshing in strongly nonlinear dynamic problems. *Computer Methods in Applied Mechanics and Engineering*, 172:203–240, 1999.

[152] R. Radovitzky and M. Ortiz. Tetrahedral mesh generation based on node insertion in crystal lattice arrangements and advancing-front-Delaunay triangulation. *Computer Methods in Applied Mechanics and Engineering*, 187:543–569, 2000.

[153] K. Ravi-Chandar and W. G. Knauss. An experimental investigation into dynamic fracture, Part 1. Crack initiation and arrest. *International Journal of Fracture*, 25(4):247–262, 1984.

[154] K. Ravi-Chandar and W. G. Knauss. An experimental investigation into dynamic fracture. Part 3. On steady state crack propagation and crack branching. *International Journal of Fracture*, 26:141–154, 1984.

[155] H. W. Reinhardt and J. Weerheijm. Tensile fracture of concrete at high loading rates taking account of inertia and crack velocity effects. *International Journal of Fracture*, 51:31–42.

[156] A. A. G. Requicha. Representations for rigid solids: Theory, methods and systems. *Computing Surveys*, 12:437–465, 1980.

[157] J. R. Rice. Mathematical analysis in the mechanics of fracture. In H. Liebowitz, editor, *Fracture*, pages 191–311. Academic Press, 1968.

[158] J. R. Rice. Dislocation nucleation from a crack tip: An analysis based on the peierls concept. *Journal of the Mechanics and Physics of Solids*, 40:235–271, 1992.

[159] J. R. Rice and G. E. Beltz. The activation-energy for dislocation nucleation at a crack. *Journal of the Mechanics and Physics of Solids*, 42:333–360, 1994.

[160] C. Rocco, G. V. Guinea, J. Planas, and M. Elices. Mechanisms of rupture in splitting tests. *ACI Materials Journal*, 96:52–60, 1999.

[161] C. Rocco, G. V. Guinea, J. Planas, and M. Elices. Size effect and boundary conditions in the Brazilian test: experimental verification. *Materials and Structures*, 32:210–217, 1999.

[162] C. Rocco, G. V. Guinea, J. Planas, and M. Elices. Size effect and boundary conditions in the Brazilian test: theoretical analysis. *Materials and Structures*, 32:437–444, 1999.

[163] R.Y. Rockafellar. *Convex Analysis*. Princeton University Press, Princeton, N.J., 1970.

[164] J. Rodríguez, C. Navarro, and V. Sánchez-Gálvez. Splitting tests: An alternative to determine the dynamic tensile strength of ceramic materials. *Journal de Physique IV*, 4:101–106.

[165] J. Roedel, J. F Kelly, and B. R. Lawn. In situ measurements of bridged crack interfaces in scanning electron microscope. *Journal of the American Ceramic Society*, 73:3313–3318, 1990.

[166] J. H. Rose, J. Ferrante, and J. R Smith. Universal binding energy curves for metals and bimetallic interfaces. *Physical Review Letters*, 47:675–678, 1981.

[167] A. Ross, J. W. Tedesco, and S. T. Kuennen. Effects of strain rate on concrete strength. *ACI Materials Journal*, 92:37–47, 1995.

[168] G. Ruiz, M. Ortiz, and A. Pandolfi. Three dimensional finite-element simulation of the dynamic brazilian tests on concrete cylinders. *International Journal for Numerical Methods in Engineering*, 48:963–994, 2000.

[169] G. Ruiz, A. Pandolfi, and M. Ortiz. Three-dimensional cohesive modeling of dynamic mixed-mode fracture. *International Journal for Numerical Methods in Engineering*, 52:97–120, 2001.

[170] V. E. Saouma and G. Fava. On fractal and size effects. *International Journal of Fracture*, 127:231–249, 2006.

[171] S. J. Schneider (Technical Chairman). *Engineered Materials Handbook. Volume 4: Ceramics and Glasses.* ASM International, 1991.

[172] E. Sharon, A. R. Rosenfield, and W. H. Duckworth. Confirming the continuum theory of dynamic brittle fracture for fast cracks. *Nature*, 397:333–335, 1999.

[173] D. K. Shetty. Mixed-mode fracture criteria for reliability analysis and design with structural ceramics. *Journal of Engineering for Gas Turbines and Power*, 109:282–289, 1987.

[174] D. K. Shetty, A. R. Rosenfield, and W. H. Duckworth. Mixed-mode fracture of ceramics in diametral compression. *Journal of the American Ceramic Society*, 69:437–443, 1986.

[175] D. K. Shetty, A. R. Rosenfield, and W. H. Duckworth. Mixed-mode fracture in biaxial stress state. Application of the diametral-compression (brazilian disk) test. *Engineering Fracture Mechanics*, 26:825–840, 1987.

[176] J. C. Simo and J. Oliver. A new approach to the analysis and simulation of strain softening in solids. In Z. P. et al. Bazant, editor, *Fracture and Damage in Quasibrittle Structures*, pages 25–39. E. & F. N. SPON, London, 1994.

[177] J. C. Simo, J. Oliver, and F. Armero. An analysis of strong discontinuities induced by strain softening in rate-independent inelastic solids. *Computational Mechanics*, 12:277–296, 1993.

[178] D. Singh and D. K. Shetty. Fracture toughness of polycristalline ceramics in combined mode i and mode ii loading. *Journal of the American Ceramic Society*, 72:78–84, 1989.

[179] R. Talreja. Continuum modeling of damage in ceramic matrix composites. *Mechanics of Materials*, 12:165–180, 1991.

[180] J. W. Tedesco, C. A. Ross, and S. T. Kuennen. Experimental and numerical-analysis of high-strain rate splitting tensile tests. *ACI Materials Journal*, 90:162–169, 1993.

[181] J. W. Tedesco, C. A. Ross, P. B. McGill, and B. P. O'Neil. Numerical analysis of high strain rate concrete direct tension tests. *Composites Structures*, 40:313–327, 1991.

[182] P. Thoutireddy and M. Ortiz. A variational r-adaption and shape-optimization method for finite-deformation elasticity. *International Journal for Numerical Methods in Engineering*, 61:1–21, 2004.

[183] V. Tikare and S. R. Choi. Combined mode i and mode ii fracture of monolithic ceramics. *Journal of the American Ceramic Society*, 76:2265–2272, 1993.

[184] D. K. Tran, A. S. Kobayashi, and K. W. White. Process zone of polycrystalline alumina. *Experimental Mechanics*, 39:20–24, 1999.

[185] V. Tvergaard and J. W. Hutchinson. The influence of plasticity on mixed-mode interface toughness. *Journal of the Mechanics and Physics of Solids*, 41:1119–1135, 1993.

[186] V. Tvergaard and J. W. Hutchinson. Effect of strain dependent cohesive zone model on predictions of crack growth resistance. *International Journal of Solids and Structures*, 33:3297–3308, 1996.

[187] V. Tvergaard and J. W. Hutchinson. Effect of strain dependent cohesive zone model on predictions of interface crack growth. *Journal de Physique IV*, 6:165–172, 1996.

[188] J. C. A. M. van Doormaal, J. Weerheijm, and L. J. Sluys. Experimental and numerical determination of the dynamic fracture energy of concrete. *Journal de Physique IV*, C8:501–506, 1994.

[189] B. Vekinis, M. G. Ashby, and P. W. R. Beaumont. R-curve behavior of Al_2O_3 ceramics. *Acta Metallurgica et Materialia*, 38:1151–1162, 1990.

[190] A. Wells. Application of fracture mechanics at and beyond general yielding. *Welding Research Ass.*, Report M13, 1963.

[191] G. N. Wells, R. de Borst, and L. J. Sluys. A consistent geometrically nonlinear approach for delamination. *International Journal for Numerical Methods in Engineering*, 54:1333.

[192] H. M. Westergaard. Bearing pressures and cracks. *Journal of Applied Mechanics*, June 1939:A49–A53, 1939.

[193] K. Willam. Simulation issues of distributed and localized failure computations. In J. Mazars and Z. P. Bazant, editors, *Cracking and Damage*, pages 363–378. Elsevier Science, New York, 1989.

[194] R. L. Woodward, W. A. Gooch, R. G. O'Donnell, W. J. Perciballi, B. J. Baxter, and S. D. Pattie. A study of fragmentation in the ballistic impact of ceramics. *International Journal of Impact Engineering*, 15:605–618, 1994.

[195] F. H. Wu and L. B. Freund. Deformation trapping due to thermoplastic instability in one-dimensional wave-propagation. *Journal of the Mechanics and Physics of Solids*, 32:119–132, 1984.

[196] G. Xu and M. Ortiz. A variational boundary integral method for the analysis of 3–d cracks of arbitrary geometry modeled as continuous distributions of dislocation loops. *International Journal for Numerical Methods in Engineering*, 36:3675–3701, 1993.

[197] X.-P. Xu and A. Needleman. Void nucleation by inclusion debonding in a crystal matrix. *Modelling and Simulation in Materials Science and Engineering*, 1:111–132, 1993.

[198] X.-P. Xu and A. Needleman. Numerical simulations of fast crack growth in brittle solids. *Journal of the Mechanics and Physics of Solids*, 42:1397–, 1994.

[199] X.-P. Xu and A. Needleman. Numerical simulations of dynamic interfacial crack growth allowing for crack growth away from the bond line. *International Journal of Fracture*, 74:253–275, 1995.

[200] X.-P. Xu and A. Needleman. Numerical simulations of dynamic crack growth along interface. *International Journal of Fracture*, 74:289–324, 1996.

[201] J. H. Yon, N. M Hawkins, and A. S. Kobayashi. Fracture process zone in dynamically loaded crack-line wedge-loaded, double-cantilever beam concrete specimens. *ACI Materials Journal*, 88:470–479.

[202] J. H. Yon, N. M Hawkins, and A. S. Kobayashi. Numerical simulation of mode i dynamic fracture concrete. *Journal of Engineering Mechanics/ASCE*, 117:1595–1610, 1991.

[203] J. H. Yon, N. M Hawkins, and A. S. Kobayashi. Strain-Rate Sensitivity of Concrete Mechanical Properties. *ACI Materials Journal*, 89:146–153, 1992.

[204] C.-T. Yu, A. S. Kobayashi, and N. M Hawkins. Energy-dissipation mechanisms associated with rapid fracture of concrete. *Experimental Mechanics*, 33:205–211, 1993.

[205] R. C. Yu, A. Pandolfi, D. Coker, M. Ortiz, and R. J. Rosakis. Three-dimensional modeling of intersonic crack-growth in asymmetrically loaded unidirectional composite plate. *International Journal of Solids and Structures*, 39:6135–6157, 2002.

[206] R. C. Yu, A. Pandolfi, and M. Ortiz. A 3d numerical investigation on branching for brittle materials. 2007. in press.

[207] R. C. Yu, G. Ruiz, and A. Pandolfi. Numerical investigation of the dynamic behavior of advanced ceramics. *Engineering Fracture Mechanics*, 71:897–911, 2004.

[208] A. T. Zehnder and A. J. Rosakis. Dynamic fracture initiation and propagation in 4340 steel under impact loading. *International Journal of Fracture*, 43:271–285, 1990.